AD-A096 815 BATTELLE COLUMBUS LABS OH F/G 20/6
OPTICAL WAVEGUIDE SCATTERING REDUCTION. II.(U)
DEC 80 D W VAHEY, N F HARTMAN, R C SHERMAN F33615-79-C-1852
AFWAL-TR-80-1186 NL

UNCLASSIFIED

1 2

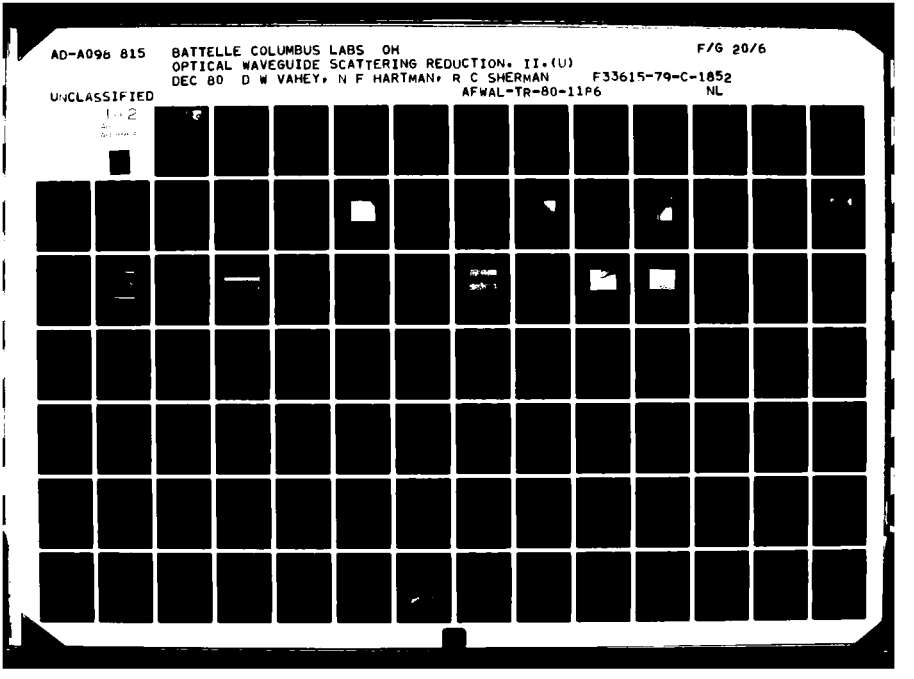

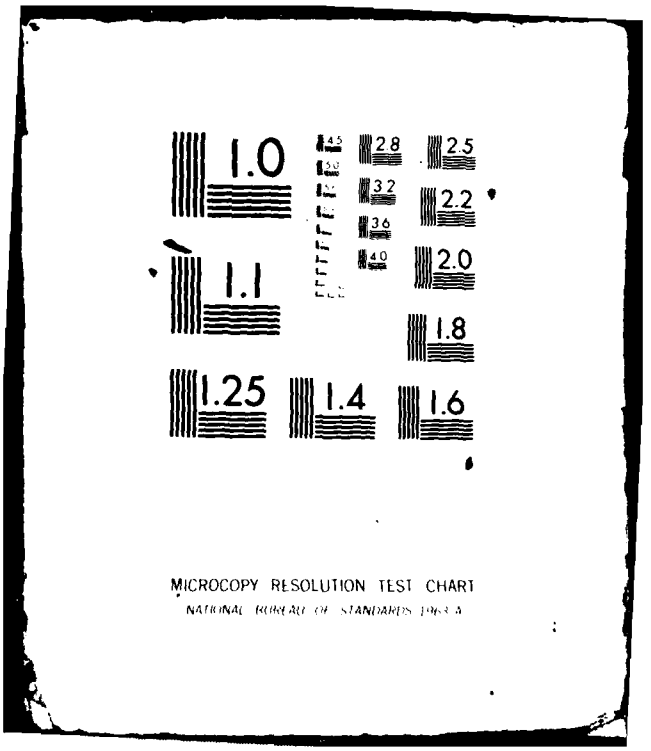
1.0
1.1
1.25
1.4
1.6
1.8
2.0
2.2
2.5
2.8
3.2
3.6
4.0
MICROCOPY RESOLUTION TEST CHART
NATIONAL BUREAU OF STANDARDS 1963-A

LEVEL II

2

AFWAL-TR-80-1186

AD A098815

OPTICAL WAVEGUIDE SCATTERING REDUCTION II

BATTELLE COLUMBUS LABORATORIES
505 KING AVENUE
COLUMBUS, OHIO 43201

December 1980

TECHNICAL REPORT AFWAL-TR-80-1186

Final Report for Period July 1979 to August 1980

Approved for public release; distribution unlimited.

AVIONICS LABORATORY
AIR FORCE WRIGHT AERONAUTICAL LABORATORIES
AIR FORCE SYSTEMS COMMAND
WRIGHT-PATTERSON AIR FORCE BASE, OHIO 45433

NOTICE

When Government drawings, specifications, or other data are used for any purpose other than in connection with a definitely related Government procurement operation, the United States Government thereby incurs no responsibility nor any obligation whatsoever; and the fact that the government may have formulated, furnished, or in any way supplied the said drawings, specifications, or other data, is not to be regarded by implication or otherwise as in any manner licensing the holder or any other person or corporation, or conveying any rights or permission to manufacture use, or sell any patented invention that may in any way be related thereto.

This report has been reviewed by the Office of Public Affairs (ASD/PA) and is releasable to the National Technical Information Service (NTIS). At NTIS, it will be available to the general public, including foreign nations.

This technical report has been reviewed and is approved for publication.

Douglas A. Wille

DOUGLAS A. WILLE, Project Engineer
Electro-Optics Techniques and
Applications Group

Kenneth R. Hutchinson

KENNETH R. HUTCHINSON, Chief
Electro-Optics Techniques and
Applications Group

FOR THE COMMANDER

Richard L. Remski

RICHARD L. REMSKI, Acting Chief
Electro-Optics Technology Branch
Avionics Laboratory

"If your address has changed, if you wish to be removed from our mailing list, or if the addressee is no longer employed by your organization please notify AFWAL/AADO-2, W-PAFB, OH 45433 to help us maintain a current mailing list".

Copies of this report should not be returned unless return is required by security considerations, contractual obligations, or notice on a specific document.

AIR FORCE/56780/30 April 1981 — 40

(12) 157

SECURITY CLASSIFICATION OF THIS PAGE (When Data Entered)

(19) **REPORT DOCUMENTATION PAGE**

READ INSTRUCTIONS BEFORE COMPLETING FORM

(18) 1. REPORT NUMBER: AFWAL-TR-80-1186	2. GOVT ACCESSION NO.: AD-A098815
3. RECIPIENT'S CATALOG NUMBER	
(6) 4. TITLE (and Subtitle): OPTICAL WAVEGUIDE SCATTERING REDUCTION, II.	5. TYPE OF REPORT & PERIOD COVERED: July 2, 1979 - Final - August 2, 1980
	6. PERFORMING ORG. REPORT NUMBER
(10) 7. AUTHOR(s): David W. Vahey, Nile F. Hartman and Rand C. Sherman	(15) 8. CONTRACT OR GRANT NUMBER(s): F33615-79-C-1852
9. PERFORMING ORGANIZATION NAME AND ADDRESS: Battelle Columbus Laboratories, 505 King Avenue, Columbus, Ohio 43201	(16) 10. PROGRAM ELEMENT, PROJECT, TASK AREA & WORK UNIT NUMBERS: 62204F, 2001 0268 (17) 02
(11) 11. CONTROLLING OFFICE NAME AND ADDRESS: Avionics Laboratory (AFWAL/AADO), Air Force Wright Aeronautical Laboratories, Wright-Patterson AFB, OH 45433	12. REPORT DATE: December 1980
	13. NUMBER OF PAGES: 157
14. MONITORING AGENCY NAME & ADDRESS (if different from Controlling Office): (9 Final rept. 2 Jul 79-2 Aug 80)	15. SECURITY CLASS. (of this report): Unclassified
	15a. DECLASSIFICATION/DOWNGRADING SCHEDULE

16. DISTRIBUTION STATEMENT (of this Report)

Approved for public release: distribution unlimited

17. DISTRIBUTION STATEMENT (of the abstract entered in Block 20, if different from Report)

18. SUPPLEMENTARY NOTES

19. KEY WORDS (Continue on reverse side if necessary and identify by block number)

Integrated Optics, Optical Waveguides, Scattering, Surface Roughness, Spectrum Analyzer, $LiNbO_3$, Ti-Diffused $LiNbO_3$, Out-Diffused $LiNbO_3$, Li_2TiO_3, $Li_2Ti_3O_7$, $LiNb_3O_8$, Prism Coupling, Edge Polishing, End-Fire Coupling, Dynamic Range, Diffusion Conditions, Prism Scattering, Reflection Scattering, e-Beam-X-Ray Analysis, Talystep Profilometry

20. ABSTRACT (Continue on reverse side if necessary and identify by block number)

The goal of this program was the reduction of scattering in optical waveguides to levels commensurate with 40 dB dynamic range for an integrated optical spectrum analyzer. Waveguides formed by thermal diffusion of Ti films into $LiNbO_3$ substrates were emphasized. Nine potential sources of scattering in such waveguides were identified and discussed. Diagnostic methods and optical scattering experiments useful for studying the sources of scattering were described and experimental results for non-scattering experiments were presented. An analysis of the effects of Rayleigh, Rayleigh-Gans-Debye, and Mie scattering on spectrum →

DD FORM 1 JAN 73 1473

SECURITY CLASSIFICATION OF THIS PAGE (When Data Entered)

407080

analyzer dynamic range was performed. Formulas for differential scattering cross sections were derived, and parameter values for various sources of scattering were inserted to obtain estimates of spectrum-analyzer performance for each scattering mechanism. Rayleigh-Gans-Debye scattering centers from surface roughness and surface compounds (probably Li-Ti-O compounds) were found to lead to the largest predicted scattering.

Experimental in-plane scattered-energy distributions were complicated by the effects of prism-enhanced scattering, which was theoretically investigated. Data were obtained using either end-fire input coupling or by comparing the scattering generated using two different input-output coupling-prism separations. The best performance achieved was consistent with scattering from either surface roughness or surface-compound formation. The performance was consistent with a spectrum-analyzer dynamic range of only 27 dB. However, the same scattering centers, when housed in a waveguide having surface index change $\Delta n = 0.0049$ and diffusion depth $D = 3.29\ \mu m$, were projected to result in a spectrum analyzer having at least the requisite dynamic range of 40 dB. These parameters are expected to result from the diffusion of a 150 Å thick Ti film for 8 hr at 1000°C. No significant influence on scattering is believed to be associated with substrate cleaning variations, microdomains, or formation of the phase $LiNb_3O_8$ as long as the diffused sample is not slowly cooled. Surface roughness is less than 3 Å in the as received substrate but is found to be in the vicinity of 30 Å after Ti diffusion. This roughness is still too small to limit dynamic range except in waveguides having large values of $\Delta n/D$, say $0.01\ \mu m^{-1}$. By elimination, the chief scattering mechanism is the formation of Li-Ti-O compounds at or near the waveguide surface. These are successfully controlled by post-diffusion polishing of the waveguide surface as well as by the use of longer, hotter diffusion treatments.

TABLE OF CONTENTS

TABLE OF CONTENTS
(Continued)

TABLE OF CONTENTS
(Continued)

LIST OF ILLUSTRATIONS

LIST OF ILLUSTRATIONS
(Continued)

FIGURE

I. INTRODUCTION

This report summarizes the results of a two-year investigation of optical waveguide scattering phenomena. It builds on, and in some cases corrects, information obtained during the first-year investigation, described in Ref. 1. The program was funded by the Air Force in connection with their on-going effort to develop an integrated optical spectrum analyzer.[2] Air Force personnel have long recognized that the signal processing capabilities of an integrated optical spectrum analyzer, as measured by its dynamic range, was likely to be limited by scattering events in the waveguide carrier. The objective of the present program has been to study these events, obtain information regarding the sources of scattering, and develop fabrication procedures that minimize the number or effectiveness of these sources.

Owing to the difficulty of the problem, only one of several candidate waveguides has been considered. That has been the Ti-diffused $LiNbO_3$ waveguide, currently the waveguide of choice for the spectrum analyzer application. At the conclusion of the research, we are able to state with confidence that this class of waveguide is indeed useful for spectrum analyzers having a dynamic range of 40 dB, as required by currently envisioned device applications.

Unfortunately, this conclusion cannot be based on the actual fabrication and testing of a waveguide commensurate with this level of performance. Spurious scattering associated with prism input coupling has constituted a source of noise that has prevented this. We have developed methods for dealing with this noise and have derived an encompassing if not rigorous theory to use in interpreting our results. This theory allows us to reach conclusions regarding the number and effectiveness of scattering centers in our waveguides. From this we can predict the performance of waveguides fabricated using altered diffusion conditions. Our opinion that $LiNbO_3$ is an eminently suitable substrate for an integrated optical spectrum analyzer is based on the highly favorable outcome of these predictions.

Progress toward this conclusion has resulted from achievements fully described in the body and appendices of this report. Section II contains a listing and discussion of the physical basis for nine potential sources of scattering relevant to $LiNbO_3$ waveguides. They range from those associated

with substrate preparation, such as polishing, to those associated with diffusion phenomena, such as lithium-titanate compound formation at the diffused waveguide surface.

Section III is a compendium of experimental methods that may be used to study the scattering centers itemized in Sec. II. These include diagnostic methods which ideally produce direct evidence of individual scattering centers, as well as optical waveguide experiments from which a picture of the scattering centers is pieced together using indirect evidence. We have included in the discussion our experimental results for those methods which were only used in the program briefly. This included virtually all diagnostic tools, which were frankly not very useful in providing information about the elusive scattering centers in Ti diffused $LiNbO_3$.

In Sec. IV, we present the theoretical analysis necessary for the interpretation of our optical waveguide experiments. The section begins with the derivation of a formula for calculating spectrum-analyzer dynamic range in terms of scattering cross section, scattering-center density, and type of scattering involved (Rayleigh, Rayleigh-Gans-Debye, or Mie). Then we move to the derivation of formulae for scattering cross sections. By inserting in these formulas the values of the scattering parameters estimated for the various mechanisms of Sec. II, we are able to predict the spectrum-analyzer dynamic range associated with each mechanism. The results of this section show that in-plane scattering caused by surface compounds formed during diffusion is likely to be an important limiter of spectrum-analyzer dynamic range.

Section V constitutes the principal experimental section of the report, in which results consistent with scattering from both surface roughness and surface compounds are obtained. The section outlines the experimental methods that were used to obtain in-plane scattered-energy distributions, and the analytical methods that were used to interpret them. Included is a discussion of scattering associated with prism input coupling and of experimental attempts to polish two opposite waveguide edges for end-fire input and output coupling. Then we present experimental results for seven different waveguide samples used in the program, fabricated by various diffusion treatments. The results are used to predict very good performance levels for waveguides having smaller values of surface index change Δn and larger values of diffusion depth D than those we

fabricated. These conditions may be achieved using longer, hotter diffusion treatments (say 8 h at 1000°C), and the use of such conditions is the principal recommendation of this report.

Section VI summarizes the results and conclusions of the program, while Appendices A-E expand on various items mentioned in the body of the report. The most important of these is a theoretical analysis of scattering enhancement associated with the use of prism input coupling. This enhancement is produced by the interaction of the evanescent field of incoming light reflected at the base of the prism with scattering centers at the surface of the waveguide. An unfortunate finding is that the enhancement factor increases for waveguides having index and depth parameters conducive to better scattering performance. The result is that good and bad waveguides tend to produce similar in-plane scattered energy distributions when obtained using prism input coupling. This feature obscures the dependence of waveguide quality on the diffusion treatment and caused us to report erroneously in Ref. 1 that this dependence was minimal.

We now believe that the best Ti-diffused $LiNbO_3$ waveguides will be formed from thinner Ti films (say 150 Å) using longer diffusion treatments (say 8 h) at higher temperatures (say 1000°C). Some post diffusion polishing may be helpful, especially if inhomogeneous mixtures of lithium-titanate compounds remain at the waveguide surface following the heat treatment. This is more likely for thicker Ti films, and may also be influenced by the diffusion atmosphere, oxygen or argon, though this has not been studied.

Post-diffusion polishing may also be helpful in reducing surface roughness caused by the Ti diffusion, though generally surface roughness levels are too low to produce significant scattering except in waveguides having relatively large values of the ratio $\Delta n/D$ (say $\geq 0.01\ \mu m^{-1}$). If such waveguides are required because of system considerations, we point out that good quality waveguides can result from heavily diffused samples by substantial post-diffusion polishing.[1]

II. SOURCES OF SCATTERING IN Ti DIFFUSED $LiNbO_3$ WAVEGUIDES

In this section we discuss potential sources of scattering in Ti:$LiNbO_3$ waveguides that we have been able to identify. Not all of them have been studied in detail, and not all of them are viewed to be significant. But it is appropriate to generate a list to quantify the scope of the scattering problem and to use as a reference when discussing the work of the program.

The sources of scattering are divided into two groups: fabrication-related sources and diffusion-related sources. The former are associated with the human role in preparing waveguides; the latter are related to the physics of the diffusion process, and would be expected to be the more difficult sources to eliminate.

FABRICATION-RELATED SOURCES OF SCATTERING

Surface Roughness

Surface roughness has been the potential source of waveguide scattering most often treated in the literature.[3,4,5] In the context of this report, it refers to the deviation of the waveguide surface from an ideal plane. The simplest model of a rough surface is indicated in Fig. 1. The average deviation of the surface height from the ideal plane is zero, while the rms average deviation is termed σ. The parameter a is the lateral distance over which the surface height function is correlated. It is, in simpler terms, the average wavelength of the surface-roughness undulations. One may think of the waveguide thickness as being modulated by the roughness fluctuations. This causes proportional fluctuations in the waveguide mode index. These fluctuations distort the wavefronts of guided light and cause scattering.

A perhaps more realistic view of a polished surface is shown schematically in Fig. 2., where the effects of subsurface polishing damage are indicated. Additional features not shown in Fig. 1 are voids and cracks caused by imperfect polishing, in which successively smaller abrasives are not used long enough to remove the damage caused by the previous abrasives. Subsurface damage phenomena are known to exist for polished glass and probably exist for $LiNbO_3$, though the

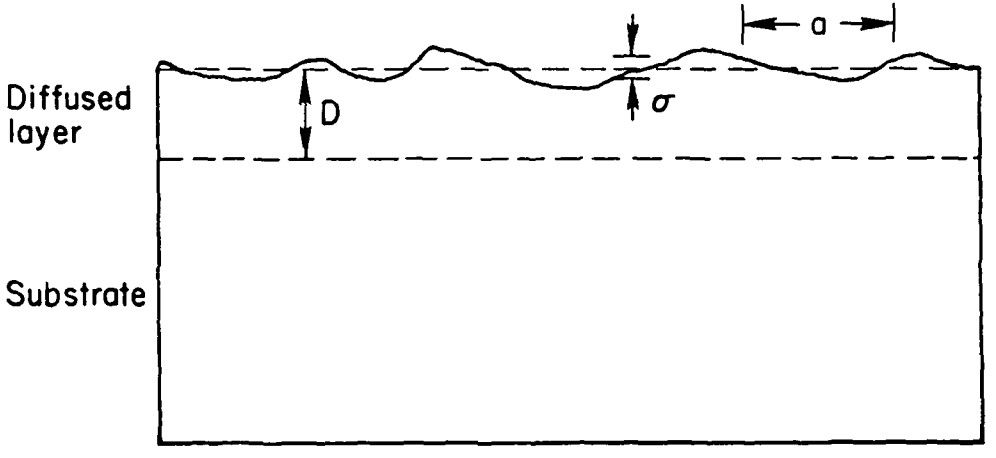

Fig. 1. Schematic drawing of a rough surface.

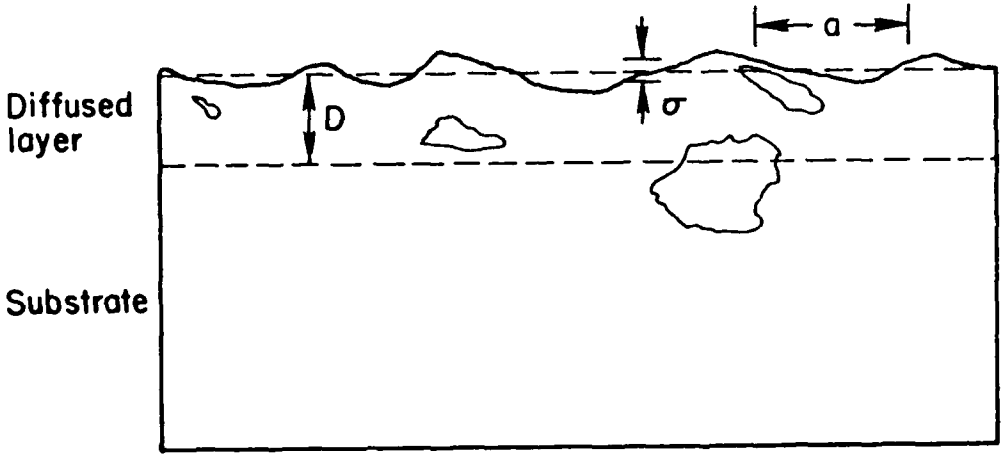

Fig. 2. Schematic drawing of a rough surface showing subsurface polishing damage.

phenomena may be very different because of the crystalline nature and different mechanical properties of $LiNbO_3$ relative to those of glass. We emphasize that Fig. 2 is schematic in nature. We know of no work that has been performed to study the nature of polishing damage in $LiNbO_3$.

Crystalline Imperfections

Nassau, Levinstein, and Loiacono[6] have stated that solid-phase inclusions, gaseous inclusions, prominent low-angle grain boundaries, twin planes, and dislocations have been revealed in pulled $LiNbO_3$. They add that all except dislocations can be eliminated by careful crystal growth. They present photographs showing 10-μm sized triangular and hexagonal inclusions which they describe as metal particles from the crucible.

We have not done a careful study of these phenomena, but our observations tend to be supportive. Samples used in the program have been selected-acoustic-grade material from Crystal Technology, optically polished to λ/10 on both sides to facilitate inspection. The most often observed imperfections are macroscopic refractive-index striations that run for centimeter lengths parallel to the optic axis. The manufacturer has been cooperative in providing us with crystals that do not exhibit this phenomenon, which may reflect imperfect poling or fluctuations in crystal stochiometry.

Titanium Nonuniformity

Fluctuations in the titanium concentration in diffused waveguides will be associated with refractive-index fluctuations that can scatter light. Some potential sources of Ti nonuniformity are diffusion related and are discussed below. One source that is fabrication related has to do with the deposition of a Ti film for diffusion on an imperfectly cleaned $LiNbO_3$ substrate. At the high temperature required for diffusion, dust and surface residues will oxidize and, possibly, mar the uniformity and diffusion characteristics of the overlaying Ti film. These variations in the film later produce variations in the diffused layer which scatter light.

Figure 3 shows a Nomarski Micrograph of the edge of a Ti-diffused $LiNbO_3$ waveguide. The center of the waveguide is defect free. The artifacts presumably result from poor cleanliness at the sample edge. The micrograph reveals circular structures of 5-10 μm diameter that could be areas where the Ti-film exploded away at the high diffusion temperature. Also noted are smaller reflective structures where, for unknown reasons, the Ti was not diffused into the surface.

Fig. 3. Nomarski micrograph showing artifacts near the edge of a Ti-diffused $LiNbO_3$ waveguide. (500X)

DIFFUSION RELATED SOURCES OF SCATTERING

Li-Ti-O Compound Formation

Burns, Klein, West and Plew have published evidence that the diffused Ti concentration in Ti:$LiNbO_3$ waveguides shows a peak extending to about 0.3 μm below the surface.[7] This peak is imposed upon the anticipated Gaussian diffusion profile extending 2 μm below the surface. The authors postulate that the excess Ti concentration is bound in the form of Li-Ti-O compounds such as Li_2TiO_3 or $Li_2Ti_3O_7$. These compounds form a dilute mixture with the $LiNbO_3$ host. Unless this mixture is homogeneously distributed in the plane of the waveguide, it will constitute a source of waveguide scattering.

Microdomains

Microdomains in grown crystals are generally prevented by the use of proper poling techniques.[8] However, Ohnishi has reported that domain reversal at the positive dipole (+c) face of $LiNbO_3$ can occur at the elevated temperatures used to make waveguides by diffusion.[9] Also, Venables reports that microdomains can be generated in $LiTaO_3$ crystals by the process of grinding and polishing thin wafers.[10] Both of these mechanisms could conceivably introduce microdomain scattering centers into $LiNbO_3$ waveguides.

Growth Strains and Misfit Dislocations

Ramaswamy and Standley have reported the observation of dislocations in Nb-diffused $LiTaO_3$ caused by elastic strain due to the lattice mismatch between $LiNbO_3$ and $LiTaO_3$.[11] Boyd, Schmidt, and Storz report that Ni diffusion into a $LiNbO_3$ rod produced strains sufficient to fracture the crystal.[12] Sugii, Fukama, and Iwasaki found a 0.1% lattice contractions caused by Ti diffusion into $LiNbO_3$.[13] This resulted in misfit dislocations and cracks in the diffused layer that could serve as a source of waveguide scattered light.

$LiNb_3O_8$ Formation

Svaasand, Eriksrud, Nakken, and Grande have observed the gradual conversion of $LiNbO_3$ to $LiNb_3O_8$ upon heating the crystal to the vicinity of 810°C.[14] The latter phase occurs in the form of small crystallites that were demonstrably effective scatterers of light. Some generation of $LiNb_3O_8$ crystallites could occur during waveguide fabrication as the substrate is heated to or cooled from the diffusion temperature, giving rise to optical waveguide scattering. In this connection, note that the outdiffusion process is described by the chemical reaction $3LiNbO_3 \rightarrow Li_2O + LiNb_3O_8$. Outdiffusion during waveguide formation may thus be conducive to scattering by separated phase material, provided this material is not homogeneously distributed in the plane of the waveguide. Figure 4 shows the surface degradation that can result from a heat treatment specifically intended to produce the separated phase $LiNb_3O_8$.

Globular Metal Films

It is known that vacuum evaporation of thin layers of Sn onto heated substrates can produce globular films containing particles of the order of the wavelength of visible light in size.[15] If this phenomena were to occur for the case of Ti films evaporated on $LiNbO_3$ substrates, the resultant diffused layer could contain index inhomogeneities capable of scattering light.

Statistical Fluctuations

Even if perfection is achieved in the fabrication of a uniform Ti film and in the subsequent diffusion process, a finite level of scattering will still result from statistical fluctuations in the concentration of Ti throughout the waveguide. This is the lowest level of scattering which is theoretically possible.

Fig. 4. Nomarski micrograph showing the results of a 10 min heat treatment of $LiNbO_3$ at 850°C in flowing O_2. (500X)

III. METHODS FOR STUDY OF SCATTERING SOURCES

In this section we will present a compendium of methods that may be used to study sources of waveguide scattering. We have employed many of these methods to varying degrees, and we will indicate when appropriate our experiences with them. Our results with the methods that we employed most often will, however, be covered in later sections in more detail.

We classify methods for studying scattering sources as being either direct or indirect, depending on whether the method provides actual information about the source or information that must be inferred from a related observation. Microscopy in its varied forms would be an example of a direct method, while etching studies would be an example of an indirect method. Direct methods can be further divided into topographical approaches, which look for surface structures, and compositional approaches, that look for spatial variation in chemical make up.

DIRECT METHODS

Topographical Approaches

Nomarski Microscopy

The microscope is the most obvious tool for examining surface topography, but in the case of highly polished surfaces showing little structure it leaves much to be desired as a means for resolving small surface height differential. An adaptation known as differential-interference-contrast microscopy (or Nomarski microscopy) has the capability for converting phase information imposed on an optical beam by reflection from a nearly perfect surface to amplitude information.[16] This makes it possible to view topographical structures as small as several Angstroms provided the slopes are sufficiently steep.

Our main use of the Nomarski microscope throughout this program has been to evaluate the topography of diffused waveguide surfaces directly after diffusion. We usually have found a granular texture such as that shown in Fig. 5 which we speculated was one result of the Li-Ti-O compound formation

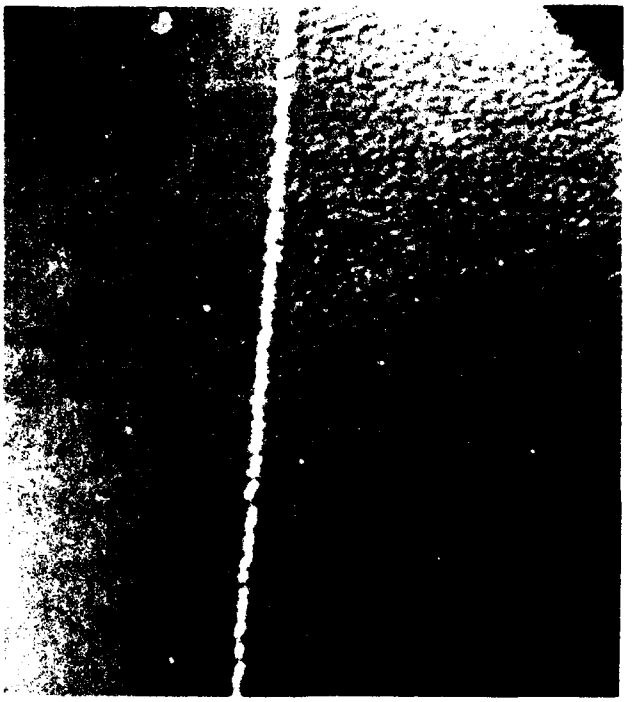

Fig. 5. Nomarski micrograph showing the granular surface texture associated with Ti diffusion (1000 Å Ti film, 26 h diffusion, 500X magnification). Vertical line shows the demarkation between the diffused region (right) and the undiffused region (left).

described by Burns and coworkers.[7] Other have noted a change in this granularity with increasing diffusion time, with the appearance of the surface generally becoming smoother.[17] We have tentative evidence that this is the case but have not performed a careful study. Our approach has been to achieve waveguide quality enhancement by polishing away the granular layer. Our experiments are summarized in Ref. 1.

TIR Microscopy

A different optical microscopic technique has been employed by H. E. Bennett and coworkers at the Naval Weapons Center.[18] As shown in Fig. 6, a laser beam is reflected from a polished surface at an angle greater than the critical angle. The evanescent field is scattered by surface structures and detected with a conventional optical microscope. This is similar to dark field microscopy. We tested the method and found that it was very sensitive to surface dust, but we were not sufficiently encouraged by our observations to use the technique in place of Nomarski microscopy.

Multiple-Beam-Interference Microscopy

We also tested, briefly, the use of multiple-beam-interference methods for studying surface topography. These methods generally employ a conventional microscope to image the wavefront formed by multiple reflections between a test surface and a reference surface. The two surfaces are coated with a highly reflective layer to increase the number of reflections of light waves trapped between them. This amplifies the phase distortion associated with surface topography to the extent that 5 Å roughness can be observed with 2 μm horizontal resolution.[19] However, the time available during this program to establish this measuring capability was not sufficient to achieve the reported sensitivity. Using a commercial device for measuring the thickness of thin films, called an Angstrometer, we achieved a 100 Å vertical resolution during preliminary investigations (see Fig. 7). This was not adequate to resolve the surface roughness of our $LiNbO_3$ samples, and we did not pursue the method further.

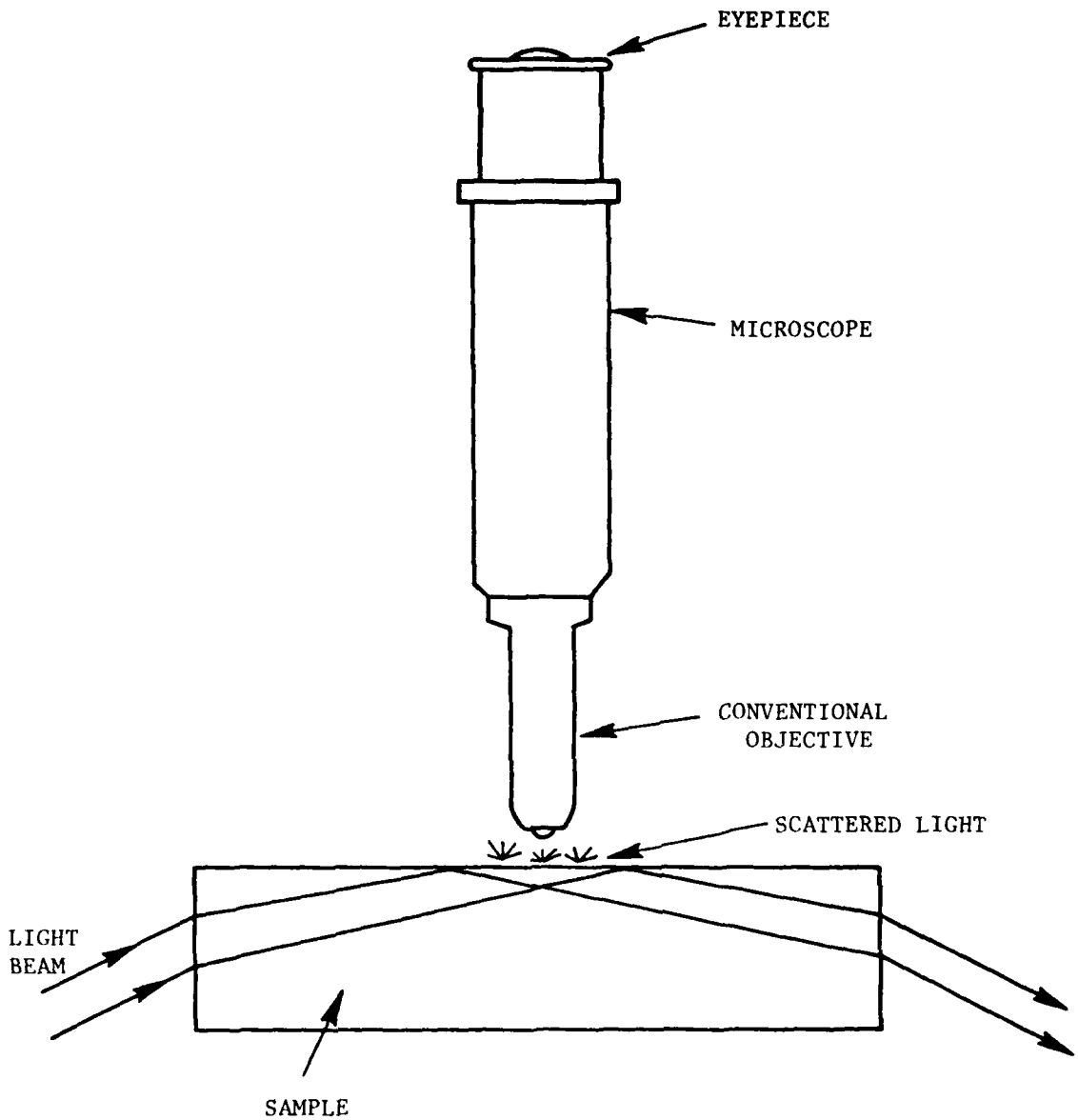

Fig. 6. Total-internal-reflection microscopy.

Fig. 7. Angstrometer data showing 100 Å vertical resolution.

Scanning Electron Microscopy

The final microscopic technique that we tested was that of the scanning electron microscope (SEM). Actually we employed this equipment in several modes of operation during the program, but the one we describe here is a shadowing method for looking at the topography of relatively smooth surfaces. In this technique a sample of $LiNbO_3$ is coated with gold at glancing incidence ($\sim 1^\circ$) to allow shallow topographical structures to shadow the surface. Fig. 8 shows the resultant SEM micrograph of a dusty surface, in which the shadowing effect is clearly evident. However the technique becomes less useful as the slope of the surface irregularities becomes small in comparison to the angle of incidence of the evaporated beam, and this was apparently the case for clean portions of the sample examined. There was no variation in surface contrast that could obviously be attributed to the topography of the polished surface.

Talystep Profilometry

The last topographical approach that was employed to study surface roughness was the Talystep instrument operated by Drs. Ted Vorburger and Clayton Teague of the National Bureau of Standards. This instrument has a maximum magnification of 10^6, making possible the detection of rms surface roughness as small as 1 Å. At this level of magnification the instrument was used with a chisel-shaped stylus with approximate dimensions 0.1 μm x 1 μm.

The instrument was used to examine the topography of a polished $LiNbO_3$ substrate purchased from Crystal Technology. No processing of the substrate was performed prior to the examination. Ted Vorburger of NBS made three 1.5-mm long scans of the surface both parallel and perpendicular to the optical axis. He reported that the surface was among the smoothest ever examined at NBS, with less than 3 Å rms roughness and an autocorrelation length of about 36 μm. The autocorrelation length may have been slightly longer when measured parallel to the optical axis. There was possibly an additional short wave correlation length of about 1 μm, but this was too close to the lateral resolution of the system to be sure. For that matter, a significant fraction of the 3 Å roughness could have its origin in system noise. The complete NBS report is Appendix A of this report. Surface evaluation was repeated after an interval of 73 days with similar results.

Fig. 8. SEM shadowgraph of a dusty $LiNbO_3$ surface. (2000X)

The sensitivity of the Talystep instrument makes it, in our opinion, the best tool for surface-roughness studies in this type of work. Unfortunately, awareness of this instrument and its capabilities came too late to make further use of it during the program.

Compositional Approaches

E-Beam X-Ray Analysis

Other methods for direct observation of waveguide scattering centers look for variations in the composition of the waveguide materials rather than for variations in waveguide topography. One such method is e-beam x-ray analysis, in which a micron-sized electron beam is used to bombard a sample with the objective of creating x-rays characteristic of the materials encountered.[20] This technique has been used to measure Ti-concentration profiles in planar and channel waveguides.[20,21] However, in a scattering program the objective is to measure nonuniformities in the Ti concentration, rather than the average concentration, and a much greater sensitivity is required of the technique.

We employed e-beam x-ray analysis to look for Ti nonuniformities in a diffused waveguide, in an undiffused, unoxidized Ti film, and in an undiffused, oxidized Ti film. Both films were on $LiNbO_3$ substrates. The only situation for which we observed a Ti nonuniformity was in the case of the undiffused film that had been oxidized at 600°C for 1 hour. The initial film was deposited on an imperfectly clean surface and served to decorate the surface residues. After thermal oxidation, further decoration occurred, and new imperfections, such as micron sized bubbles, were observed. It might be anticipated that the oxidation process would cause vaporization of organic residues which, in turn would explosively remove some of the overlaying Ti film. We did not acquire any evidence for this, even when we scanned the electron beam through highly decorated regions of the oxidized film. However, we did obtain one scan of the 720 μm length which shows a 5-μm-wide region of excess Ti. This scan is shown in Fig. 9. It is not known if the excess Ti is associated with the oxidation process or with the initial Ti-deposition process. A scan of an unoxidized Ti film revealed no similar feature, although in measurements of this type it must be remembered that a millimeter-sized scan of a micron-sized beam does not cover much surface area.

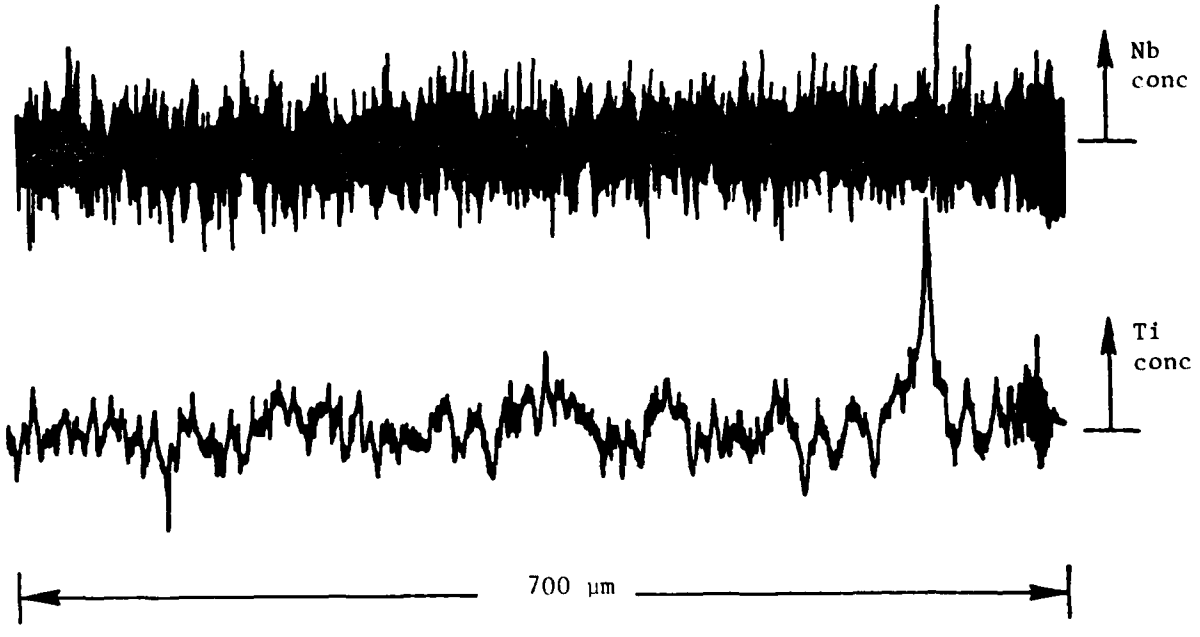

Fig. 9. e-beam, X-ray analysis data showing the presence of a region of excess Ti on an oxidized but undiffused Ti film/$LiNbO_3$ substrate.

The chances of seeing a 5 μm particle using a 1 mm scan are good only if the particle density is large compared to $(0.005 \times 1\ mm^2)^{-1} = 200\ mm^{-2}$. We did not make enough scans of the surface to fully test the potential of this method of measurement. In retrospect this would have been worth doing.

Secondary Ion Mass Spectroscopy

Another technique for looking at compositional variations in waveguide materials is Secondary Ion Mass Spectroscopy (SIMS).[7] In this technique the compositional profile is determined in depth as material is ejected from the surface and analyzed using mass-spectroscopic techniques. This method does not usually offer high spatial resolution in the plane of the waveguide, but it does so in depth. In this sense, SIMS is complimentary to e-beam x-ray analysis which averages over about 2-μm depth but affords good lateral resolution.

The most important use of SIMS in studying optical waveguides was reported by Burns and coworkers.[7] They observed an anomalously large Ti concentration in the top 0.3 μm of a diffused waveguide. They attributed this to the formation of Li-Ti-O compounds during diffusion. We have speculated that the granular structure shown on the waveguide surface of Figure 3 is a further indication of this phenomenon. The importance of this Li-Ti-O surface contamination to waveguide scattering is inferred from the fact that waveguide quality degrades when thicker Ti-films are diffused, but this should ultimately be tested by a series of measurements in which waveguide quality is compared to Li-Ti-O contamination as measured using SIMS.

INDIRECT METHODS

Waveguide Scattering

We now move to a discussion of methods for studying scattering sources in which information must be inferred from observations which are indirectly influenced by scatterers. The method that we have used the most is in-plane waveguide scattering. Measured scattering levels can be related by theory to characteristic scattering parameters. The parameters can then be compared to those which would be expected for various sources. The information obtained by this procedure is model-dependent and should therefore be used to corroborate direct information whenever this is possible. We will have much to say about waveguide scattering measurements and their interpretation in subsequent sections of this report.

Electric-Field Induced Scattering

Occasionally, modifications of the standard in-plane waveguide scattering experiment can be performed to obtain more concrete information about particular scattering sources. For example, we have applied electric fields to $LiNbO_3$ waveguides with the expectation of enhancing scattering from any microdomains that may be present. Our first observations reported in Ref. 1 showed a positive effect. More recently we have determined that the electric-field enhanced scattering that we observed was due to fringing-field effects at the electrodes used to apply the electric field to the waveguide. This conclusion is based on the observation that field-enhanced scattering decreases as the electrode gap becomes significantly wider than the guided beam.

Indiffused and Outdiffused Waveguide Comparison

Another use that can be made of the in-plane waveguide scattering experiment is to compare the scattering from both Ti-indiffused $LiNbO_3$ waveguides and Li_2O-outdiffused $LiNbO_3$ waveguides. Any excess scattering in the former may be ascribed to a source that is related to the Ti diffusant. Similar scattering levels suggests a source of scattering common to the host crystal, such

as surface roughness or the occurrence of the separated phase $LiNb_3O_8$. The situation is complicated by scattering differences associated with prism coupling and by the fact that Ti-diffusion can influence surface roughness and $LiNb_3O_8$ formation. We will discuss this further in connection with our experimental results in Sec. V.

Polishing Studies

Waveguide scattering can be used in "before and after" studies in which the waveguide is repeatedly modified and examined to see if the modification produced a reduction in scattering. Our best example of this is the improvement in waveguide quality that results from polishing the surface.[1] This improvement is most pronounced when thick ($\sim$ 700 Å) Ti films are diffused to make the waveguide. We have attributed the improvement with polishing to removal of Li-Ti-O compounds at the surface as described in Ref. 7.

Reflected Light Scattering

In addition to the use of waveguide scattering to obtain information about sources, we have employed conventional beam scattering from waveguide surfaces to obtain information specifically about surface-roughness parameters. The results will be discussed in detail in Appendix E.

Thermal and Chemical Decoration Techniques

There are, in addition to these optical approaches based on light scattering, several non-optical approaches for obtaining indirect information about scattering sources. These are generally thermal or chemical techniques for decorating flaws that might not otherwise be visible. The most well known of these is wet chemical etching.

We have mentioned several etching studies of $LiNbO_3$ used as a means for observing microdomains.[6,9] Our etching experiments gave no clear indication of the presence of microdomains, but we did observe some interesting effects. The most significant is that Ti diffusion makes the $LiNbO_3$ surface more etch resistant. Figure 10 shows the results of an experiment in which a sample containing a $\sim$ 130 μm wide Ti-diffused channel was etched in hot H_3PO_4. The

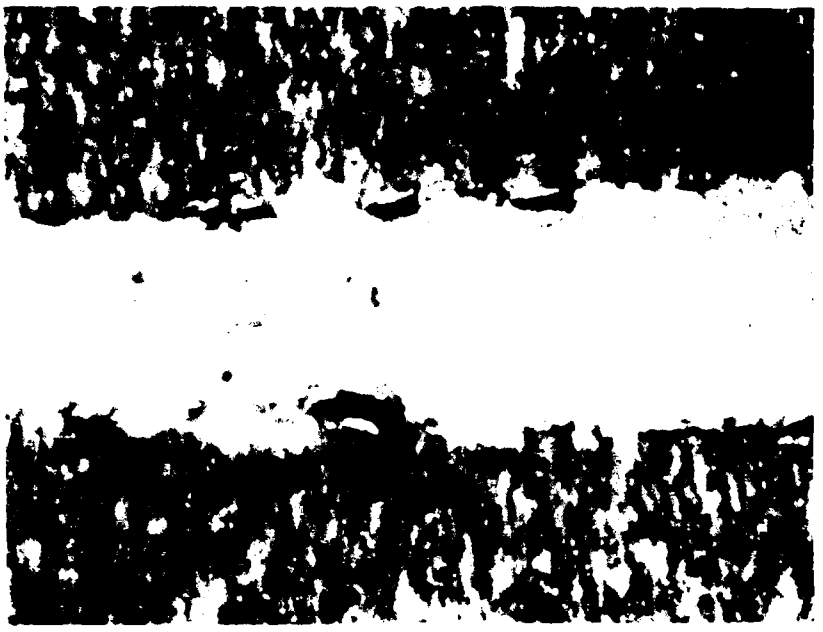

Fig. 10. Results of etching a 130 μm-wide Ti-diffused $LiNbO_3$ channel waveguide in hot H_3PO_4.

material surrounding the channel has been removed to a greater extent than the material in the channel.

Figure 11 shows the results of an etch in hot concentrated H_2SO_4 of a sample that was coated with 150 Å Ti and diffused to form a waveguide. Although the sample was coated uniformly, the resulting waveguide surface showed regions of high and low granularity. When etched, the regions of low granularity showed the characteristic "V" pattern that we believe to be associated with the host material. The regions of high granularity were etch resistant.

This result is supportive of the idea that Li-Ti-O compounds are responsible for etch resistance and that surface granularity is an indication of their presence. Nonuniform distribution of the compounds can cause light scattering. The granular texture of the diffused surface, both before and after etching, suggests that the compounds are indeed distributed nonuniformly in space. The characteristic size of the granular texture is on the order of 1 μm before etching. After etching, the characteristic size estimated from Fig. 11 is more like 20 μm.

Figure 12 shows the results of an etching experiment carried out using 1 part HF and 2 parts HNO_3 at 90°C for 70 min. The sample was a scrap piece of $LiNbO_3$ of uncertain history. It may or may not have been Ti-diffused, although notes on the experiment do not mention any particular etch resistance that may have been associated with the presence of diffused Ti.

The occurrence of etch pits or hillocks similar to the large structures in Fig. 12 have been noted by others, usually in z-cut crystals.[9] Most often they are isolated and occur at the terminus of dislocations. In Fig. 12 the etch-induced structures are contiguous. Moreover, the crystal is y-cut rather than z-cut. This may further effect their interpretation.

One tantalizing way to interpret Fig. 12 is to associate the size and distribution of etch structures with the size and distribution of scattering centers. This is reasonable if the scattering centers give rise to the etch structures. The size of the larger etch structures are 15 μm. Interestingly, this is about the size of the scattering centers as we measure them using in-plane waveguide scattering.

Fig. 11. Results of etching a uniformly Ti-diffused $LiNbO_3$ sample in hot concentrated H_2SO_4.

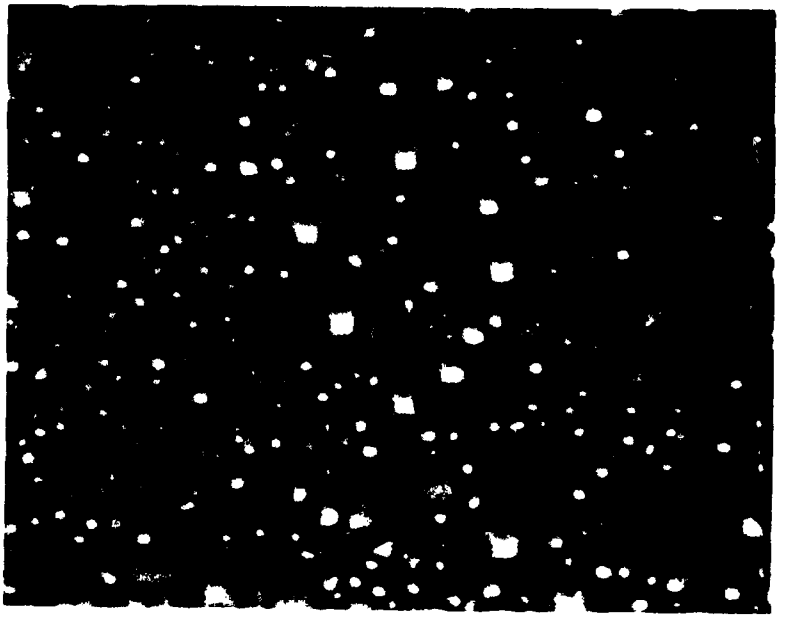

Fig. 12. Results of etching $LiNbO_3$ in hot HF/HNO_3.

IV. EFFECTS OF SCATTERING SOURCES ON WAVEGUIDE AND SPECTRUM ANALYZER PERFORMANCE

In this section we use simple models for sources of scattering to predict their effect on waveguide quality and, in particular, on the dynamic range of a spectrum analyzer.[2] These calculations are helpful in identifying types of scatterers that are likely to be a particular problem in limiting spectrum analyzer performance and they provide us with guidelines to use in interpreting our experimental results of the next sections.

CALCULATION OF SPECTRUM-ANALYZER DYNAMIC RANGE

Figure 13 shows the front and back focal region of a spectrum analyzer design that we will use in calculating dynamic range. The object of the calculation is to predict the scattered signal at any detector relative to the unscattered signal at the central detector. We consider scattering events that occur in both the diffracted and undiffracted beams both before and after the lens. But we do not consider scattering events that occur before the acoustic wave in the front plane of the lens. To further simplify the calculation, we take the lens to be infinitely thin and positioned at the center of the real, distributed lens.

The specifications for the spectrum analyzer shown in Fig. 13 were provided by the Air Force; however, we can base our derivations on a general spectrum analyzer for which F is the lens focal length, W is the unfocused beam width, δy is the detector width, and Δy is the separation of a particular detector from the central detector. The z-axis is the direction of the diffracted beam and z is the distance from the detector array.

To keep the scattering mechanism as general as possible for the present, we describe it by the differential scattering cross section $\sigma(\phi)$, defined as follows: If I is the power per unit width W of the waveguided beam, then

$$\Delta P = I\sigma(\phi)\Delta\phi \qquad (1)$$

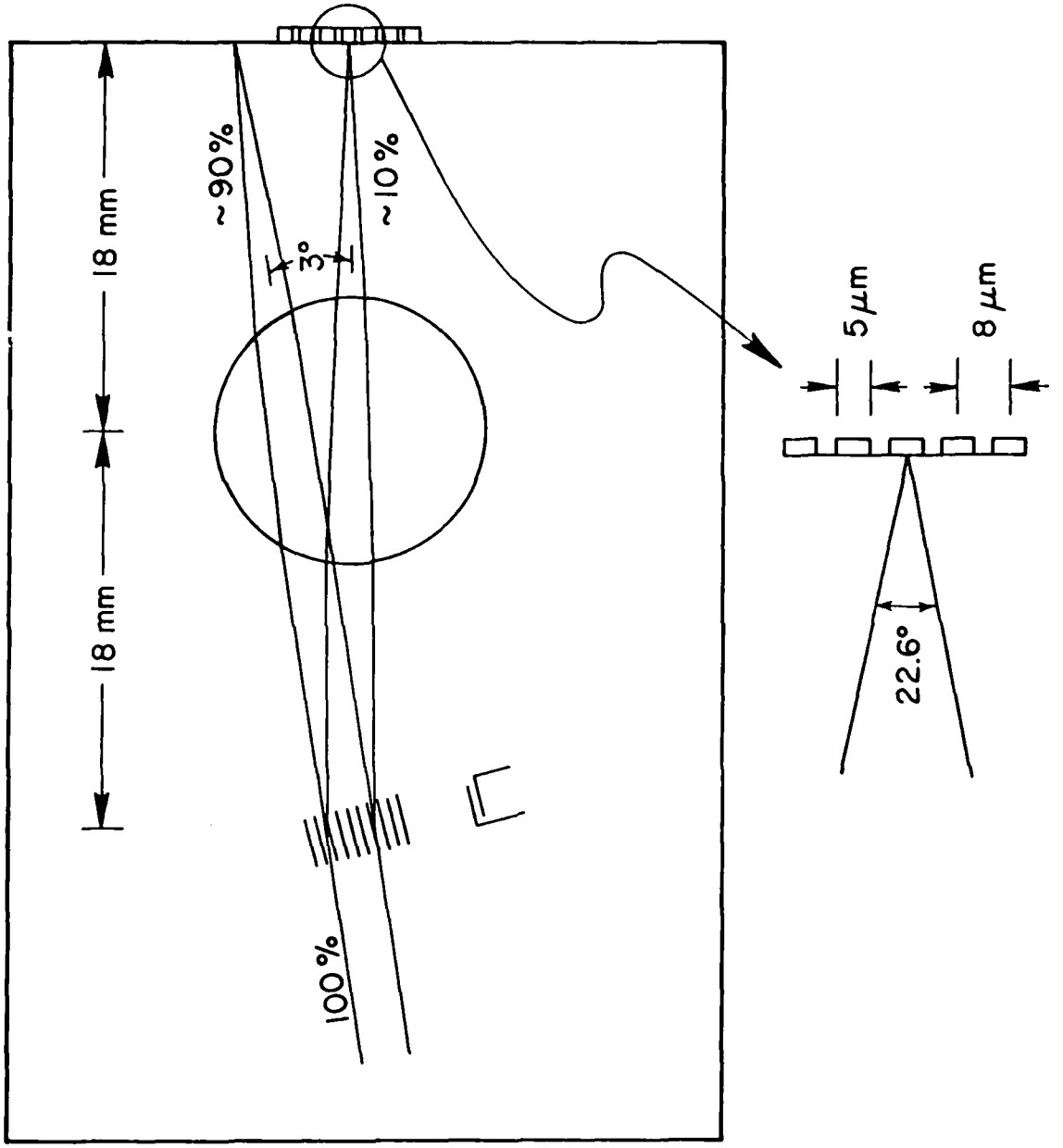

Fig. 13. Geometry used in calculating spectrum analyzer performance.

is the power scattered in plane at an angle ϕ into an angular sector $\Delta\phi$. Note that as a result of the waveguide geometry, $\sigma(\phi)$ has dimensions of length. This is in contrast to the case for scattering in a 3-dimensional geometry, where σ has dimensions of area and I is power per unit area of the incident beam. If there are Σ scattering centers per unit area, then the total power scattered into the sector $\Delta\phi$ is

$$\Delta P_{tot} = \Sigma LW \, I\sigma(\phi)\Delta\phi \quad , \tag{2}$$

where the product LW is the scattering area.

Contribution to Scattered Power from the Focused Beams

To apply these concepts to a calculation of spectrum-analyzer dynamic range, consider the contribution to scattered signal from scattering events that occur between the center of the waveguide lens, assumed thin, and the detector array. Figure 14 defines the scattering parameters for a strip located between z and z + dz, where z is the distance from the array. For rays scattered at height y and incident on the array at height y', the scattering angle is

$$\phi = \tan^{-1}[(y'-y)/z] + \tan^{-1}[y/z] \quad . \tag{3}$$

The total scattered power from the strip into a detector extending from $y' = \Delta y - \delta y/2$ to $y' = \Delta y + \delta y/2$ is obtained by integrating over all scattering angles subtended by the detector, all initial ray heights, and all thin strips. For convenience, we convert the ϕ integration to a y' integration using $d\phi = (\partial\phi/\partial y')dy'$. We have, then

$$\Delta P = \int_0^F dz \int_{-z\tan\theta}^{z\tan\theta} dy \; \Sigma I(y,z) \int_{\Delta y-\delta y/2}^{\Delta y+\delta y/2} dy' \; \sigma[\phi(y,y',z)](\partial\phi/\partial y') \quad . \tag{4}$$

In this expression, θ is the half-angle defined by the converging beam. For most cases of interest, the differential scattering cross section will not vary much with y' across the span of the detector element. Consequently, it may be

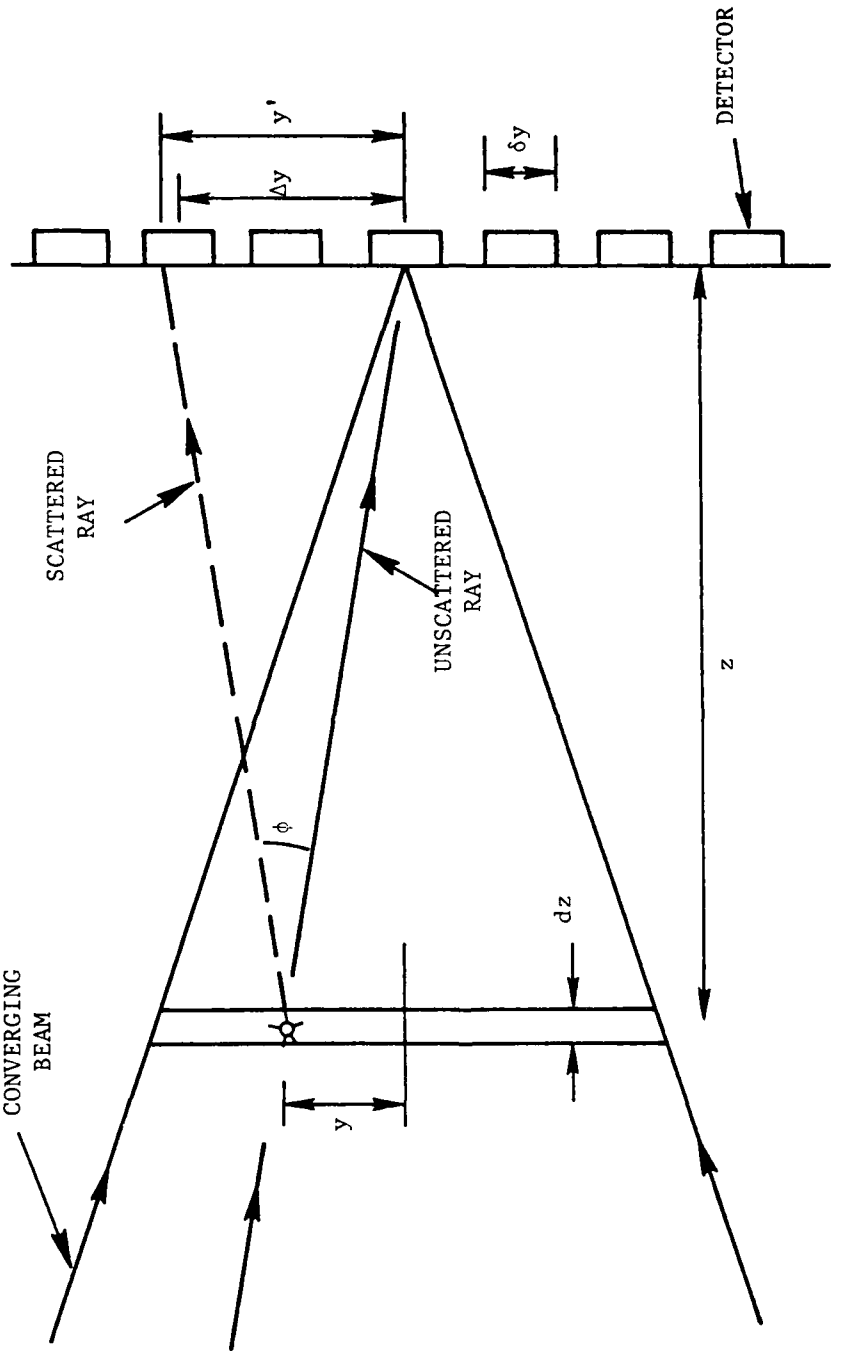

Fig. 14. Parameters for scattering events that occur between the lens and detector array.

replaced by its value at y' = Δy and taken outside the y' integration. The y' integral is then just the difference in the scattering angle φ when evaluated at the edges of the detector. We are left with

$$\Delta P = \int_0^F dz \int_{-z\tan\theta}^{z\tan\theta} dy\, \Sigma I(y,z)\sigma[\phi(y,\Delta y,z)] \qquad (5)$$

$$\times \{\tan^{-1}[(\Delta y + \delta y/2 - y)/z]$$

$$-\tan^{-1}[(\Delta y - \delta y/2 - y)/z]\}.$$

It is desirable to obtain an analytic approximation to this integral, one which at least contains the correct dependences on the parameters, though it may be off by numerical factors on the order of two. Examination of Fig. 14 suggests that the angle subtended by the detector, given by the quantity in curly brackets in Eq. (5), is approximately described by the value obtained when Δy and y are zero. This approximation is best for detectors near the optical axis which are of particular interest since they determine the spectrum analyzer dynamic range.

We also simplify Eq. (5) by using the geometrical optics form for the beam intensity, given by

$$I(y,z) = I_o W/2z\tan\theta \quad \text{in} \quad -z\tan\theta \leq y \leq z\tan\theta, \qquad (6)$$

$$= 0 \text{ elsewhere.}$$

In this expression, $I_o W$ is the total power in the beam, assumed to be approximately uniformly distributed in y at each value of z. Finally, the scattering angle φ, given by Eq. (3) with y' = Δy, varies only slightly with y for a beam with a small value of θ such as we are considering. A good approximate value for φ is therefore the value on axis,

$$\phi(y,\Delta y,z) \approx \tan^{-1}(\Delta y/z) \; . \qquad (7)$$

In the limit of the validity of these approximations the y-integration of Eq. (5) is easily carried out with the result

$$\Delta P = 2 \int_o^F dz\ \Sigma I_o W\ \sigma[\tan^{-1}(\Delta y/z)]\ \tan^{-1}\delta y/2z \quad . \tag{8}$$

We now identify two cases of interest: narrow-angle scattering, associated with scattering centers of characteristic size a large compared with the wavelength (Rayleigh-Gans-Debye (RGD) limit) and wide angle or dipole scattering, associated with scattering centers smaller than the wavelength (Rayleigh limit). In the latter case we may take

$$\sigma(\phi) \simeq \sigma(0) \text{ for TM modes} \quad , \tag{9}$$

$$\sigma(\phi) \simeq \sigma(0)\cos^2\phi \text{ for TE modes} \quad .$$

In the former case, we have shown in Reference 1 that

$$\sigma(\phi) \simeq \sigma(0)\ [1 + k^2a^2\phi^2]^{-1} \quad , \tag{10}$$

where $k = 2\pi/\lambda$, λ being the wavelength in the material.

We can now evaluate the scattered power by inserting these expressions into Eq. (8), using Eq. (7) for ϕ. The simplest case is that of Rayleigh scattering of TM modes. The differential scattering cross section is constant because the in-plane scattering direction is always normal to the mode polarization. The z-dependence of the integrand of Eq. (8) is that of the term $\tan^{-1}\ \delta y/2z$ alone. The value of the integral, taken between the center of the lens and the diode array, is

$$\Delta P = \Sigma I_o W \delta y \sigma(0) \ell n(2F/\delta y) \quad . \tag{11}$$

This is an approximation to the actual integral. It is valid in the limit $2F/\delta y >> 1$, which is well satisfied in all examples of practical interest.

Equation 11 does not show a dependence on Δy owing to our use of $2\tan^{-1}\delta y/2z$ to describe the angle subtended by the detector. For off-axis detectors, a good approximation to the subtended angle is $\delta yz/(z^2 + \Delta y^2)$. When this is used in Eq. (8) in place of $2\tan^{-1}\delta y/2z$, the resulting formula for scattered power is found to be

$$\Delta P = \Sigma I_o W \delta y \sigma(0) \ell n[(F^2 + \Delta y^2)/\Delta y^2]^{1/2} \quad . \tag{12}$$

One can phenomenologically combine Eqs. (11) and (12) to obtain an expression for scattered power that reduces to Eq. (11) when Δy is zero, and yet does not differ significantly from Eq. (12) when Δy is not zero. The combined expression is

$$\Delta P = \Sigma I_o W \delta y \sigma(0) \ell n[(F^2 + \Delta y^2)/(\delta y^2/4 + \Delta y^2)]^{1/2} \quad . \tag{13}$$

This result is valid in the limit of Rayleigh scattering of TM modes.

In considering the Rayleigh limit for TE polarized light, the integrand of Eq. (8) is reduced from the TM case by the factor

$$\cos^2\phi = z^2/(z^2 + \Delta y^2) \quad . \tag{14}$$

This factor results from the obliquity of the polarization of the scattered light relative to the polarization of the incident light. For on-axis scattering, the obliquity factor is unity and the scattered power is the same as that given by Eq. (11) for TM polarization.

For off-axis scattering, the obliquity factor forces the integrand of Eq. (8) to vanish near $z = 0$. For this reason we can take $\tan^{-1}\delta y/2z \approx \delta y/2z$ in Eq. (8) without introducing much error to the integral, even near $z = 0$. The result of integrating over z is exactly the result of Eq. (12) obtained for TM polarization. We conclude that the modified expression of Eq. (13) is valid in the Rayleigh limit for both TE and TM polarization. Differences associated with obliquity can be determined by using the more precise substitution $\tan^{-1}\delta y/2z \rightarrow (z\delta y/2)/(z^2 + \Delta y^2)$ in Eq. (8), but these difference are found to modify Eq. 13 by a small factor of about $[2 \ell n(F/\Delta y)]^{-1}$ which we ignore.

We now consider the case of weak scattering centers large compared with a wavelength (RGD scattering—later we will consider aspects of the more general case of Mie scattering). In the RGD limit, the z-dependent part of the integrand of Eq. (8) is $[1 + k^2a^2(\tan^{-1}\Delta y/z)^2]^{-1} \tan^{-1}\delta y/2z$. Since $ka \gg 1$, the integrand is largest for large z except for the on-axis case $\Delta y = 0$. This suggests that we may replace the inverse-tangent functions by their arguments except when $\Delta y = 0$. In the $\Delta y = 0$ case, small values of z make important

contributions to the integral which are not correctly accounted for by the small-angle approximation. If we ignore this problem temporarily, the approximate integrand has the z dependence $z/(z^2 + k^2a^2\Delta y^2)$. The resulting expression for scattered power is

$$\Delta P \simeq \Sigma I_o W \delta y \, \sigma(0) \ell n[(F^2 + k^2a^2\Delta y^2)^{1/2}/ka\Delta y] \quad . \tag{15}$$

This expression is infinite at $\Delta y = 0$. However, we can replace the logarithmic denominator $ka\Delta y$ by the term $(k^2a^2\Delta y^2 + \delta y^2/4)^{1/2}$. This is similar to the phenomenological approach used in proceeding from Eq. (12) to Eq. (13). The added term removes the infinity and gives us the correct result when $\Delta y = 0$. At the same time it is negligible for all off-axis values of Δy that will be of interest. The appropriate expression is then

$$\Delta P \simeq \Sigma I_o W \delta y \sigma(0) \ell n[(F^2 + k^2a^2\Delta y^2)/(\delta y^2/4 + k^2a^2\Delta y^2)]^{1/2} \quad . \tag{16}$$

The results of Eqs. 13 and 16 give the detected scattered power from converging, SAW diffracted rays in the spectrum-analyzer configuration of Fig. 13. The same formulas may be used to calculate the scattered power from undiffracted rays once appropriate changes for the terms I_o and Δy are incorporated. If η is the acoustooptic diffraction efficiency and I_o is the diffracted power per unit beam width, the undiffracted power per unit beam width is I_o/η. Similarly, if ψ is the angle between the diffracted and undiffracted beams ($\psi = 3°$ in Fig. 13), and Δy is the value of detector position relative to the optical axis of the diffracted beam, then

$$I_o \rightarrow I_o/\eta \quad ,$$

$$\Delta y \rightarrow F\tan\psi - \Delta y \quad , \tag{17}$$

are the substitutions to make in Eqs. (13) and (16) to describe the detected scattered power from the undiffracted beam. For the geometry of Fig. 13, the value of F tanψ is 943 μm, while the largest value of Δy is that for the +50th detector, 400 μm.

Contribution to Scattered Power from the Unfocused Beams

Light scattered before the lens at an angle ϕ is focused by the lens onto the detector array at position $y' = F\tan\phi$. (As before, we begin by considering only the contribution of the SAW diffracted beam.) The scattering angle subtended by each detector is approximately $\delta y/F$. The power intercepted from a single scattering event is $I_o\sigma(\phi)\delta y/F$. Since the total number of scattering centers in the front focal region is ΣWF, the total scattered power detected is

$$\Delta P = \Sigma I_o W \delta y \sigma(\phi) \tag{18}$$

The angle dependence of $\sigma(\phi)$ is that of Eq.(9), for Rayleigh scattering, and Eq. (10) for RGD scattering.

This expression for scattered power from the SAW side of the lens applies to the undiffracted beam when I_o is replaced by I_o/η and ϕ is replaced by $\psi-\phi$. From Fig. 13, the on-axis detector receives light from the undiffracted beam that has been scattered at $\psi = 3°$. Consequently the ϕ dependence of Eq. (18) is not significant for Rayleigh scattering, which is wide angle, though for RGD scattering it could result in a gradual decrease in scattered power across the detector array.

Total Contribution to On-Axis Scattered Power

The total scattered power is obtained by summing the contributions from the diffracted and undiffracted beams, both before and after the beams pass through the lens. At first glance, one might anticipate that the dominant contribution comes from the portion of the undiffracted beam scattered on the detector-array side of the lens. The undiffracted beam is more intense than the diffracted beam by a factor of $1/\eta$, while scattering on the array side of the lens is detected in greater amounts because of the larger acceptance angle of the detector elements.

For this contribution the power intercepted by the central detector is calculated from either Eq. (13) or (16), depending on the type of scattering, after making the substitutions $I_o \rightarrow I_o/\eta$ and $\Delta y \rightarrow F\tan\psi - \Delta y$ (= $F\tan\psi$ for the central

detector element). We summarize the results using an approximation valid when $\tan\psi \ll 1$, as is the case in practice:

$$\Delta P = \Sigma(I_o/\eta)W\delta y\sigma(0) \qquad (19)$$

$$\times \ell n[(1/M\tan\psi)(1 + M^2\tan^2\psi)^{1/2}] \quad ,$$

where $M = k\alpha$ for the RGD limit ($k\alpha \gg 1$) and $M = 1$ for the Rayleigh limit ($k\alpha \ll 1$). Taking $\psi = 3°$, $k = 2\pi(2.2)/.633\ \mu m = 21.8\ \mu m^{-1}$, and $\alpha = 10\ \mu m$, we find that the logarithmic term above has the value 2.95 in the Rayleigh limit and 0.0038 in the RGD limit.

In the Rayleigh limit, then, scattering from the post-lens region is only about three times as great as that from the pre-lens region, where the logarithmic term in Eq. (19) is replaced by unity in accord with Eq. 18. With $\eta = 10\%$, the total on-axis scattered power from the undiffracted beam in the Rayleigh limit is close to

$$\Delta P \simeq 39.5\ \Sigma I_o W\delta y\sigma(0) \quad . \qquad (20)$$

The numerical factor 39.5 is the result of $(2.95 + 1.0)/\eta$.

In the RDG limit, the value of the logarithmic term in Eq. (19) is small enough to suggest that other contributions to scattering dominate that from the undiffracted beam on the output side of the lens. The contribution from scattering of the undiffracted beam on the input side of the lens is an expression similar to Eq. (19) except that the logarithmic term is replaced by $[1 + k^2\alpha^2\psi^2]^{-1}$ (see Eqs. (10) and (18)). In the numerical example chosen, this factor is found to be 0.0076, up from 0.0038 but still small. If $\eta = 10\%$, the total scattering contribution from the undiffracted wave is

$$\Delta P \simeq 0.114\ \Sigma I_o W\delta y\sigma(0) \quad , \qquad (21)$$

where $0.114 = (0.0076 + 0.0038)/\eta$.

In view of this small value, let us now consider the on-axis scattering contribution from the SAW-diffracted wave. Taking the sum of Eqs. (16) and (18) accounts for scattering generated both before and after the lens. For the central detector, we have

$$\Delta P = I_o W \delta y \sigma(0)[1 + \ell n 2F/\delta y] \tag{22}$$

The quantity in brackets is 9.88 for the parameters of Fig. 13. This is two orders of magnitude greater than the scattering contribution from the undiffracted wave. This imbalance is caused by the assumed large size of the scattering centers, a = 10 μm, which results in a highly localized scattered energy distribution. If a = 1 μm, the contributions from the diffracted and undiffracted beams are comparable. Similarly, if η = 1% instead of 10%, the relative undiffracted-beam contribution increases on order of magnitude and may exceed the diffracted-beam contribution.

Note that the result of Eq. (22) is a valid expression for the diffracted-beam contribution to scattering in both the Rayleigh and RGD limits. Consequently it may be added to Eq. (20) to obtain the total on-axis scattered power in the Rayleigh limit from diffracted and undiffracted beams, both before and after the lens:

$$\Delta P(\text{Rayleigh}) = 49.4\ \Sigma I_o W \delta y \sigma(0). \tag{23}$$

In the RGD limit, we had from Eq. (22)

$$\Delta P(\text{RGD}) = 9.9\ \Sigma I_o W \delta y \sigma(0)\ . \tag{24}$$

The numerical coefficient will always be at least as large as 1 + $\ell n 2F/\delta y$, contributed from the diffracted beam, and it may be larger if the angular spread of scattering is as large as the angle ψ between diffracted and undiffracted beams. Generally this will be the case for Rayleigh scattering. In the following discussion we will write

$$\Delta P = Q \Sigma I_o W \delta y \sigma(0) \tag{25}$$

where $Q \simeq 10$ for the large-particle RGD limit and $Q \simeq 100$ for the small-particle Rayleigh limit.

Calculation of Dynamic Range

The dynamic range of a spectrum analyzer is the amount that the peak diffracted signal must be attenuated to equal the noise associated with scattered light. For a uniform beam of width W and power per unit width I_o, the power per unit width in the Fourier transform plane is

$$I(y') = I_o(W^2/F\lambda)\ \mathrm{sinc}^2(y'W/F\lambda), \tag{26}$$

where $\mathrm{sinc}z = \sin\pi z/\pi z$. The width of the central peak of the Fourier transform distribution is $2F\lambda/W$. For a spectrum analyzer having the geometry of Fig. 13 F = 18 mm and W = 7.2 mm. With $\lambda = (0.633/2.2)\ \mu m = 0.29\ \mu m$ the width of the central peak is about 1.4 μm. This is considerably less than the 5 μm detector aperture. The detected power is therefore essentially the total power in the diffracted but unscattered incident beam:

$$P_o = I_o W \quad . \tag{27}$$

The dynamic range is

$$P_o/\Delta P = [Q\delta y\sigma(0)]^{-1} \quad . \tag{28}$$

The factor $Q\delta y$ in this expression is somewhat under control of the design engineer. Provided that scattering from the undiffracted beam is negligible, we have

$$Q\delta y = [1 + \ell n 2F/\delta y]\delta y \quad . \tag{29}$$

This goes to zero as δy goes to zero. However, δy = 5 μm as used in Fig. 13 is probably close to the state of the art. In that case, improvement in dynamic range is afforded by keeping F as small as possible. F = 18 mm in Fig. 13 is also a reasonable small value. We conclude that the design of Fig. 13 is close to optimum from the point of view of maximizing system dynamic range.

CALCULATION OF DIFFERENTIAL SCATTERING CROSS SECTIONS

In order to further analyze spectrum-analyzer dynamic range it is necessary to develop expressions for the on-axis value of the differential scattering cross section $\sigma(0)$. This problem was addressed in Ref. 1 from a rigorous point of view, though ultimately approximations were introduced that limited the analysis to the Rayleigh-Gans-Debye limit; that is, $ka>>1$ and $ka\delta n<<1$, where δn is the effective index perturbation of the scattering particle. In this work we prefer to limit the rigor of the analysis but to preserve its physical content as much as possible. The objective is to produce simple but physically sound formulas for use in predicting spectrum-analyzer performance in a variety of scattering situations. In addition, we hope to extend the results of Ref. 1 to include the Rayleigh limit of scattering by small particles.

Differential Scattering Cross Sections in the Rayleigh Limit

Figure 15 shows a schematic drawing of dipole scatters distributed throughout a waveguide layer of depth D. If we ignore the effects introduced by the waveguide geometry, the total scattering cross section is[22]

$$\sigma_{tot} = (8\pi/3)k^4a^6(m^2-1)^2/(m^2+2)^2 \quad , \tag{30}$$

where a is the scattering center radius, $m = (n+\delta n)/n$, and n is the refractive index. The ratio of the terms containing m is approximately equal to $(4/9)\delta n^2/n^2$ when the index perturbation satisfies $\delta n<<n$. However, this is a fair approximation even when the scattering centers are voids in the waveguide layer, having $n+\delta n = 1.0$ and, for $LiNbO_3$, $n = 2.2$. Therefore we use the approximation for all δn of interest, writing

$$\sigma_{tot} = (8\pi/3)(4/9)k^4a^6\delta n^2/n^2 \quad . \tag{31}$$

The differential scattering cross section is reduced by a factor $(8\pi/3)$ and multiplied by the polarization factor $\cos^2\phi$, where $\pi/2-\phi$ is the angle between

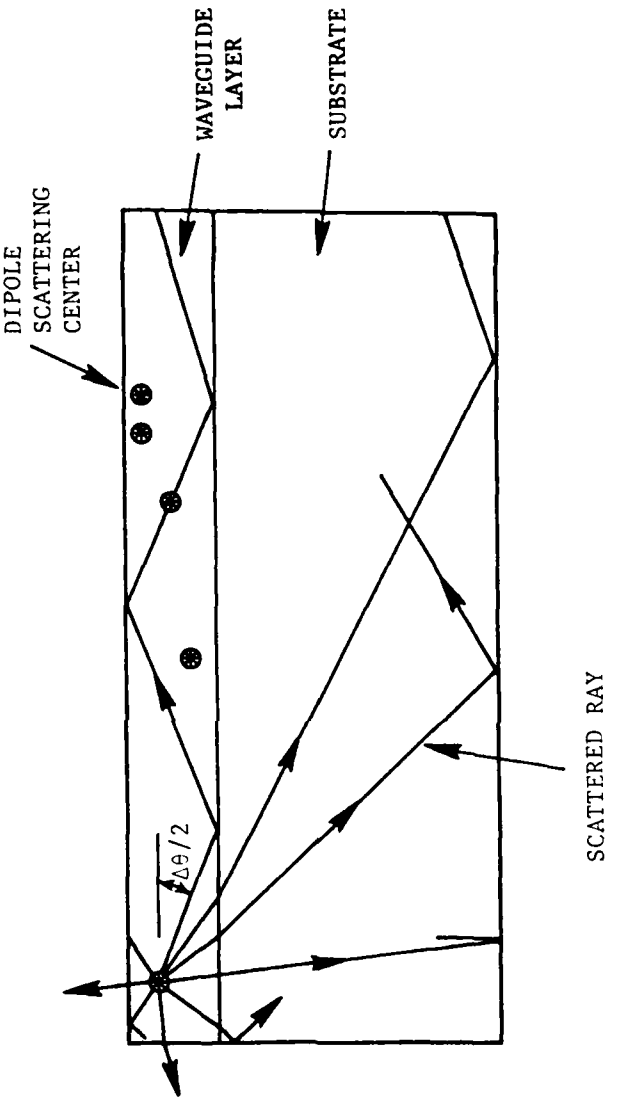

Fig. 15. Schematic drawing of dipole scattering centers confined to the waveguide layer. $\Delta\theta$ = full acceptance angle of the waveguide.

the scattering direction and the incident polarization. In the problem we are considering, that of in-plane forward scattering, $\phi = 0°$ and we have

$$\sigma_{dif} = (4/9)k^4 a^6 \delta n^2/n^2 \tag{32}$$

as the relevant differential scattering cross section. Note that σ_{tot} and σ_{dif} both have dimensions of area, whereas $\sigma(0)$ of the previous subsections had dimensions of length. This disparity will be remedied when we take into account the reduced dimensionality of the waveguide geometry.

For a single scattering center, the amount of light scattered into a solid angle $\Delta\Omega$ is

$$\Delta P = (I_o/D)\sigma_{dif}\Delta\Omega \quad , \tag{33}$$

where D is the waveguide depth and I_o/D is the appropriate power per unit cross sectional area in the waveguide layer. We are interested in the solid angle subtended by a waveguide detector. Since light scattered into the substrate is presumed not to be detected, we need consider only solid angles that are bounded by the acceptance angle of the waveguide. This angle, $\Delta\theta$, is defined by Fig. 15 and is found using Snell's Law to be given by

$$\Delta\theta \simeq 2(2\Delta n/n)^{1/2} \quad , \tag{34}$$

where Δn is the index perturbation of the waveguide, assumed small in comparison to the substrate index n. If the detector subtends an angle $\Delta\phi$ measured in the plane of the waveguide, the included solid angle is $\Delta\Omega = \Delta\theta\Delta\phi$, or

$$\Delta\Omega = 2(2\Delta n/n)^{1/2}\Delta\phi \quad . \tag{35}$$

The detected power is obtained from Eq.(33):

$$\Delta P = 2f(I_o/D)\sigma_{dif}(2\Delta n/n)^{1/2}\Delta\phi \tag{36}$$

A factor f has been added to account for the fact that only a fraction of rays emitted within the acceptance angle of the waveguide is trapped in waveguide modes.

By comparison with Eq. (1), the in-plane differential cross section to be used in the previous formulas of this section is

$$\sigma(0) = 2f(\sigma_{dif}/D)(2\Delta n/n)^{1/2} \quad . \tag{37}$$

This has the correct dimension of length. Eq. (28) for dynamic range depends on the product $\Sigma\sigma(0)$ where Σ is the number of scatters per unit waveguide area. If ρ is the volume density of scatters in the waveguide, then $\Sigma = \rho D$ and

$$\Sigma\sigma(0) = \rho\sigma_{dif}(2\Delta n/n)^{1/2} \quad . \tag{38}$$

We have, for simplicity, taken $f \simeq 1/2$. Eq. (38) can be cast in terms of the attenuation coefficient of the waveguide, $\alpha = \rho\sigma_{tot}$, using $\sigma_{dif} = \sigma_{tot}/(8\pi/3)$. We find for the spectrum analyzer dynamic range,

$$P_o/\Delta P = [Q\delta y(3/8\pi)\alpha(2\Delta n/n)^{1/2}]^{-1} \tag{39}$$

For $Q = 100$, $\delta y = 5$ μm, $\alpha = 1$ dB/cm, $\Delta n = 0.007$ and $n = 2.2$ we find

$$P_o/\Delta P(\text{Rayleigh}) = 39.6 \text{ dB} \quad . \tag{40}$$

If waveguide losses can be reduced to 0.1 dB/cm, the dynamic range improves to nearly 50 dB. This result is very encouraging, but is is based on the assumption that only Rayleigh scattering exists in the waveguide. Other scattering present can degrade the level of performance, as we now discuss.

Differential Scattering Cross Sections in the Rayleigh-Gans-Debye Limit

We consider scattering centers which are much larger than a wavelength (Mie scattering), yet which are optically soft (RGD limit). This means that the field inside the scattering center is essentially the same as the incident field, and the effect of the scattering center is simply to perturb the wavefront of the incident light by an amount small compared to a wavelength. These requirements are satisfied when $ka \gg 1$ and $k_o a\delta n \ll 1$, where δn is the index perturbation associated with the scattering center.

Figure 16 defines the geometry of the problem we are considering. If $A_o e^{ik_o n_\rho(z_o - a/2)}$ is the incident wavefront, the wavefront at the trailing edge of the scattering center is

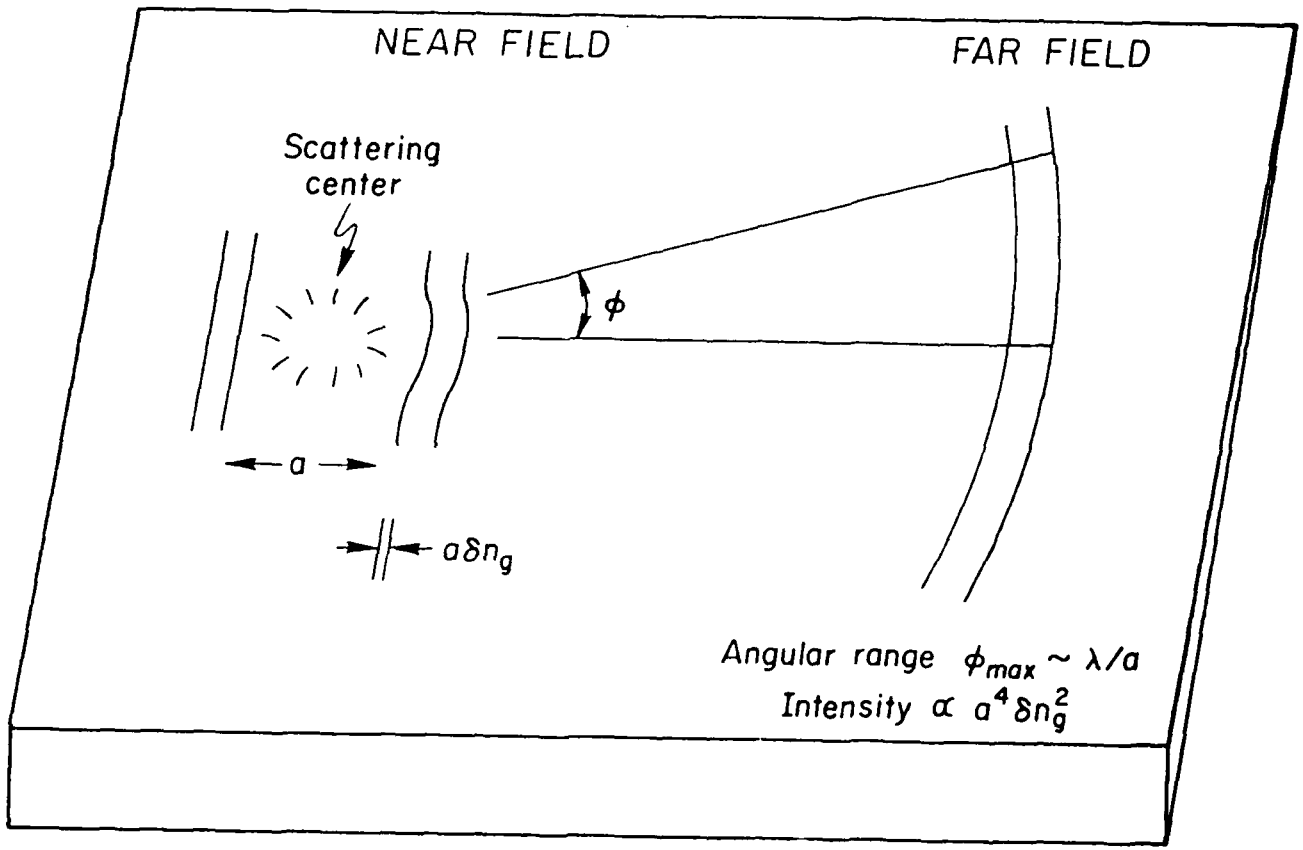

Fig. 16. Geometry for scattering analysis in the Rayleigh-Debye Limit.

$$A = A_o \exp\{ik_o n_g (z_o - a/2) + ik_o \int_{z_o-a/2}^{z_o+a/2} dz n_g(y,z)\} . \quad (41)$$

where $k_o = 2\pi/\lambda_o$, λ_o is the free-space wavelength, and $n_g(y,z)$ is the perturbed mode index in the scattering region. If we take $n_g(y,z) \approx n_g + \delta n_g(y,z)$, the field may be written

$$A = A_o e^{ik_o n_g (z_o + a/2)} \{1 + [\exp(ik_o \int_{z_o-a/2}^{z_o+a/2} dz \delta n_g(y,z)) - 1]\} . \quad (42)$$

The term in square brackets describes the perturbed wavefront. Its variation along the y axis depends on the shape and index of the scattering center and in general will be quite complicated. To keep the analysis simple and yet preserve its important features, we take $\delta n_g(y,z)$ to be a rectangular function,

$$\delta n = \text{constant for } z_o - a/2 < z < z_o + a/2$$

$$y_o - a/2 < y < y_o + a/2 ,$$

$$\delta n_g = 0 \text{ elsewhere.} \quad (43)$$

We also assume $k_o a \delta n_g << 1$. The perturbation field is then

$$A = A_o e^{ik(z_o + a/2)} i k_o a \delta n_g \quad \text{in} \quad y_o - a/2 < y < y_o + a/2,$$

$$= 0 \text{ elsewhere.} \quad (44)$$

The scattered field in the far zone is obtained through a straightforward application of Fraunhofer diffraction theory:[23]

$$A(y,z) = A_o e^{ik(z_o + a/2)} ik_o a \delta n_g [i\lambda(z - z_o)]^{-1/2} e^{ikr} \int_{-a/2}^{a/2} e^{iky'\phi} dy' . \quad (45)$$

The parameters of the problem are defined with respect to Fig. 17: (y,z) are the coordinates of the observation point, and are such that $y >> y_o$, $z >> z_o$; r is

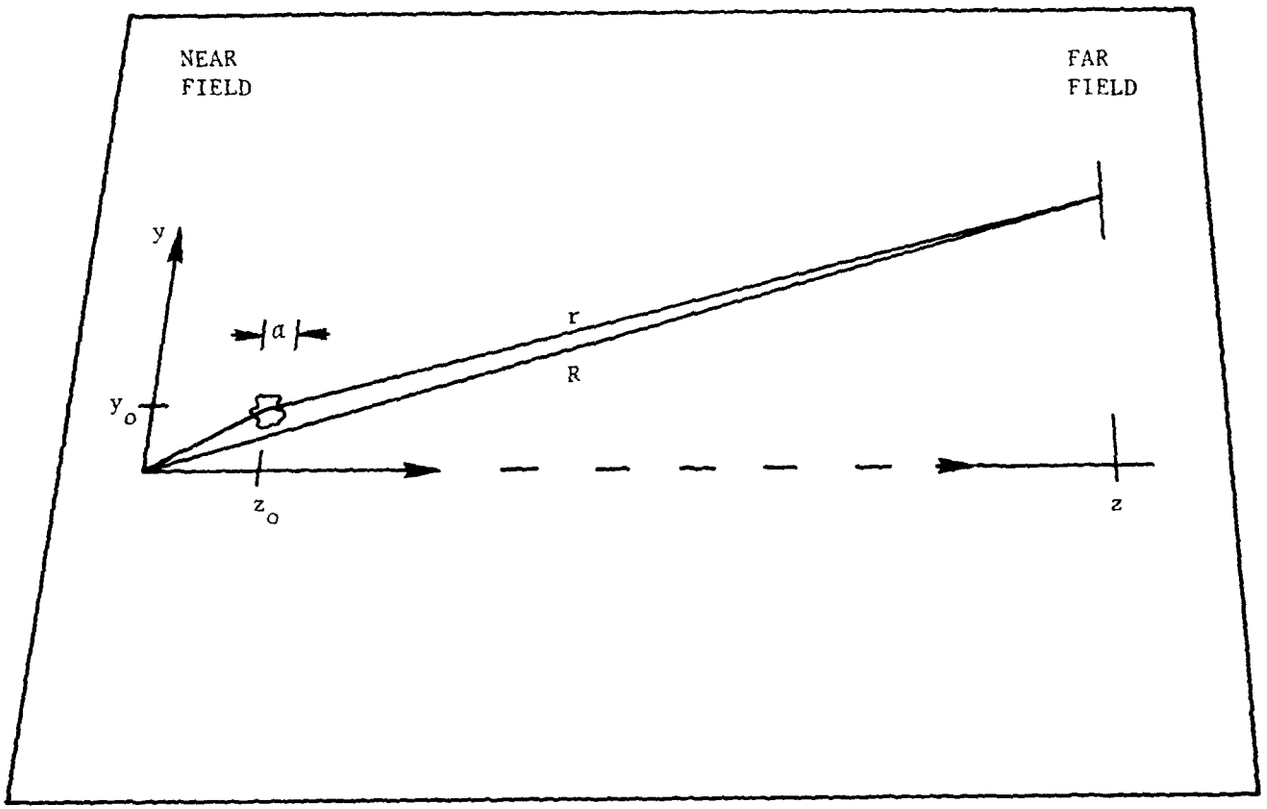

Fig. 17. Definition of parameters for determining the scattered field in the Fraunhofer zone.

the distance of the observation point from the scattering center and ϕ is the scattering angle, assumed to be small. The integral in Eq. (45) has the value $a\,\mathrm{sinc}(a\phi/\lambda)$. Finally, the distance r is given by

$$r \simeq R - y_o \sin\phi - z_o \cos\phi \quad , \tag{46}$$

where R is the distance of the observation point from the origin of coordinates. Using these results to substitute in Eq. (45), we have, in polar coordinates,

$$A(R,\phi) = A_o e^{ikR}(i\lambda z)^{-1/2} ik_o a^2 \delta n_g \,\mathrm{sinc}(a\phi/\lambda)$$
$$e^{-iky_o\sin\phi + ikz_o(1-\cos\phi)} \quad . \tag{47}$$

The last term on the right contains phase information associated with the location of the scattering center. The other terms are common to all scattering centers in the scattering region. We may replace $A(R,\phi)$ by the field $A_i(R,\phi)$ for the ith scattering center located at coordinates (y_i,z_i). The total scattered field is then

$$E(R,\phi) = \sum_i A_i(R,\phi) \tag{48}$$

and the scattered intensity is proportional to

$$EE^* = A_o^2 (k_o a^2 \delta n_g)^2 (\lambda z)^{-1} \mathrm{sinc}^2(a\phi/\lambda) S(\phi) \ ,$$
$$S(\phi) = \left| \sum_i e^{-iky_i\sin\phi + ikz_i(1-\cos\phi)} \right|^2 \quad . \tag{49}$$

The summation term may be written

$$S(\phi) = N + \sum_{i\neq j} e^{-ik(y_i-y_j)\sin\phi + ik(z_i-z_j)(1-\cos\phi)} \quad . \tag{50}$$

where N is the total number of scattering centers. The maximum value is $S(0) = N^2$. However the terms in the sum will begin to add incoherently at angles for which the maximum values of $k(y_i-y_j)\sin\phi$ or $k(z_i-z_j)(1-\cos\phi)$ approach unity. Since this will occur at angles comparable to or less than $\phi \simeq 1/kW$, the beam diffraction angle, the coherent contribution to scattering cannot be resolved experimentally. At larger values of ϕ than 1/kW, the exponents of some terms in Eq. 50

are large and the value of $S(\phi)$ quickly falls toward an average value of N. Coherent addition could occur at nonzero values of ϕ if the scattering centers were arrayed in a periodic lattice, but for random scattering center locations we have not been able to observe even partial evidence of coherent scattering when the sum of Eq. 50 is generated on a computer. Nor have we observed any enhanced scattering at nonzero scattering angles in our experimental work.

This does not mean that $S(\phi)$ exhibits no significant fluctuations with ϕ. Consider a short scattering path length L so that

$$S(\phi) \simeq N + \sum_{i>j} 2\cos[k(y_i - y_j)\sin\phi] \quad . \tag{51}$$

We have cast the sum in terms of the real-valued cosine function and thereby reduced the number of terms to $(N^2-N)/2$. For a given value of $\sin\phi \simeq \phi >> 1/kW$, at least some arguments of the cosine functions in Eq. (57) will be large compared to unity. If we assume that the arguments populate the interval $0<\arg<(kW\sin\phi>>1)$ in a manner which is uniform and random, the cosine function assigns to each argument a positive or negative number in the range 0 to 1 or 0 to -1 with approximately equal probability. We simplify the problem by averaging the values of the cosine function in these ranges, so that each term in the sum is taken to have the value $+4/\pi$ or $-4/\pi$. This reduces the problem to that of the well-known random walk in one dimension. We have $(N^2-N)/2$ terms that are valued either $+4/\pi$ or $-4/\pi$ in a random fashion, such as might be determined by flipping a coin. The average value of such an ensemble is 0. Hence $\langle S(\phi)\rangle = N$. However, statistical fluctuations are such that values on the order of $S(\phi) = N \pm [N^2-N)/2]^{1/2}$ might well be observed at typical values of ϕ. Thus, S fluctuates between $S_+ \simeq N(1+2^{-1/2})$ and $S_- \simeq N(1-2^{-1/2})$ for large N. The ratio $S_+/S_- = 5.83$ shows that fluctuations in the scattered signal about the average could easily amount to 7.7 dB.

Let us define $NR(\phi)$ to be the randomly fluctuating component of $S(\phi)$, so that

$$S(\phi) = N[1+R(\phi)] \quad . \tag{52}$$

When this relation is substituted into Eq. (49), we have

$$EE^* = A_o^2 N(k_o a^2 \delta n_g)^2 (\lambda z)^{-1} \mathrm{sinc}^2(a\phi/\lambda)[1+R(\phi)] \tag{53}$$

The ϕ dependence of scattering is contained in the final two terms. The average variation of the scattered intensity is contained in the $\text{sinc}^2(a\phi/\lambda)$ term. However this function itself has structure that results from our unphysical assumption of a single particle size a for scattering centers, when a distribution of sizes is more realistic. The envelope of the sinc^2 function would therefore appear to be a more physically meaningful quantity in Eq. (53) The envelope has a value of unity at $\phi = 0$ and a value near $(\pi a\phi/\lambda)^{-2}$ at large ϕ. A Lorentzian distribution, $[1+(\pi a\phi/\lambda)^2]^{-1}$, has both these functions. In fact, the derivation of Ref. 1, based on the approach of Marcuse [3] and very different in spirit from the derivation here, shows a Lorentzian variation with ϕ, namely $[1+(2\pi a\phi/\lambda)^2]^{-1}$. Note that the coefficient of ϕ is a factor of two greater than that obtained using our heuristic analysis. The discrepancy originates in the statistical treatment used in Ref. 1 to account for the random distribution of scattering centers. The same treatment results in a scattered amplitude twice that found in Eq. (47). Incorporating both these features to preserve consistency with Ref 1, we have

$$EE^* = 4A_o^2 N(k_o a^2 \delta n_\rho)^2 (\lambda z)^{-1} L(ka\phi)[1+R(\phi)]$$

$$L(ka\phi) = [1+(ka\phi)^2]^{-1} \quad . \tag{54}$$

This expression is readily converted into experimental intensity parameters using the relation $I_{scat}/I_o = EE^*/A_o^2$. If the scattered light is measured using a detector of width δy, the detected power is $\Delta P = I_{scat}\delta y = I_o EE^* \delta y/A_o^2$. From Eq. (54) we have

$$\Delta P = 4I_o N(k_o a^2 \delta n_g)^2 \lambda^{-1} (\delta y/z) L(ka\phi)[1+R(\phi)] \tag{55}$$

The term $(\delta y/z)$ is just $\Delta\phi$, the angular acceptance of the detector, while N, the number of scattering centers, is ΣLW, where L and W are the length and width of the scattering area, respectively. Making these substitutions in Eq.(55), we find

$$\Delta P = \Sigma LW\, I_o\, \sigma(\phi)\, \Delta\phi$$

$$\sigma(\phi) = (2/\pi)^{-1} n\, k_o^3 a^4 \delta n_g^2 L(ka\phi)[1+R(\phi)] \tag{56}$$

The latter expression is the differential scattering cross section in the Rayleigh-Gans-Debye limit.

Let us use the results of Eq. (56) to estimate the dynamic range of a spectrum analyzer. The formula is that of Eq. (28), with $Q \approx 10$ for the case of RGD scattering. As a worst-case situation let us take $\Sigma = a^{-2}$; that is, scattering centers are contiguous. There is no space between them. Further, let us take $\delta y = 5$ μm, $a = b = 10$ μm, $n = 2.2$, $k_o = 2\pi/0.633$ μm, and $\phi = 0 = R(0)$. The resulting on-axis dynamic range is

$$P_o/\Delta P = 1.46 \times 10^{-7} \delta n_g^{-2} \quad . \tag{57}$$

To achieve a 40 dB dynamic range or better, it is necessary that $\delta n_g \leq 0.38 \times 10^{-5}$. This is to be compared with $\Delta n \leq 10^{-2}$ for the index change at the surface of $LiNbO_3$ Ti-diffused waveguides.

Calculation of δn_g

Thus far we have made no assumption about the origin of δn_g. Hence we cannot comment on its magnitude. In this subsection we calculate δn_g in terms of waveguide and scattering parameters for several physical models of scattering beginning with surface roughness.

Surface-Roughness Scattering. We model the effects of surface roughness on scattering by considering the rough surface to be associated with a randomly fluctuation waveguide thickness D. If $n_g(D)$ is the effective mode index, the rms fluctuation of n_g associated with a surface having rms roughness σ is

$$\delta n_g = (\partial n_g/\partial D)\sigma \quad . \tag{58}$$

Our problem reduces to an analysis of the waveguide dispersion equation to obtain a formula for $\partial n_g/\partial D$ in terms of k_o, $\Delta n = n_1 - n_2$, and D, where $n_1(n_2)$ is the surface (substrate) refractive index.

Let us base our discussion on the analysis of Hocker and Burns for diffused optical waveguides.[24] They derive a set of universal curves which relate a normalized mode index

$$b = (n_g^2 - n_2^2)/(n_1^2 - n_2^2) \tag{59}$$

to a normalized waveguide depth,

$$V = k_o D(n_1^2 - n_2^2)^{1/2} \quad . \tag{60}$$

The desired quantity is

$$\partial n_g/\partial D = (\partial n_g/\partial b)(\partial b/\partial V)(\partial V/\partial D) \quad . \tag{61}$$

The second term on the right, $\partial b/\partial V$, is just the slope of the universal curve, while the third term is

$$\partial V/\partial D = k_o(n_1^2 - n_2^2)^{1/2} \simeq k_o(2n_2\Delta n)^{1/2} \quad . \tag{62}$$

The first term is obtained by inverting the derivative of Eq. 59:

$$\partial n_g/\partial b = (n_1^2 - n_2^2)/2n_g \simeq \Delta n \quad . \tag{63}$$

Consequently, Eq. 61 reduces to

$$\partial n_g/\partial D = k_o \Delta n(2n_2\Delta n)^{1/2}(\partial b/\partial V) \quad . \tag{64}$$

To complete the solution to the problem, one works from a knowledge of waveguide fabrication procedures to select the appropriate universal curve b(V) and the correct operating point $b = b(V_o)$. The slope of the curve at the operating point $b'(V_o)$ is inserted into Eq. (64) to specify the derivative $\partial n_g/\partial D$. Using the universal curve for a Gaussian index profile, and taking $V_o = 4.45$, the largest value possible for a single mode waveguide, we have $\partial b/\partial V = 0.10$. With $k_o = 2\pi/0.633\ \mu m$, $n_g = 2.2$ and $\Delta n = 0.007$, the derivative $\partial n_g/\partial D$ is 1.23×10^{-7} $\mathring{A}^{-1}$. The largest value of the derivative for a single-mode guide occurs with $V = 2.70$, and is only 2.6 times the above value. We have measured the slopes used in these calculations directly from a set of universal curves provided in a preprint of Ref. (7) obtained from the first author. It appears that values of δn_g on the order of 10^{-5} can be obtained with surfaces as rough as 100 Å rms. Using Eq. 57 for dynamic range in conjunction with our result $\delta n_g = \sigma 1.23 \times 10^{-7}$ $\mathring{A}^{-1}$, we find $\sigma = 31$ Å associated with a dynamic range of 40 dB. This, however, is not a particularly good polish. An average polish having $\sigma = 10$ Å is consistent with a dynamic range of 50 dB, and a 3.2 Å surface roughness is consistent with an 60 dB dynamic range. These results offer encouragement with

regard to the possibility of reducing surface-roughness scattering to negligibly important levels.

Before moving on, we present a derivation of $\delta n_g = \sigma(\partial n_g/\partial D)$ for a strongly asymmetric slab waveguide. For strong asymmetry the superstrate index n_o is not close to n_1 or n_2 in magnitude. As a result, terms dependent on n_o can be eliminated from the model dispersion equation. For TE modes, the dispersion equation can be simplified to

$$V = -(1-b)^{-1/2}\tan^{-1}(b^{-1}-1)^{1/2} \quad . \tag{65}$$

The derivative of this equation with respect to V is

$$1 = (1/2)(db/dV)(1-b)^{-1}[b^{-1/2}-(1-b)^{-1/2}\tan^{-1}(b^{-1}-1)^{1/2}] \quad . \tag{66}$$

The last item in brackets can be replaced by its equivalent, V, using Eq. (65). Combining this result with Eqs. (61), (62), (63), and (58), we obtain

$$\delta n_g = k_o\sigma\, 2\Delta n(2n_2\Delta n)^{1/2}(1-b)(b)^{1/2}$$

$$x[k_o D(2n_2\Delta nb)^{1/2}+1]^{-1} \tag{67}$$

One may wish to insert this result directly into Eq. (56) to obtain an expression for differential scattering cross section $\sigma(\phi)$ in terms of waveguide and roughness parameters alone. Such an expression was derived in Ref. 1 using a more rigorous approach. If the two agree, it adds credence to the present results. We begin with Eq. (14) of Ref. 1 and insert the results of Eqs. (9), (23), and (20) of that reference to obtain

$$dP/d\phi = P(2\pi/\beta_o)(k_o^4/16\pi^2)(n_1^2-n_o^2)^2\sigma^2E_o^4(0)(\beta_o/2\omega\mu_o P)^2$$

$$x4N\alpha^4H(\phi) \tag{68}$$

In our current notation, we have replaced P by I_o on the right hand side above, where I_o is power per unit waveguide width. This is done to avoid confusion with dP, which was and is an increment of power. Also $\beta_o = n_g k_o \simeq n_2 k_o$ is the magnitude of the wavevector of the waveguide mode, μ_o is the vacuum permeability, ω is $2\pi\nu$, ν is the optical frequency, $E_o(0)$ is the waveguide field at the surface, and $N = \Sigma LW$ is the number of scattering centers. Our current

definition of the differential scattering cross section is

$$\sigma(\phi) = (I_o \Sigma LW)^{-1}(dP/d\phi) \tag{69}$$

This is different from that of Ref. 1 by the inclusion of the scattering center density Σ in the denominator. Eq. (68) gives us the information necessary to write an expression for $\sigma(\phi)$. However, it is useful to first express the field at the surface $E_o(0)$ in terms of physical waveguide parameters.[25] For the strongly asymmetric waveguide we are considering, the field is approximately given by

$$E_o^2(0) \simeq 4(1-b)(n_1^2-n_o^2)^{-1}(\omega\mu_o I_o/\beta_o)k_o b^{1/2}(2n_2\Delta n)^{3/2}$$

$$x(Vb^{1/2}+1)^{-1} \quad . \tag{70}$$

Using Eq. (67), this result may be rewritten as

$$E_o^2(0) = (\omega\mu_o I_o/\beta_o)2(n_1^2-n_o^2)^{-1}(\delta n_g/\sigma\Delta n)(2n_2\Delta n) \tag{71}$$

Upon inserting this expression into Eq. (68) and then inserting Eq. 68 into (69), we find

$$\sigma(0) = (2/\pi)n_2 k_o^3 a^4 \delta n_g^2 \tag{72}$$

This agrees with our heuristic result of Eq. 56. We conclude that the derivations of this section are theoretically sound. In particular, the critical assumption that the effect of large scattering centers can be expressed in terms of the mode index perturbation δn_g appears correct.

Volume Scattering. In this subsection we consider first the model for large volume scattering centers that was introduced in Ref. 1. The scattering centers are assumed to have an index different from their surroundings by an amount δn.

This model for volume scattering might be expected to describe fluctuations in the Ti concentration or in the stoichiometry of the host $LiNbO_3$ material. One source of scattering that we have considered is that of gaps in the waveguide layer caused by dust particles trapped beneath the Ti film prior to diffusion.[1] At the high temperatures of diffusion, these may explode and effect the removal of Ti from the surface, leaving a void in the waveguide Ti distribution.

In this case $n_1 = n_2$ in the vicinity of the scattering center; that is, there is no waveguide (we ignore outdiffusion). We have

$$\delta n_g = n_g - n_2 \simeq b\Delta n \ . \tag{73}$$

By combining Eq. 56 with Eq. 28, and taking Q = 10, n = 2.2, $k_o = 2\pi/0.633$ μm, and $\delta n_g = b\Delta n$, we find that the on-axis dynamic range is given by

$$P_o/\Delta P = 1.46 \times 10^{-5} \ \mu m^2/a^4 \Sigma \, b^2 \Delta n^2 \tag{74}$$

We will take $a \simeq 1$ μm as the largest dust particles which are difficult to locate on a surface and difficult to remove because of electrostatic forces. Similarly, we will take $b\Delta n \simeq 0.003$ as the largest value of the index inhomogeneity associated with Ti gaps in the waveguide. Then for a 40 dB dynamic range we find a density of scattering centers of $\Sigma = 162 \ mm^{-2}$.

This is a rather dirty surface, probably not encountered in careful practice. If Σ is reduced two orders of magnitude to a more reasonable level of 1.6 mm^{-2}, the dynamic range is increased to 60 dB. If $\Sigma = 0.2\ mm^{-2}$, while $a = 3\ \mu m$, the dynamic range is 50 dB. We conclude that scattering from Ti gaps in the waveguide is not likely to impair spectrum-analyzer performance provided care is taken in waveguide preparation.

Other volume scattering centers discussed in Sec. III had to do with the occurrence of the separated phase $LiNb_3O_8$ and Li-Ti-O compounds like $Li_2Ti_3O_7$ during waveguide fabrication.[14,7] The index of refraction associated with these species is likely to differ by $\delta n = 0.1$ or more from that of the host species. This is generally too large to qualify as RGD scattering, and will be treated later as Mie scattering.

However, if the scattering centers are confined near the waveguide surface to within a depth $z_o << D$, the effective index is likely to be reduced from δn because of the poor overlap with the waveguide electric field.

From the discussion following Eqs.(2) and (6) of Ref. 1, the scattering parameter η_o of that reference is calculated from

$$\eta_o = (k_o n_2/2\omega\mu_o I_o) 2n_2\delta n \int_o^{z_o} dz E_o^2(z) \tag{75}$$

where z_o is the depth of the scattering inhomogeneity and $E_o(z)$ is the normalized electric field. We have been considering $z_o = a >> D$, the waveguide depth. In this case $\eta_o = 2n_2\delta n$ results from replacing z_o by ∞ in Eq.(75). For the case we now consider, $z_o << D$ and

$$\eta_o = (z_o/D)(4n_2\Delta n)(n_1^2 - n_o^2)^{-1} 2n_2\delta n[Vb^{1/2}/(Vb^{1/2}+1)] \tag{76}$$

In deriving this result, we have approximated the integral in Eq.(75) as $z_o E_o^2(0)$, where $E_o^2(0)$ is given by Eq.(70). For cases of interest, $V \simeq 3$ and $b = 0.2$, the quantity in square brackets above is about 1/2 in value. Use of this simplification along with $n_2 = 2.2$ and $\Delta n = 0.007$ gives us

$$\eta_o = 8.0 \times 10^{-3}(z_o/D) 2n_2\delta n \quad . \tag{77}$$

In other words the scattering perturbation is reduced by a factor 8×10^{-3} (z_o/D) from the case $z_o >> D$. We can write this result as

$$\delta n_g = 8.0 \times 10^{-3}(z_o/D)\delta n, \quad z_o << D \quad . \tag{78}$$

Taking $\delta n = 0.1$, $z_o = 0.3$ μm and $D = 3.0$ μm, we have $\delta n_g = 8 \times 10^{-5}$. Inserting this result into Eq. (57), we predict a dynamic range of only 14 dB. This result assumes that we are dealing with contiguous scattering centers of 10-μm size. The dynamic range increases to 24 dB for 3.2 μm scattering centers. Note that δn should be taken to describe fluctuations in the high index layer at the surface, since a uniform high index layer would produce no scattering. Since this layer is presumed to result from compounds having $\delta n \simeq 0.1$, we should really insert the variation $\delta(\delta n)$ into Eq. (57). The value $\delta(\delta n) = 0.01$ would increase the dynamic range by 20 dB to the vicinity of 40 dB, depending on scattering center size.

Nevertheless, this scattering mechanism has to be considered important. Experimentally we have verified its presence by measuring improvement in our waveguides upon polishing the surface following the diffusion process.[1]

In order to complete our study of RGD volume scattering centers, let us now consider the possibility of scattering from Ti concentration fluctuations that occur as a result of the statistical nature of the Ti-film deposition and diffusion process. These cannot be avoided regardless of care taken in waveguide preparation. A 200 Å Ti film diffused to make a 2 μm deep waveguide will have an average concentration in the material of $c = 5.7 \times 10^{20}$ cm^{-3}. If we consider a surface area of a^2, the average number of Ti atoms within that area is $\langle N \rangle = ca^2D$, where D is the diffusion depth. The standard deviation in that number is about $\langle N \rangle^{1/2} = (ca^2D)^{1/2}$. The corresponding fractional variation in the number of Ti atoms in each cell is $\langle N \rangle^{1/2}/\langle N \rangle = (ca^2D)^{-1/2}$. Accordingly, if Δn is the index change associated with the average Ti count, then $\delta n = \Delta n\,(ca^2D)^{-1/2}$ is the index change associated with statistical fluctuations in the Ti count in each scattering area a^2. This quantity is to be inserted into the expression for scattering cross section, Eq. (56).

Although it appears rather unphysical that δn depends on the arbitrarily chosen size of the scattering area, a, this dependence cancels out of the product

$\Sigma\sigma(\phi)$ upon which all measured quantities depend. This occurs because $\sigma(\phi) \propto a^4\delta n^2$ and $\Sigma = a^{-2}$ for adjacent scattering areas of size a. We find from Eq. (56)

$$\Sigma\sigma(0) = (2/\pi)\, n k_o^3 \Delta n^2/cD \ . \tag{79}$$

When this result is inserted into Eq. 28 for dynamic range, we find $P_o/\Delta P_o$ = 79.3 dB. In performing the calculation we have utilizied Q = 10, δy = 5 μm, n = 2.2, $k_o = 2\pi/0.633$ μm, Δn = .007, and D = 2 μm. The result shows that scattering from statistical fluctuations in the Ti concentration is not likely to be a factor limiting spectrum-analyzer dynamic range.

Calculations of Waveguide Attenuation. Since we have calculated the spectrum-analyzer dynamic range associated with surface roughness and volume-scattering centers in the RGD limit, it is interesting to estimate what those mechanisms imply regarding waveguide attenuation. In Eq. (40) of Ref. 1 we present expressions for the attenuation coefficient associated with surface roughness and volume scattering. (A factor δn^2 has been inadvertently omitted from the expression for volume scattering.) Moreover, these expressions are proportional to $E_o(0)^2$, the square of the waveguide field at the surface. The formula for $E_o(0)^2$ given in Eq. (24) of Ref. 1 should be replaced by Eq. 70 of this report. The result is the addition of a factor $[Vb^{1/2}/(Vb^{1/2}+1)](1-b)$ to the formulas for the attenuation coefficient. This factor shows the dependence on waveguide modal characteristics, but for cases of interest, V ≈ 3, b ≈ 0.2, the added factor is close to 1/2 in value. Incorporating this factor into the results of Ref. 1, Eq. (40), we have

$$\alpha_{surf} \simeq (2/3\pi^2) n_2^{1/2} \Delta n\, \Sigma a^2 k_o^2 \sigma^2/D(k_o a)^{1/2}$$

$$\alpha_{vol} \simeq (2/3\pi^2) n_2^{5/2} (n_1^2 - n_o^2)^{-3} \Delta n \Sigma a^2 \delta n^2/D(k_o a)^{1/2} \ . \tag{80}$$

For surface roughness, the parameters $\Sigma = 10^{-2}$ μm^{-2}, a = 10 μm, Δn = 0.007, $k_o = 2\pi/0.633$ μm, D = 2.55 μm, n_2 = 2.2, and σ = 31 Å were found to provide a 40 dB spectrum-analyzer dynamic range. When inserted into the first of Eq. (80), the same parameters provide

$$\alpha_{surf} \simeq 1.1 \times 10^{-3} \text{dB/cm} \tag{81}$$

For volume scattering centers, parameters for 40 dB dynamic range include $\Sigma = 6\ \text{mm}^{-2}$, $\delta n = 0.003$, and $a = 3\ \mu\text{m}$. If in addition $\Delta n = 0.007$, $n_2 = 2.2$, and $D = 2.55\ \mu\text{m}$, we find from the second of Eqs. (80)

$$\alpha_{vol} = 1.0 \times 10^{-10} \text{dB/cm} \tag{82}$$

The tremendous reduction relative to the attenuation from surface roughness comes primarily from a 10^3 reduction in Σ and a 10^3 reduction in the value of δn^2 relative to the value of $(k_o \sigma)^2$. The result emphasizes a conclusion reported in Ref. 1: that volume scattering centers are efficient generators of in-plane scattered energy, while surface roughness scattering centers are efficient generators of out-of-plane scattered energy. However neither mechanism produces much scattering of either type if the calculations of this section can be relied on. Reported levels of attenuation in $LiNbO_3$ waveguides[26] may well reflect intrinsic absorption losses and scattering from other sources than the RGD scatters considered here.

Differential Scattering Cross Sections in the Mie Limit

In Section II we described several types of scattering centers that do not appear to be well described by Rayleigh scattering, because of their potentially large size, or by Rayleigh-Gans-Debye scattering, because of their large refractive index difference from their environment. We will use a simple but attractive analysis to predict the scattering cross section for these Mie scattering centers. We assume them to be large in comparison to a wavelength, so that a beam of light passing through them is subject to Snell's law of refraction. If the typical radius of curvature seen by an incident waveguided beam is a, an approximate application of the lens-makers formula[27] suggests that the output beam will focus at a distance

$$R \simeq a/2\delta n \tag{83}$$

At distances much greater than R, the half-angle of divergence of the beam is given by

$$\theta_{div} = \tan^{-1} a/R \simeq \tan^{-1} 2\delta n \quad . \tag{84}$$

In the waveguide geometry, most of the light emitted into the upper part of the light cone is reflected from the waveguide surface into the substrate, doubling the intensity in that region. At a distance $r \gg R, a$ from the scattering center, the area subtended by the light cone in the substrate is a semicircle of radius $r \tan \theta_{div} \simeq 2r\delta n$. The area of the semicircle is $A = 2\pi r^2 \delta n^2$. If the power scattered by the inhomogeneity is equal to the power intercepted,

$$\Delta P_{tot} \simeq 2 I_o a \quad , \tag{85}$$

the power per unit area in the scattered beam is

$$\Delta P_{tot}/A = I_o a/\pi r^2 \delta n^2 \quad . \tag{86}$$

The effective area covered by a waveguide detector at a distance r is $A_d = r^2 \Delta\Omega$ where $\Delta\Omega$ is the solid angle subtended by the detector, given in terms of the waveguide acceptance angle by Eq. (35). We find

$$A_d = 2r^2 (2\Delta n/n)^{1/2} \Delta\phi \tag{87}$$

where $\Delta\phi$ is the angle subtended by the detector in the plane of the waveguide.

The power intercepted by the detector is

$$\Delta P = \Delta P_{tot} A_d/A = (1/\pi)(2\Delta n/n)^{1/2} (I_o a f/\delta n^2) \Delta\phi \quad . \tag{88}$$

As before, a factor f is introduced to account for the fact that not all rays scattered within the acceptance angle will be trapped in waveguide modes: f is the fraction trapped. The differential scattering cross section is

$$\sigma(\phi) = \Delta P/I_o \Delta\phi = (1/\pi)(2\Delta n/n)^{1/2} a f/\delta n^2 \quad . \tag{89}$$

Actually light is scattered only in the range $-\theta_{div} \leq \phi \leq +\theta_{div}$ bounded by the light cone. Outside this range $\sigma(\phi) = 0$. For $\delta n = 0.1$ the range is $2\theta_{div} = 22.6°$. This is intermediate between Rayleigh scattering and Rayleigh-Gans-Debye scattering. However, the angle is large enough relative to the scattering angles important in the spectrum-analyzer application that the problem may be treated

as we treated Rayleigh scattering; that is, the dynamic-range equation is

$$P_o/\Delta P = [Q\Sigma\sigma(0)\delta y]^{-1} \quad , \tag{90}$$

where the geometric factor $Q \approx 100$ as for Rayleigh scattering. Also taking $\delta y = 5$ μm, and inserting Eq. (89) into Eq. (90), we find

$$P_o/\Delta P = [(500\ \mu m)(1/\pi)(2\Delta n/n)^{1/2}\Sigma\alpha f/\delta n^2]^{-1} \quad . \tag{91}$$

This formula may be expressed in terms of the waveguide attenuation coefficient. If we ignore the power trapped in waveguide modes in comparison to the total power scattered, the power lost to the waveguide over a path length L is

$$\Delta P_{lost} = 2I_o\alpha\Sigma LW \quad . \tag{92}$$

The attenuation coefficient is

$$\alpha = \Delta P_{lost}/(I_o W)L = 2\Sigma\alpha \quad . \tag{93}$$

Substitution of this result into Eq. (91) yields

$$P_o/\Delta P = [1.46 \times 10^{-4}\alpha f/\delta n^2]^{-1} \quad , \tag{94}$$

where we have used $\Delta n = 0.007$ and $n = 2.2$ to obtain the numerical coefficient, and where α is given in dB/cm.

The largest values of δn that we might be expected to encounter experimentally are $\delta n = 2.2-1.0 = 1.2$, for pits in the waveguide surface or subsurface voids, and $\delta n \approx 0.15$ for the separated phase $LiNb_3O_8$.[1] Li-Ti-O compounds formed during the diffusion process are also likely to have $\delta n \geq 0.1$. Smaller values of δn are treated using RGD theory.

Taking $\alpha = 0.1$ dB/cm, $f = 1/2$ and $\delta n = 0.12$ in Eq. (94) we find $P_o/\Delta P_o = 33$ dB. This is among the smaller dynamic ranges we have calculated yet. The condition $\alpha = 0.1$ dB/cm could result from scattering centers as small as 1 μm and densities as low as 1 mm^{-2}. Such small, dispersed scattering centers might be difficult to locate despite their large index changes. Thus it is well to consider them as relevant to the spectrum-analyzer dynamic range problem.

CALCULATIONS OF SCATTERING AT 90°

Thus far we have emphasized forward scattering because it is this component that will limit spectrum-analyzer dynamic range. However, forward scattering is difficult to study experimentally because of the presence of the unscattered beam and of scattered light from optical components of the beamforming system. The observation of scattering at 90° is useful as a means of circumventing these complexities. However, it must be remembered that of all the types of scattering we have discussed only Rayleigh scattering of TM modes will have a large differential cross section for $\phi = 90°$.

Let us consider the experiment shown in Fig. 18 in which in-plane scattered light at ϕ=90° is coupled out of the waveguide and viewed by a dark-adapted eye. The power into the eye is

$$\Delta P = P\Sigma L\sigma(\pi/2)\eta\Delta\phi \quad , \tag{95}$$

where P is the power in the waveguide, L is the length of the beam path contributing to the observation, $\Delta\phi$ is the angle subtended by the dilated pupils of the observers eyes, and η is the output coupling efficiency of the prism located between the scattering area and the observer.

We will take $\Delta P \simeq 10^{-15}$ W to be the threshold of vision. This number is based on physiological studies and its derivation is presented in Appendix A. Then we can substitute appropriate values for P, L, η, and $\Delta\phi$ and determine the smallest value of $\Sigma\sigma(\pi/2)$ that will produce a visual effect. The experimental parameters are $P = 2 \times 10^{-4}$ W, L = 1 cm, $\eta \simeq 0.1$ and

$$\Delta\phi = d/Dn = 7.6 \times 10^{-3} \quad , \tag{96}$$

where d = 5mm is the pupil aperture, D = 30 cm is the approximate viewing distance, and n = 2.2 is the refractive correction necessary to account for the Snell's-law-associated increase in the scattering angle upon leaving the waveguide and entering free space. These values indicate

$$\Sigma\sigma(\pi/2) \geq 6.6 \times 10^{-13} \ \mu m^{-1} \tag{97}$$

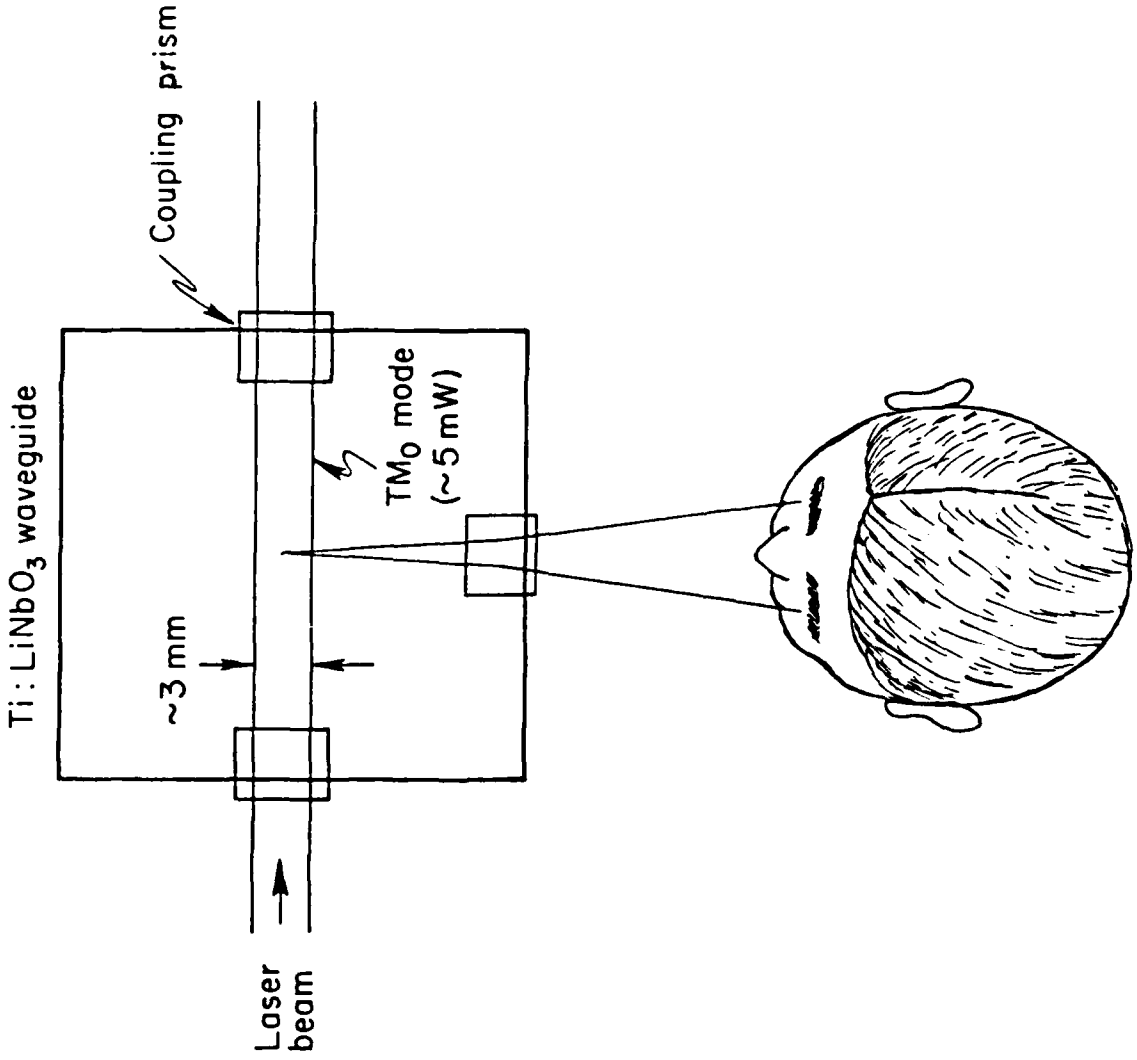

Fig. 18. Observation of scattered light at 90°.

for a visual effect.

For Rayleigh scattering of TM waveguide modes, $\Sigma\sigma(\pi/2) = \Sigma\sigma_{tot}(3/8\pi)$, where σ_{tot} is the total scattering cross section and $\Sigma\sigma_{tot}$ is the attenuation coefficient, α. We thus find

$$\alpha \geq 2.4 \times 10^{-7} \text{ dB/cm} = 0.024 \text{ dB/km} \tag{98}$$

in order for scattering from dipole sources to be observed at 90°. This is two orders of magnitude better than the current attenuation levels found in the best optical fibers.

The reader may have already anticipated that in the experiment we performed, no light was detected. Even if our crude calculations are in error by two orders of magnitude, the result suggests that a negligible level of dipole scattering is to be found in $LiNbO_3$ waveguides. If the attenuation coefficient of Eq. (98) is inserted into Eq. (39), for example, we predict a spectrum analyzer dynamic range in excess of 110 dB.

Let us now consider RGD and Mie scattering centers, which are large in comparison to wavelength. Our derivations of scattering cross sections for these types of scattering centers have made use of their refractive properties. This has led to the result that scattering is concentrated in the forward or near forward direction, with $\sigma(\pi/2) \approx 0$. Let us now consider the scattering contribution caused by reflection from these scattering centers. We take the total scattered power as equal to the intercepted power times an average reflection coefficient. The later quantity depends on the interior index of the scattering center, on its shape and on the optical polarization. For normal incidence the reflection coefficient is $[\delta n/(2n + \delta n)]^2$ and for grazing incidence it approaches unity. We will take δn^2 as an average value. We further assume that the reflected power is distributed uniformly over a solid angle of 4π. The solid angle encompassed by the detector is $\Delta\theta\Delta\phi$, where $\Delta\theta = 2(2\Delta n/n)^{1/2}$ is the acceptance angle of the waveguide. If a fraction f of light reflected within the acceptance angle of the waveguide is trapped in waveguide modes, the detected power is

$$\Delta P = (2I_o a\delta n^2)(1/4\pi)2(2\Delta n/n)^{1/2}\Delta\phi f \quad . \tag{99}$$

The differential scattering cross section for light scattered in plane at an angle $\phi \cong 90°$ is

$$\sigma(\phi) = (\Delta P/I_o \Delta\phi) = a\delta n^2 f(2\Delta n/n)^{1/2}/\pi \quad . \tag{100}$$

Inserting this result in Eq. (97), first taking f = 1/2, $\Delta n = 0.007$, and n = 2.2, we find that

$$\Sigma a\delta n^2 \geq 0.52 \times 10^{-10}\ \mu m^{-1} \quad . \tag{101}$$

must be satisfied to produce visible Mie scattering at 90°.

For the case of weak RGD scatterers confined near the waveguide surface we assume that most of the reflected radiation remains trapped in the waveguide mode. This results in an expression for scattering cross section similar to that of Eq. (100), except that the product $f(2\Delta n/n)^{1/2}$ does not appear. The corresponding inequality

$$\Sigma a\ \delta n_g^2 \geq 0.2 \times 10^{-11}\ \mu m^{-1} \tag{102}$$

must then be satisfied to produce a visible scattering effect at 90°.

Consider first a dense system of RGD scattering centers, such as surface roughness, described by $\Sigma = a^{-2}$, a = 10 μm and $\sigma = 30$ Å. This is found to produce a dynamic range of 40 dB and a value $n_g = 3.7 \times 10^{-6}$. We find $\Sigma a\delta n_g^2 = 0.14 \times 10^{-11}\ \mu m^{-1}$. Considering the limitations of the calculation the observation of visible scattering at 90° is marginally possible. For the case of $LiNb_3O_8$ or Li-Ti-O compounds near the waveguide surface, the parameters $\Sigma = a^{-2}$, a = 10 μm, $(z_o/D) = 0.1$, and $\delta(\delta n) = 0.01$ produce 34 dB dynamic range and $\Sigma a\delta n_g^2 = 0.6 \times 10^{-11}\ \mu m^{-1}$. A visible scattering effect is again marginally indicated.

Next consider scattering that might result from gaps in the waveguide caused by dust trapped beneath the Ti film prior to diffusion. We found that a = 3.2 μm, $\Sigma = 15\ mm^{-2}$, and $\delta n_g = 10^{-3}$ produced a spectrum-analyzer dynamic range of 40 dB. The same parameters are associated with the product $\Sigma a\delta n_g^2 = 4.8 \times 10^{-11}\ \mu m^{-1}$. Again, a visible scattering effect at 90° is marginally indicated.

Next consider the scattering situation where $a = 10\ \mu m$ and $\delta n \simeq 0.1$, such as might be associated with separated $LiNbO_3$ phases or lithium titanate compounds. The scattering centers are not assumed to be confined near the waveguide surface. A density of $\Sigma = 0.1\ mm^2$ is found to lead to a spectrum analyzer dynamic range of about 34 dB. For the same parameters we find

$$\Sigma a \delta n^2 = 10^{-8}\ \mu m^{-1} \quad . \tag{103}$$

This is 200 times greater than the value from Eq. (101) required for a visible scattering effect at 90°. If Σa is reduced accordingly to provide consistency with our null scattering observation at 90°, the spectrum-analyzer dynamic range is predicted to increase to 47 dB. However, we are now dealing with scattering center densities so low that individual scatterers can be avoided in experiments by careful selection of optical beam paths. This is not found to be the case in practice. We conclude that our null observation of scattering at 90° is an argument against the existence of Mie scattering by islands associated with $LiNb_3O_8$ and Li-Ti-O compounds.

Finally, consider scattering at 90° by large polishing imperfections, such as pits in the surface as subsurface voids, both having $\delta n \simeq 1$. If $a = 1$ and $\Sigma = 1\ mm^{-2}$, corresponding to $\alpha = 0.086$ dB/cm and a spectrum-analyzer dynamic range of 45 dB, we have

$$\Sigma a \delta n^2 = 10^{-6}\ \mu m^{-1} \quad . \tag{104}$$

This is 20,000 times the value required for a visible scattering effect at 90°. This is a strong indication that this type of scattering is not important in practice. We conclude that our null scattering observation is most consistent with RGD scattering from surface roughness, surface compounds, and gaps in the waveguide Ti distribution. Rayleigh and Mie scattering mechanisms are least consistent with our observation.

SUMMARY

In this section we derived equations for spectrum-analyzer dynamic range in terms of spectrum-analyzer design, scattering-center density, and scattering-center cross section. Then we considered various models for

scattering centers and calculated cross sections based on those models. This has enabled us to predict which scattering mechanisms are likely to be of greatest significance in limiting spectrum-analyzer dynamic range. Our results are dispersed throughout the section, so it is appropriate to summarize them here. This is done in Table I.

Only the entries in the last column of Table I may require explanation. These are ratios of calculated power scattered at 90° to the estimated minimum detectable power for a human observer, 10^{-15} W. Values of this ratio greater than unity indicate that the scattered light should be sufficiently intense to produce a visual effect. Values less than unity are consistent with our opposite experimental result. However, the calculation is so approximate and the experiment so qualitative that we suggest that ratios as large as several hundred may be compatible with our observation.

On this basis, all scattering mechanisms listed in Table I are candidate mechanisms except for Rayleigh scattering from defects smaller than a wavelength and Mie scattering from surface or subsurface polishing imperfections. Mie scattering from islands of $LiNb_3O_8$ and Li-Ti-O compounds that are large or comparable to waveguide thickness are possible limiters of dynamic range to values less than 40 dB; however, the size and index of these islands would make it likely that they could be seen with a microscope. Since we have not done so, we discount their importance.

This leaves Rayleigh-Gans-Debye (RGD) scattering. Reasonable values of surface roughness show a rather high dynamic range associated with this source of RGD scattering. Comparable or higher dynamic range is associated with Ti voids in the waveguide layer and statistical fluctuations in the Ti concentration. The only remaining candidate for significant levels of RGD scattering is the formation of $LiNb_3O_3$ and Li-Ti-O scattering centers near the waveguide surface. In fact, this source of scattering is verified experimentally. Burns et al report evidence for the formation of Li-Ti-O compounds during waveguide fabrication.[7] They also report results indicating the possible confinement of these compounds near the top 0.3 μm of the waveguide layer. The etch-resistance that we have found in diffused layers may be a further indication of the presence of these compounds. Additionally we have found reduction of scattering when the waveguide is polished following diffusion.[1]

TABLE I. SCATTERING CENTER PARAMETERS

Scattering Class / Mechanism	Size a(μm)	Density $\Sigma(mm^{-2})$	Index δn	Roughness σ(Å)	Depth z_o(μm)	Effective index δn_g	Dynamic Range (dB)	Attenuation dB/cm	$\Delta P(90°) \div \Delta P_{threshold}$
Rayleigh									
Dipole	0.1	400	1.0	-	-	-	40	1	4×10^6
	0.1	4000	0.1	-	-	-	50	0.1	4×10^5
	0.01	96	1.0	-	-	-	106	2.4×10^{-7}	1
Rayleigh-Gans-Debye									
Surface roughness	10	10^4	-	31	-	3.8×10^{-6}	40	1.1×10^{-3}	0.7
	10	10^4	-	10	-	3.8×10^{-7}	50	1.1×10^{-4}	0.7×10^{-2}
Ti voids	1	15	0.007	-	-	0.003	50	6.4×10^{-11}	67.5
	3	2	0.007	-	-	0.003	40	7.6×10^{-11}	27.0
$LiNb_3O_8$, Li-Ti-O	10	10^4	0.1	-	0.1	8×10^{-5}	14	0.12	320
Surface compounds	1	10^6	0.1	-	0.1	8×10^{-5}	34	0.12	3.2×10^3
	10	10^4	0.01	-	0.1	8×10^{-6}	34	1.2×10^{-3}	3.2
Ti concentration	10	10^4	1.8×10^{-8}	-	-	1.8×10^{-8}	79	2.8×10^{-17}	1.6×10^{-5}
statistical fluctuations	1	10^6	1.8×10^{-7}	-	-	1.8×10^{-7}	79	2.8×10^{-15}	1.6×10^{-2}
Mie									
$LiNb_3O_8$, Li-Ti-O	10	1	0.1	-	-	0.1	22	0.86	2×10^3
compounds	1	1	0.1	-	-	0.1	32	0.086	200
Polishing Imperfections	1	1	1.0	-	-	1.0	52	0.086	2×10^4

The results of this section are consistent with the experimental findings, and suggest that once this source of scattering is eliminated, no other of the potential sources considered are likely to limit spectrum analyzer dynamic range to values less than about 40 dB.

V. MEASUREMENT AND EVALUATION OF WAVEGUIDE PERFORMANCE

THE IN-PLANE-SCATTERING EXPERIMENTAL METHOD

The measurement of in-plane scattered energy distributions was performed in this program much as in the preceding program and described in Ref. 1. The experimental setup is shown in Fig. 19. A Gaussian beam of approximately 1-mm waist is prism coupled into and out of the waveguide and focused with a lens of about 10-cm focal length on a slit of variable width s. Typically s is in the range 20-60 μm. When the slit is displaced from the optical axis by a distance x, it collects light scattered in the waveguide at an angle $\phi = x/n_g f$, where n_g is the mode index.

The scattered power through the slit is typically 20-40 dB down from the peak power. Moreover, the peak power must be kept small to avoid the generation of optical damage by the photorefractive effect.[29] As a result, we have the problem of detection of low light levels. For this reason we use a photomultiplier tube to monitor the light passed by the slit. In addition, light coupled into the waveguide is amplitude modulated by periodically varying the angle of incidence of the input beam, using an oscillating mirror. The modulated component of the photomultiplier tube output is measured using a lock-in amplifier. The log of the output from the lock-in amplifier is generated by a log amplifier and delivered to the y-axis of an x-y recorder. The x-axis displacement is proportional to the separation x of the slit from the optical axis of the beam. When the x and y axes are properly calibrated we obtain a plot of $\log_{10}(\Delta P(\phi)/P)$ versus ϕ, where $\Delta P(\phi)$ is the power through the slit from rays scattered at an angle ϕ in the waveguide and P is the peak power through the slit from the unscattered beam.

Dynamic Range

Owing primarily to the need to keep the peak power in the waveguide low, the dynamic range of our measurement was limited to 50 dB. That is, the electronic noise level was about 53 dB below the signal generated when the maximum power was passed through the slit. The dynamic range could be

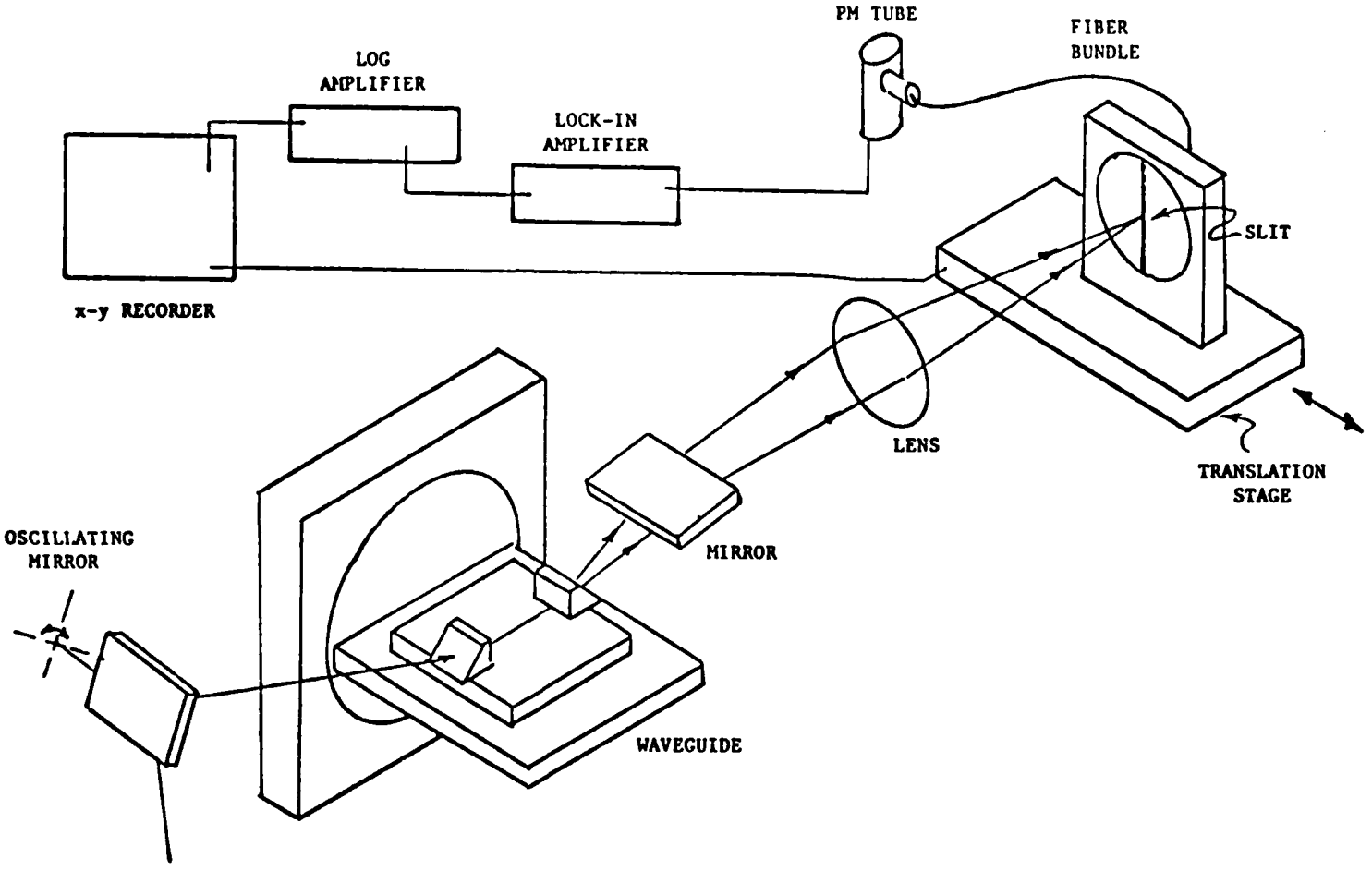

Fig. 19. The in-plane scattering experimental method.

increased by a number of techniques: cooling the photomultiplier or replacing it with a lower-noise tube, increasing the lock-in time constant, increasing the slit width at low power levels, working at optical wavelengths or at elevated temperatures where optical damage is not a problem and higher beam powers may be used. We actually investigated the simplest of these methods, increasing the time constant and varying the slit width. However, both methods entail a certain amount of inconvenience. A longer time constant requires a longer data-acquisition time. Varying the slit width requires a more complicated data analysis. In fact, spectrum-analyzer performance is specified by the on-axis scattering and the angular range of scattering. Since both of these are measurable when the dynamic range is 50 dB, we made no unusual attempts to increase system dynamic range further. Ultimately this should be done in order to measure the scattering at angles beyond a few degrees from the optical beam axis.

Sources of Spurious Scattering

A perhaps more serious experimental problem than limited dynamic range is the optical noise generated by light scattering at components other than the waveguide under test. Each intersection of the beam with a surface is a potential source of scattering. This includes, in Fig.19, the Fourier-transform lens, the mirrors used to direct the beam, and the coupling prisms. It also includes items left out of Fig.19 for simplicity, such as the laser and all beam-forming and polarizing optics.

Scattering from items located well in advance of the waveguide can be reduced by placing an aperture slightly larger than the beam diameter in front of the oscillating mirror in Fig.19. Scattering from mirrors and the lens close to the waveguide can at least be measured to demonstrate that it doesn't contribute much to the total scattering level. However, we still have scattering from the input and output coupling prisms which cannot readily be separated from scattering in the waveguide.

Prism Enhanced Scattering

Our best attempt at doing this has been to measure the total scattering from the waveguide-prism system with the prisms about 1-2 mm apart, and then with the prisms about 15 mm apart. If prism scattering is negligible, the total scattering should increase in proportion to waveguide path length. Accordingly, a 10 dB variation is anticipated. In fact, the variation is in the range 0-3 dB, leading to the conclusion that scattering at the prism interfaces is an important part of the total scattering observed.

Subsequent to the acquisition of data for this program, we undertook a theoretical study of scattering associated with prism coupling. The results of this study are contained in Appendix C. We found that even a perfect prism can serve to enhance the amount of scattering from waveguide scattering centers beneath the prism. The source of the enhanced scattering is the evanescent field associated with light from the input beam that strikes the base of the coupling prism and is totally reflected. This evanescent prism field can be more intense than the waveguide field, causing the level of scattering from the prism-coupling region to rival scattering from the free waveguide despite the much longer path length of the free waveguide.

If this path length is designated as L_g, the effect of prism-enhanced scattering may be characterized by a parameter R such that

$$L = L_g + RL_g \tag{105}$$

is the effective path length over which scattering may be said to occur. If L_c is the prism coupling length and there is no prism enhancement of scattering, we expect

$$R = R_{min} = L_c/L_g \tag{106}$$

Ordinarily $R_{min} \approx 1/10$. However, the results of Appendix C show that $R \sim 1$ is possible, while our experimental results, to be described, suggest that $R \geq 1$.

In any case the best approach to data obtained using input-and output-prism coupling is to subtract the scattered signal obtained when the free path length has two different values, say L_g and L_g'. The difference

signal then represents scattering from the path length $L_g - L'_g$. Assuming that R remains the same in the two measurements, the effects of prism enhanced scattering are subtracted away.

Polished Edges for End Fire Coupling

There must be some concern as to whether the above cited procedure works well, in view of the possibility that R varies with each new placement of the prism on the waveguide. This concern is justified by occasional experimental results that show greater scattering when the prism separation is reduced.

To avoid this source of experimental error, we thoroughly investigated the possibility of replacing prism coupling with end-fire coupling through polished waveguide edges. The procedures used to generate polished edges were as follows.

Two $LiNbO_3$ slabs obtained from Crystal Technology were clamped tightly together between two steel 25.4-mm cubes that were ground to an angular precision of + 30" (angle between faces = 90° + 30"). The $LiNbO_3$ slabs were 25mm x 25mm x 3mm, with both 25mm x 25mm faces polished to a flatness of $\lambda/10$. The samples were cleaned to permit intimate contact when clamped between the stainless steel blocks.

The entire assembly was ground using 15-μm alumina abrasive on a glass lap until the faces to be polished were flush. At this stage the 25mm x 3mm $LiNbO_3$ faces have a lightly frosted appearance. Polishing is accomplished through the subsequent use of increasingly smaller abrasives, including 3 μm diamond, 1 μm diamond on solder laps, and finally colloidal silica in the form of Syton HT-30. All operations are performed in an automated fashion using a Logitech PM2 polishing machine. For the final polish with Syton, the solder lap is replaced by an expanded polyurethane lap.

In nearly all samples fabricated in this manner, there exist millimeter-length regions along the polished edge which appear to be defect-free under SEM examination. Moreover, curvature of the edge is not apparent even under 10,000X magnification, indicating that the radius of curvature of the edge is well under 0.1 μm. These characteristics bode well for the

replacement of prism input coupling with end-fire coupling. However, certain problems are inherent in the technique.

One serious problem results from the intimate contact achieved between the two $LiNbO_3$ slabs butted together for polishing. When polishing is completed, the two slabs are held together by strong attractive forces and cannot be separated without introducing at least a small degree of translational motion of one sample across the face of the other. This usually results in some damage to the two faces in contact, which are those on which the waveguide is to be fabricated. The damage often appears to be caused by an abrasive particle or a $LiNbO_3$ chip that is introduced to the interface region during the grinding operation.

This problem is of tolerable severity when only one polished edge is required per waveguide. One can usually select sample areas of good surface quality for study. The problems associated with end-fire coupling are componded, however, when one tries to obtain two polished edges for both input and output end-fire coupling. We expended significant energy in this direction owing to our desire to mimic the spectrum-analyzer configuration as closely as possible.

A second polished edge per sample requires greater effort than the first polished edge. Ideally, the assembly consisting of steel cubes contacting $LiNbO_3$ slabs should simply be inverted in order to polish the opposite 3mm x 25mm crystal faces using the identical procedure outlined above. In practice adjacent $LiNbO_3$ slabs will not be in intimate contact over their entire area owing to a slight bow in one or both crystals. The resulting polished edge is rounded to an unsatisfactory degree and the crystals have to be remounted for successful polishing to occur. Additionally, the bow affords an entry way for particulate matter that can damage the surface when the crystals are separated prior to remounting, and then after remounting and polishing of the second edge.

We attempted to surmount these problems by using a nonabrasive cement between the two adjacent $LiNbO_3$ surfaces. This would serve to protect the surfaces. At the same time, it was hoped that the cement would be sufficiently thin and close to $LiNbO_3$ in hardness that little edge rounding would occur.

The cements that we employed were Lakeside cement and dental resin. The former polished away too rapidly, causing severe edge rounding. The dental resin produced a satisfactory edge sharpness except in those locations where a bubble had formed during setting. In these regions, chipping or distortion of the polished edge took place. Possibly handling procedures could be developed for producing highly uniform layers of dental resin, but we did not pursue the matter further.

To those who may wish to develop and later experiment with end-fire input and output coupling, we note two additional problems with polished edges that can occur. Each edge may have regions of good quality extending for several millimeters; however, these regions may not both be in line with a beam travelling in the preferred direction. In that case, one may have to bear with scattering from one of the two edges. A further problem with end-fire coupling is the separation of substrate light from waveguide light. Prisms accomplish this quite nicely, a fact that helps to compensate for the disadvantage of prism-enhanced scattering.

In our opinion, the optimum experimental configuration for studying in-plane scattering makes use of end-fire input coupling and prism output coupling. A single polished edge can be generated without too much difficulty or damage to the waveguide surface. This allows one to avoid prism-enhanced scattering by use of end-fire input coupling. The use of a prism output coupler permits good discrimination between waveguide and substrate modes. While prism enhanced scattering does occur during output coupling owing to the evanescent field of the output coupled beam, the enhancement from this source of scattering is low enough to be ignored. Much of our discussion of experimental data will refer to an in-plane scattered energy distribution that was obtained using end-fire-input and prism-output coupling.

METHODS FOR ANALYSIS OF EXPERIMENTAL RESULTS

Development of the Basic Formulas

In Sec. IV we derived expressions for the scattered power detected by diode-array elements in a spectrum analyzer. These expressions

do not relate directly to the experiment shown in Fig. 19 because of significant variations from the geometry of that experiment to the spectrum analyzer geometry shown in Fig. 13. Therefore it is necessary to derive new expressions which will enable us to relate the detected signal in our in-plane scattering experiments to the waveguide-scattering parameters discussed in Sec. IV.

The starting point is the equation

$$\Delta P = \Sigma W L I_o \sigma(\phi)\, \Delta\phi \quad , \tag{107}$$

where ΔP is the power scattered in-plane at angle ϕ to the optical path, and within an angular sector $\Delta\phi$, measured in the waveguide material. Σ is the density of scattering centers, I_o is the power per unit beam width, W is the beam width, $\sigma(\phi)$ is the differential scattering cross section, and L is the effective path length in the waveguide, which may include the contribution from prism enhancement, if appropriate, as described by Eq. 105. When this power is coupled out of the waveguide, ϕ and $\Delta\phi$ change as required by the Snell's law of refraction. For the small angles of interest, we have

$$\phi_{ext} = n_g \phi \quad , \tag{108}$$

$$(\Delta\phi)_{ext} = n_g (\Delta\phi) \quad ,$$

measured external to the waveguide, where n_g is the mode index. In the focal plane of the Fourier transform lens in Fig. 19, the light energy scattered at ϕ in the waveguide appears at a distance

$$x = f\phi_{ext} = f n_g \phi \tag{109}$$

from the optical axis. It spans an interval

$$\Delta x = f(\Delta\phi)_{ext} = f n_g \Delta\phi \tag{110}$$

where f is the lens focal length. A slit of width s in the focal plane therefore collects light scattered over an angular range

$$\Delta\phi = s/n_g f \tag{111}$$

in the waveguide. Inserting this result into Eq. (107), we obtain

$$\Delta P = \Sigma W L I_o \sigma(\phi) s/n_g f \tag{112}$$

as the detected power at the slit location $x = f n_g \phi$.

This equation is not valid on-axis, where the slit collects light from the unscattered incident beam. Let us consider a beam having a peak power per unit width of I_o and a total power of I_oW. If the intensity profile of the beam is uniform, W is the actual beam width. If the profile is Gaussian, $W = W_1(\pi/8)^{1/2}$, where W_1 is the diameter of the beam measured between the points at which the intensity is I_oe^{-2}. If the slit width is small in comparison to $f\lambda_o/W$, the power passed by the slit is

$$\Delta P(0) = P = qI_o(W^2/f\lambda_o)s \quad , \tag{113}$$

where $q = 1$ for a uniform beam and $q = 2$ for a Gaussian beam. If the slit width is larger than $f\lambda_o/W$, the power passed by the slit is the total power I_oW. Through the use of the log amplifier shown in Fig. 19, the quantity measured in the experiment and plotted on the x-y recorder is the negative of the dynamic range

$$-\text{D.R.} = 10 \log_{10}[\Delta P(\phi)/P] \quad . \tag{114}$$

For a small slit width, we obtain

$$\Delta P(\phi)/P = \Sigma(L/W)\sigma(\phi)\lambda_o/qn_g \quad . \tag{115}$$

This is the smallest value of $\Delta P/P$ that is consistent with a given value of $\Sigma\sigma(\phi)$. As the slit width increases, $\Delta P(\phi)$ increases linearly with s, while P saturates above $s = f\lambda_o/W$. When this happens,

$$\Delta P(\phi)/P = \Sigma L\sigma(\phi)(s/n_g f) \quad . \tag{116}$$

Since in our experiments $s \simeq f\lambda_o/W$, it appears more appropriate to use this result than Eq. 115. The answer is the same, however if Eq. 115 is used with $q = 1$, as for a uniform beam:

$$\Delta P(\phi)/P = \Sigma(L/W)\sigma(\phi)(\lambda_o/n_g) \tag{117}$$

Taking W = 1 mm, L = 15 mm, $n_g = 2.2$ and $\lambda_o = 0.633$ μm, we obtain

$$\Delta P(\phi)/P = 4.32 \text{ μm } \Sigma\sigma(\phi) \tag{118}$$

Recall that the spectrum-analyzer dynamic range was described by a formula

$$\Delta P(\phi)/P = [Q\delta y\Sigma\sigma(\phi)]^{-1} \tag{119}$$

where $10 \lesssim Q \lesssim 100$ depending on the spectrum-analyzer geometry and scattering angular range, and $\delta y \simeq 5$ μm was the detector aperture. This indicates that the spectrum-analyzer dynamic range will be between 10.6 and 20.6 dB lower (worse) than the dynamic range measured using the system of Fig. 19. If we were to evaluate a waveguide sufficient to produce a spectrum analyzer dynamic range of 40 dB, we would want the measurement system of Fig. 19 to possess a dynamic range of about 60 dB. Moreover, scattering from the various optical components that intersect the beam should have their scattered intensity reduced at least 70 dB in order not to rival the scattering from the waveguide. The best, and perhaps only way to achieve this is to eliminate all optical components on the detector side of the waveguide, and to carefully spatially filter the light incident on the waveguide to remove as much of the scattered component as possible.

We did not do this during the program because the scattering from the waveguide-prism combination was in the range 20-30 dB, and was much greater than the background scattering from components. Since the observed scattering falls off by 10 dB within 1° of the optical axis, it appears to be Rayleigh Gans Debye scattering from scattering centers of about 10 μm diameter. Thus $Q \simeq 10$ is appropriate in Eq. 119, and a 30 dB dynamic range in the experiment of Fig. 19 translates into a 20 dB dynamic range for the spectrum analyzer. This is 20 dB lower than desired and compatible with the results of Table I of Sec. IV only for the case of scattering by $LiNb_3O_8$, Li-Ti-O compound formation near the waveguide surface.

Mechanics of Data Analysis

Theoretical Fitting of the Data

The result of performing the in-plane scattering experiment shown in Fig. 19 is a recorder tracing of $10 \log_{10}[\Delta P(\phi)/P]$ versus ϕ. Figure 20 shows the experimental result that will be the basis for much of our later discussion. It is desired to analyze data of this form to obtain information about scattering parameters of the waveguide. According to Eq. 117,

$$\Delta P(\phi)/P = [\Sigma\sigma(\phi)](L/W)(\lambda_o/n_g) \qquad (120)$$

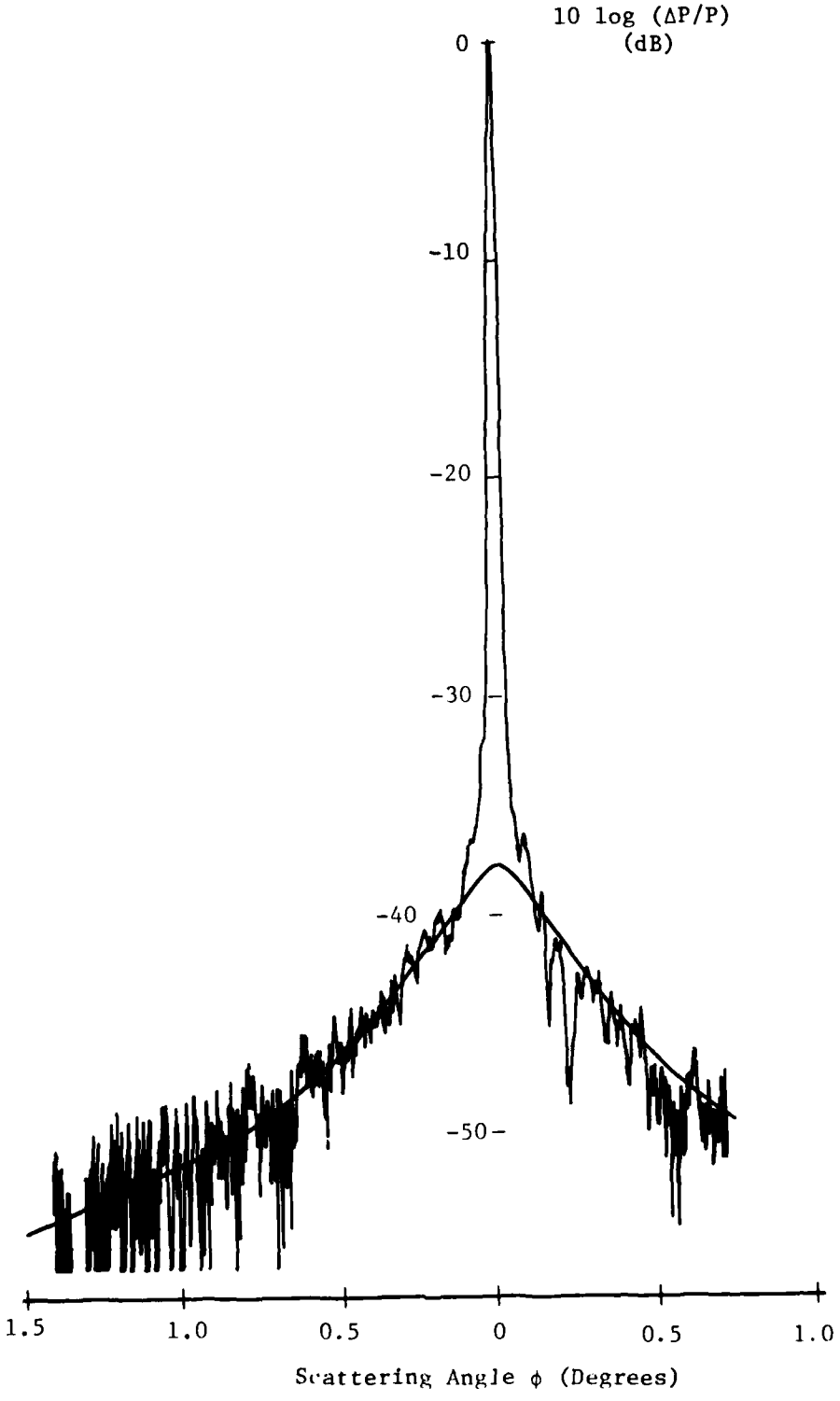

Fig. 20. In plane scattered energy distribution for sample 154 (TM_0 mode, $k \perp c$ obtained using end-fire input coupling. Scattering angles are those which would be measured in the waveguide material.

Known parameters are W, λ_o, and n_g. L may or may not be known accurately. If prism input coupling is used,

$$L = L_g + L_e \tag{121}$$

where L_g is the known separation between coupling prisms and L_e is the path length associated with prism enhancement, which may be comparable to L_g.

The result of Fig. 20 was obtained using end-fire input coupling, so that $L_e = 0$ and Eq. 14 applies with the product $\Sigma\sigma(\phi)$ being the only unknown quantity. The rapid fall-off of the scattered intensity with increasing ϕ suggests that the observed scattering is of the Rayleigh-Gans-Debye type discussed in Sec. IV. The formula for the differential scattering cross section given in Eq. 56 is

$$\sigma(\phi) = (2/\pi)nk_o^3a^4\delta n_g^2[1+(k_o na\phi)^2]^{-1}[1+R(\phi)] \tag{122}$$

In this expression $R(\phi)$ is a random function that is to be associated with the fluctuations in scattered intensity that are observed in Fig. 20. The average curve drawn through the data is that corresponding to $\langle R(\phi)\rangle = 0$, and therefore has a Lorentzian fall-off with ϕ. By inserting the average value of $\sigma(\phi)$ into Eq. 120, we obtain

$$\Delta P(\phi)/P = 4(L/W)k_o^2\Sigma a^4\delta n_g^2[1+(k_o na\phi)^2]^{-1} \tag{123}$$

The theoretical curve in Fig. 20 is consistent with the parameter values L = 15 mm, W = 1 mm, $k_o = 2\pi/0.633$ μm, n = 2.2, a = 11.7 μm and $\Sigma a^2\delta n_g^2 = 2.25 \times 10^{-10}$. The on-axis dynamic range of 37.4 dB of the theoretical curve suggests that the dynamic range of a spectrum analyzer fabricated using this waveguide would be 37.4 - 10.6 = 26.8 dB. This is in accord with Eqs. 118, 119 and the discussion following those equations.

These conclusions are based on the fitting of a Lorentzian curve to the data. We have generally done this in the following manner. The quantity $\Delta P/P$ is measured at 2N different scattering angles

$$\phi_m = \pm m\Delta\phi, \qquad m = 1,2,\ldots N \quad . \tag{124}$$

From Eq. 123 the quantity $P/\Delta P$ is a linear function of ϕ^2, having slope = $(k_o na)^2/[4(L/W)k_o^2\Sigma a^4\delta n_g^2]$ and intercept = $[4(L/W)k_o^2\Sigma a^4\delta n_g^2]^{-1}$. The fit to the

experimental curve is obtained by plotting the 2N data points $P/\Delta P(\phi_m)$ vs ϕ_m and determining the best straight line using the method of least-squares deviation.

Typically $\Delta\phi \approx 0.08°$ and $2N \approx 10$. Points are not usually taken for angles larger than $\phi = N\Delta\phi \approx 0.4°$ because the fluctuations in scattered energy with ϕ become severe and the contribution from electronic noise becomes a consideration. Often the fluctuations in scattered energy are even severe at smaller angles, causing the data points to deviate significantly from the best-fitting straight line. However, when one determines the standard deviation in slope and intercept and plots the "highest" and "lowest" Lorentzian fit to the experimental distribution using this information, one finds that the curves tend to lie along the top and bottom envelopes determined by the local maxima and minima of the fluctuations. This situation would continue to exist even if $\Delta\phi$ were decreased and N increased, because the fluctuations correspond to uncertainties that are inherent in the experimental data and not the statistical analysis of the data.

Complications Associated with Prism-Enhanced Scattering

This situation is more complicated when prism-input coupling is used, since the effective scattering path length L is unknown, owing to the contribution from prism-enhanced scattering. The unknown quantities in Eq. 120 are now $\Sigma\sigma(\phi)$ and L, and two measurements are needed to determine these quantities separately.

As we have indicated previously, the two measurements involve the determination of the function $\Delta P(\phi)/P$ at two different waveguide prism separations, say L_g and L'_g. The effective path lengths L and L' used in Eq. 14 are

$$L = L_g + L_e \tag{125}$$

$$L' = L'_g + L'_e$$

where L_e and L'_e are the prism enhancement path lengths appropriate to the two measurements. The difference in scattered power obtained by subtracting

the two results is

$$[\Delta P(\phi)-\Delta P'(\phi)]/P = [\Sigma\sigma(\phi)](\lambda_o/Wn_g)(L_g-L'_g+L_e-L'_e) \quad (126)$$

If the prism-enhancement path length is the same in the two measurements, $L_e-L'_e = 0$ and $\Sigma\sigma(\phi)$ may be determined from the experimental data as described above.

A difficulty in the analysis of Eq. 126 is posed by the fact that $\Delta P(\phi)/P$ and $\Delta P'(\phi)/P$ are both fluctuating functions of angle. Their difference also fluctuates. It is easier to analyze the data by first obtaining the best fitting Lorentzian curve to each experiment, and then subtracting the two Lorentzians to obtain a measure of waveguide performance over the path length $L_g-L'_g$.

A weakness in the use of Eq. 126 to analyze in-plane scattering data is the fact that L_e and L'_e may not cancel. The derivations of Appendix C suggest that L_e and L'_e are more likely to be equal if the gap separating the input coupling prism and the waveguide is constant in the two measurements. This is best done by leaving the input prism constant and moving the output prism to accomplish the desired change in L_g. However, our experiments were performed prior to the derivation of prism-enhancement theory, and this was not done. For completeness we note the theoretical prediction of Appendix C that L_e itself may be made small by utilizing a broad, highly collimated input beam. This too was not done in our experiments, but should be done in future experiments of this type.

INTERPRETATION OF EXPERIMENTAL RESULTS FOR SAMPLE 154

In view of the uncertainties regarding the data obtained using input coupling prisms, we will concentrate on the interpretation of Fig. 20 obtained using end-fire coupling. We found

$$a = 11.7\ \mu m$$

$$\Sigma a^2 \delta n_g^2 = 2.25 \times 10^{-10} \quad (127)$$

from the theoretical fit to the data. We would now like to correlate these results with some of the potential sources of scattering identified in Secs. II and IV.

The quantity Σa^2 in Eq. 127 is the scattering-center surface density times scattering-center area. It corresponds to the fraction of waveguide surface covered by scattering centers. For contiguous scattering centers, such as surface-roughness undulations, $\Sigma = a^{-2}$, and Σa^2 has its largest possible value of unity. δn_g then has its smallest possible value 1.5×10^{-5}. The size of the scattering centers, $a = 11.7$ μm, suggests that we are dealing with Rayleigh-Gans-Debye (RGD) scattering. Although Mie scattering is a possibility, we have discounted its importance, in Sec. IV, because the scattering particles should be visible by microscope.

Data Interpretation Based on Scattering from Surface Compounds

Restricting our attention to RGD scattering centers having $a = 11.7$ μm and $\delta n_g \geq 1.5 \times 10^{-5}$ we see from Table I of Sec. III that the candidates are surface roughness, Ti voids, and $LiNb_3O_8$ and Li-Ti-O surface compounds. The most striking correspondence between our results and the entries of that table is in the case of scattering by surface compounds. For that scattering mechanism we combine Eqs. 76, 77, and 78 to find an expression for the mode index perturbation in terms of waveguide parameters. It is

$$\delta n_g = 4n\Delta n(n^2-1)^{-1}[Vb^{1/2}/(Vb^{1/2}+1)]\delta n(z_o/D) \qquad (128)$$

where n is the $LiNbO_3$ substrate index, Δn is the waveguide index perturbation, $V = k_o D(2n\Delta n)^{1/2}$ is the normalized waveguide depth parameter, $b \simeq (n_g-n)/\Delta n$ is the normalized mode index, δn is the index perturbation associated with the surface compounds, z_o is the depth of the surface compounds, and D is the waveguide depth.

It is instructive to estimate Δn and D from waveguide fabrication parameters τ, the Ti film thickness, t_D, the diffusion time, and T the diffusion temperature. The equations to be used are

$$\Delta n_e = 1.08\ \tau/D$$

$$D = 2[\mathcal{D}(T)t_D]^{1/2} \qquad (129)$$

where the subscript e refers to the extraordinary index and $\mathcal{D}(T)$ is the diffusion coefficient. The numerical factor 1.08 is obtained from the

experimental results of Burns, Klein, West, and Plew[7] From the same work we have $\mathcal{D}(T) = 3.6 \times 10^{-13}$ cm^2/sec at T = 950°C, the fabrication temperature for our waveguide. The waveguide was also formed using a film thickness $\tau = 315\text{Å}$ and a diffusion time $t_D = 3$h. Appendix D presents some considerations on the inaccuracy of this analysis based on uncertainty regarding the correct value of τ. Nevertheless, we find

$$\Delta n_e = 0.027$$

$$D = 1.25 \ \mu m \quad . \tag{130}$$

These results provide a normalized diffusion depth V = 4.28. From the universal curves for diffused waveguides having a Gaussian index profile,[24] we find the normalized mode index corresponding to this value of V to be b = 0.44. Inserting these results into Eq. 128 we obtain

$$\delta n_g = 0.046 \ \delta n(z_o/D) \tag{131}$$

The results of Burns et al[7] shows that $z_o/D \simeq 0.1$ for the case when $D \simeq 2$ μm. If this ratio holds for our smaller $D \simeq 1.25$ μm, we find

$$\delta n = 0.0035 \tag{132}$$

required to obtain the smallest mode index consistent with our experiment, $\delta n_g = 1.5 \times 10^{-5}$.

Some of the surface compounds that may act as the source of δn are $LiNb_3O_8$, having the three refractive indices 2.28, 2.36 and 2.40, and Li_2TiO_3, having an index of 2.09. $Li_2Ti_3O_7$ is another possibility discussed in Ref. 7 probably having a similar value for refractive index. It would appear that the largest value of δn associated with these compounds is on the order 0.1, but Ref. 7 indicates that the compounds are a reasonably dilute mixture with the host $LiNbO_3$. The authors estimate Li-Ti-O compound concentration to be less than 10 mol%. This would probably reduce the effective value of δn to about 0.01, close to what we have calculated in Eq. 132.

Another fact that indicates the correctness of these ideas is that, if δn had the value 0.1, as for segregated compounds, the compounds would probably be visible with a microscope. In accord with Eq. 131, δn = 0.1 implies that $\delta n_g = 4.6 \times 10^{-4}$. Substituting this result into Eq. 127 we find

that $\Sigma = 8\ mm^{-2}$ is the surface density consistent with the data of Fig. 20. It is difficult to imagine that this concentration of particles, 12 μm in size and having an index differential of 0.1, would be able to escape optical detection.

Data Interpretation Based on Scattering From Surface Roughness

Although we have certinly indentified one possible source for scattering of the magnitude observed in Fig. 20, let us consider the possibility that surface-roughness scattering is also compatible with that result.

For surface-roughness scattering, the effective mode index is found using Eq. 58 and 64,

$$\delta n_g = \sigma(\partial n_g/\partial D)$$

$$\partial n_g/\partial D = k_o \Delta n (2n\Delta n)^{1/2} (\partial b/\partial V) \qquad (133)$$

With $\delta n_g = 1.5 \times 10^{-5}$, $k_o = 2\pi/0.633$ μm, $\Delta n = 0.027$, $n = 2.2$, and $\partial b/\partial V \simeq 0.10$ in the vicinity of $V = 4.3$, as measured from the universal curves, we find $\sigma = 16$ Å.

This result shows that a reasonably smooth surface can still lead to significant waveguide scattering levels. This possibility was not predicted in Sec. IV owing to our use of $\Delta n = 0.007$ in calculations, rather than $\Delta n = 0.027$, as obtained for the waveguide in Fig. 20. The scattered intensity varies as Δn^3 for the surface-roughness mechanism, so the large-Δn waveguide employed here was not optimum from this point of view. It is therefore possible that the observed scattering was indeed caused by surface roughness. This mechanism could operate either in addition to or instead of the surface compound formation mechanism discussed above.

The possibility that surface roughness was the cause of the scattering in Fig. 20 occurred to us well in advance of the realization that surface compound formation was also consistent with that data. As a result, emphasis was placed on an effort to measure surface roughness in a variety of samples and correlate the results with in-plane scattering levels for the same samples. This was done to further demonstrate (or disprove) the correspondence between surface roughness and observed waveguide scattering. The nature and the results of these experiments is described later.

Data Interpretation Based on Scattering from Ti Voids

In Secs. II and IV we considered the possibility of scattering from regions where, for one reason or another, Ti did not enter the waveguide. Particulate matter trapped beneath the evaporated film was cited as one source of this type of scattering. The mode-index change is approximately given by

$$\delta n_g = n_g - n \approx b\Delta n$$

In our experiment $\delta n_g = 0.44 \times 0.027 = 0.012$. In order to satisfy Eq. 127, we require the surface density of scattering centers to be $\Sigma = .012\ \text{mm}^{-2}$. The total number of scattering particles would be $\Sigma LW \sim 1$ since L = 15 mm and W = 1 mm. It is conceivable that one scattering particle could escape detection. Yet the observed scattered energy distribution would be in reality a diffraction pattern having regular features associated with the geometry of the particle. This is in contrast to what we observe. Therefore we discount this as an important scattering mechanism in our experiment.

Potential for Improved Scattering Performance

Later we will discuss possible methods for reducing scattering in $LiNbO_3$ waveguides by reducing the strength or number of scattering centers such as surface roughness and surface compounds. At this point let us consider the scattering level that might have been achieved simply by fabricating the waveguide of Fig. 20 differently, without any attempt at reducing the strength of scattering centers. Had we increased the diffusion temperature to 1000°C, at which $\mathcal{D}(T) = 9.4 \times 10^{-13}\ \text{cm}^2/\text{sec}$,[7] and the diffusion time to 8h, the diffusion depth would have been 3.29 μm instead of 1.25 μm. Had we decreased the Ti film thickness to 150Å from 315Å, the value of Δn_e would have been 0.0049, down from 0.027. The normalized depth of the waveguide would have been V = 4.79, corresponding to a normalized mode index b = 0.45. We continue to use db/dV = 0.1, δn = 0.0035 and σ = 16 Å.

AD-A096 815 BATTELLE COLUMBUS LABS OH F/G 20/6
OPTICAL WAVEGUIDE SCATTERING REDUCTION. II.(U)
DEC 80 D W VAHEY, N F HARTMAN, R C SHERMAN F33615-79-C-1852
UNCLASSIFIED AFWAL-TR-80-1186 NL

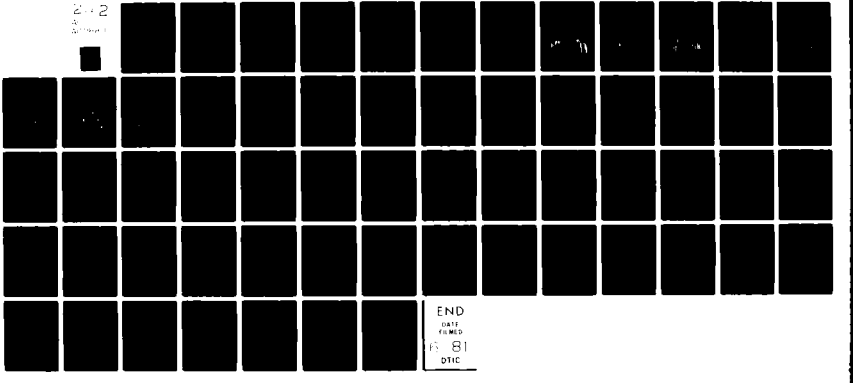

END
DATE FILMED
4-81
DTIC

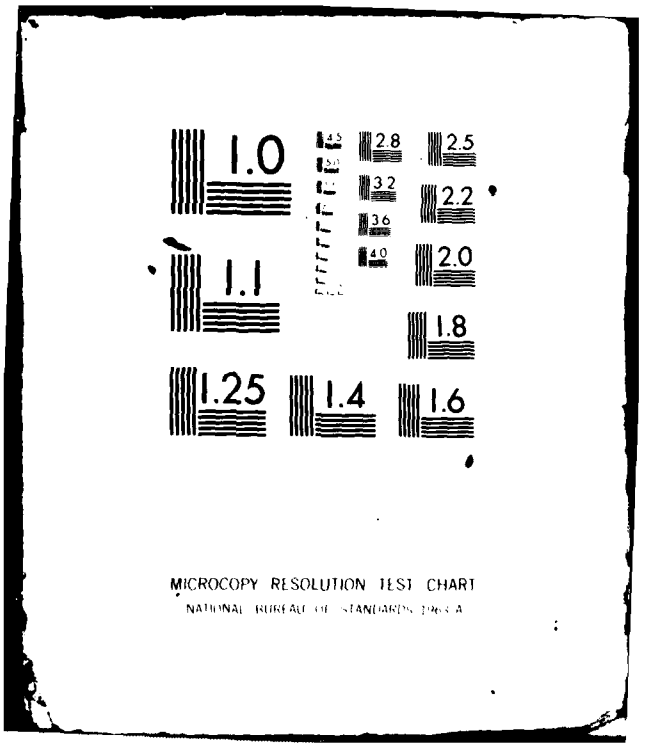
1.0
1.1
1.25
1.4
1.6
1.8
2.0
2.2
2.5
2.8
3.2
3.6
4.0
MICROCOPY RESOLUTION TEST CHART
NATIONAL BUREAU OF STANDARDS 1963 A

In the case of scattering from surface compounds, Eq. 128 now yields $\delta n_g = 3.0 \times 10^{-6}$, compared to 1.5×10^{-5} for the present waveguide. This implies a factor 25 reduction in scattered intensity. A spectrum analyzer utilizing the proposed waveguide would have a dynamic range of 40.8 dB, up from 26.8 dB predicted for the waveguide of Fig 20.

In the case of scattering from surface roughness, Eq. 133 now yields $\delta n_g = 1.1 \times 10^{-6}$, down from 1.5×10^{-5}. This implies a factor 184 reduction in scattered intensity. A spectrum analyzer utilizing the proposed waveguide would have a dynamic range of 49.4 dB, up from 26.8 dB.

These results are highly encouraging from the point of view of ultimately fabricating waveguides suitable for a spectrum analyzer. A note of caution is that geodesic lens radiation losses may increase with the introduction of waveguides that are optimum from a scattering point of view. Also note that prism-enhanced scattering increases with smaller Δn and larger D. This means that the superior scattering performance of such waveguides may not be apparent if they are tested using prism input coupling.

The careful reader may have noticed that the data of Fig. 20 is for TM_o propagation, while the data is analyzed using a formalism developed for TE_o modes. We justify this on the basis that data taken for the TE_o mode on the same sample (154) was quite similar in appearance to the data of Fig. 20 (see Fig. 29 on page 107).

OTHER IN-PLANE SCATTERING EXPERIMENTS

The in-plane scattered-energy distribution of Fig. 20 was obtained approximately midway through the program. Earlier data was taken on a variety of samples to test the relative merits of a substrate polish performed at Battelle and to compare scattering from indiffused and outdiffused waveguides. Sample 154 of Fig. 20 was prepared to test the effects of a new sample cleaning procedure, but the evidence for surface-roughness scattering from that waveguide had a strong influence on later experiments performed during the program. These were performed primarily to demonstrate the correlation or lack of correlation between measured levels of surface roughness and waveguide scattering.

We now examine these experimental results to see what additional light they shed on the understanding of waveguide-scattering phenomena. Keep in mind that the data for each waveguide were acquired with two different coupling-prism separations to cancel the effects of prism-enhanced scattering. The results are meaningful only to the extent that prism-enhanced scattering was the same in the two measurements.

Sample Histories

Ti-Film Deposition

Table II identifies the samples used in the program and presents relevant details concerning their fabrication. The substrates were purchased from Crystal Technology. They were 25mm x 25mm x 3mm in volume and polished to $\lambda/10$ flatness on both 25mm x 25mm surfaces. HP-6 was from a high-purity batch while the others were selected acoustic grade. It is likely that at least four different boules are represented by the samples used in the program.

Ti-film thicknesses were measured with a crystal monitor during their deposition by e-beam evaporation. The monitor was calibrated using an angstrometer. No account was taken of the fact that the measured thickness is not that of pure Ti but is that of an unknown oxide, depending on the purity of the vacuum system. This problem is addressed in Appendix D. Ti films deposited on samples 154 and 155 probably had a greater proportion of Ti than did other samples documented in Table II, owing to the use of a tighter vacuum system.

TABLE II. FABRICATION HISTORY OF $LiNbO_3$ WAVEGUIDES USED IN THE PROGRAM

Sample Identification	HP-6	135	154	155	166	168	169
Fabrication Date	8/2/79	8/23/79	11/2/79	11/7/79	3/20/80	3/25/80	4/1/80
Cleaning Procedure	Solvent, Detergent, Rinse, Swab	Solvent, Detergent, Rinse, Swab	Syton Polish, Methanol, Wipe	Syton Polish, Methanol, Wipe	Detergent, Rinse, Swab	Detergent, Rinse, Swab	Detergent, Rinse, Swab
Nominal Ti-film Thickness	270 Å	270 Å	315 Å	175 Å	175 Å	0 Å	600 Å
Expected Oxygen Content of Film	Higher	Higher	Lower	Lower	Higher	--	Higher
Diffusion Temperature	950°C	950°C	950°C	950°C	950°C	950°C	1000°C
Time	3h	3h	3h	3h	3h	1h	8h

Thermal Diffusion

All diffusions were carried out in flowing oxygen rather than in argon, as is done in some laboratories.[7,30] This procedure was developed at Battelle to simplify fabrication by eliminating the need for a post-diffusion heat treatment in oxygen.[31] However, the fact that oxygen plays an important role in the diffusion process means that the diffusion atmosphere could have an impact on waveguide quality. We did not test this, though it would have been worthwhile to do so.

Following the diffusion heat treatment, samples were rapidly quenched to 600° by moving them to the edge of the hot zone of the tubular oven. Then the samples were brought to room temperature in a time comparable to or longer than 30 min. The quench to 600°C is performed to minimize the time spent in the 800-850°C temperature range, where surface defects can be produced as a result of the generation of the separated phase $LiNb_3O_8$.[1,14] We have observed this degradation in samples allowed to cool slowly overnight, and in samples that were intentionally allowed to remain at 800-850°C for times on the order of ten minutes. A rapid quench from the diffusion temperature to 600°C is probably not required, although we generally performed the quench in a few seconds.

Cleaning Procedure

The method used to clean $LiNbO_3$ substrates for waveguide fabrication has been subject to considerable evolution over the years that Battelle has had experience in the area. Two approaches are now dominant. One that minimizes contact with the $LiNbO_3$ surface has as its principle features a soak in "Micro" detergent, follwed by a long (5 min) rinse in hot, filtered tap water, and concluded with a short rinse in hot distilled tap water. Variations on the main theme include ultrasonic agitation of the "Micro" and a concluding bake out at 250°C. If the sample is not baked, it is blown dry with filtered air or N_2. Slight swabing of the surface with a cotton swab is permitted during the early rinsing stages. Otherwise there is no contact with the surface.

A problem with minimizing surface contact has to do with the very strong electrostatic attraction that $LiNbO_3$ exerts on airborne particulates.

Surface dust is not easily rinsed away. An approach that we have found successful has been to first subject the sample to a "final polish" with colloidal silica. This physically removes firmly attached dust and other residue. Then the sample is wiped once with a "Kleenex" or a lintless wipe that has been wetted with methanol. If the sample has been recently sawed, care must be taken to insure that loose chips are not dragged across the surface in this step. Nomarski microscopy reveals a clean, nearly dust-free surface.

This cleaning procedure was used for samples 154 and 155, while other samples cleaned during the program were cleaned using the minimum-contact approach. We somewhat prefer the contact appraoch for its simplicity and effectiveness, but we also believe that it doesn't make much difference which method is used as far as waveguide scattering is concerned. Our results suggest that the scattering level associated with cleaning-related scattering centers is not very great.

Sample HP-6

HP-6 was from a high-purity boule of $LiNbO_3$ that was left over from a previous program. The sample was ground and polished to the extent that the effects of previous diffusions and heat-treatments were in all likelihood eliminated. Then a waveguide was prepared on the substrate according to the description in Table II.

It was believed that the scattering level from this sample, when compared with that from a waveguide formed on a Crystal-Technology prepared substrate, would indicate the potential for scattering from surface roughness and/or subsurface polishing imperfections that might exist in one or the other to a greater degree.

Sample 135

Waveguide sample 135 was fabricated in a similar fashion to HP-6 in order to make the comparison indicated above. Also, sample 135 contained a surface area approximately 25 mm x 6 mm that was not diffused with Ti, and hence supported an outdiffused waveguide. The reason for this was to allow comparison of scattering from indiffused and outdiffused waveguides formed on the same

substrate. Unfortunately, the outdiffused portion was only tested without correction for prism-enhanced scattering, so this comparison could not be made. An outdiffused waveguide was, however, carefully made and tested later in the program.

Samples 154 and 155

These samples were initially fabricated to test the influence of surface cleaning procedures on $LiNbO_3$ waveguide scattering. However, following the analysis of the data for 154, shown in Fig. 20, it was felt that surface roughness was a more significant source of scattering. Subsequent samples used in the program were fabricated with this possibility in mind.

Samples 166, 168, and 169

These samples were designed for a series of measurements in which waveguide scattering was to be measured as a function of surface roughness. Roughness was to be varied by post-diffusion polishing of the waveguide surface. Sample 166 was fabricated from a relatively thin, 175-Å Ti film. A thin film was employed to minimize the upheaval of the topography of the $LiNbO_3$ surface caused by the diffusion process. This upheaval was surmised from measurements made on sample 154, in which the scattered component of light reflected from the surface at about 90° suggested a roughness of about 30 Å (see Appendix E) or an order of magnitude greater than the NBS- measured roughness for an undiffused substrate (see Appendix A).

Sample 169 was diffused from a relatively thick, 600 Å Ti film. This was done to provide contrast with sample 166, and also to permit checking of the results of the Phase I program,[1] which showed the best scattering performance to be provided by a heavily diffused waveguide that was subjected to a long post-diffusion polish.

Sample 168 was an outdiffused waveguide formed to verify that topographical upheaval of the surface was indeed related to Ti indiffusion, and also to provide the comparison of scattering from indiffused and outdiffused waveguides that was mentioned earlier in connection with sample 135.

Experimental Results for Samples Other Than 154

Scattered-Energy Distributions for Separated and Adjacent Input and Output Prism Couplers

In Figs. 21-28 we present in-plane scattered-energy distributions for the samples whose histories have just been described. In each experimental distribution, the solid curve shows scattering observed when the prism separation was about 15 mm. The dashed curve shows the scattering observed when the prism separation was as close as could be conveniently obtained, about 1-2 mm. The distributions have been truncated at -20 dB so the main peaks associated with unscattered light are off-scale. The scattering angles shown along the horizontal axis are those which would be measured in the waveguide material.

The smooth curves shown in the figures are the Lorentzian-shaped theoretical fits to the data obtained by methods discussed earlier in this section. These curves are solid or dashed in correspondence to the experimental data that they fit. Table III summarizes the theoretical results. This table presents the scattering level at 0° and 1° measured in air [(1/n)° measured in the waveguide], as provided by the theoretical fit for both separated and adjacent coupling prisms.

Interpretation of Results

It is desired to evaluate waveguide scattering by subtracting the scattering level obtained using adjacent prisms from that obtained using separated prisms. The results of this calculation are shown in row 5 of Table III. Three entries are omitted: Samples HP-6 (TE_o mode, $k \perp c$) and 135 (TE_o mode, $k \perp c$) show a negative scattering contribution from the waveguide, while sample 155 (TM_o mode, $k \parallel c$) shows a very large scattering that belies the close match between experimental curves seen in Fig. 24.

Results for other samples show that 166, 168, and 169 have the lowest scattering levels, near -36 dB and comparable to that obtained for sample 154. Samples 135 and 155 have scattering levels approximately 10 dB greater. In view of the fact that the fluctuations in scattered energy for many of the samples

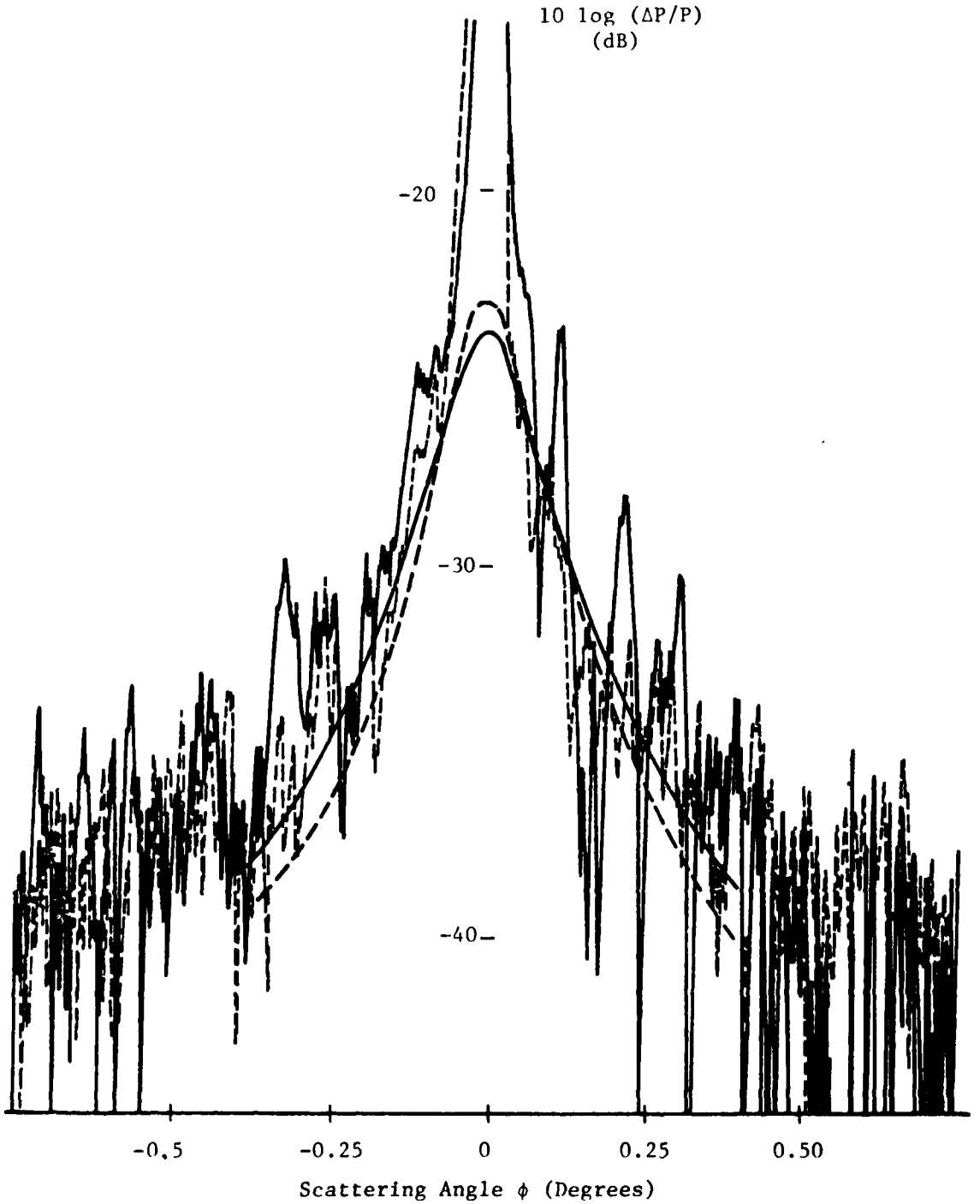

Fig. 21. In-plane scattering energy distribution for sample HP-6 (TE_o mode, $k \perp c$), taken with separated coupling prisms (solid curves) and adjacent coupling prisms (dashed curves). Bell-shaped curves are theoretical. Scattering angles are referenced to waveguide material.

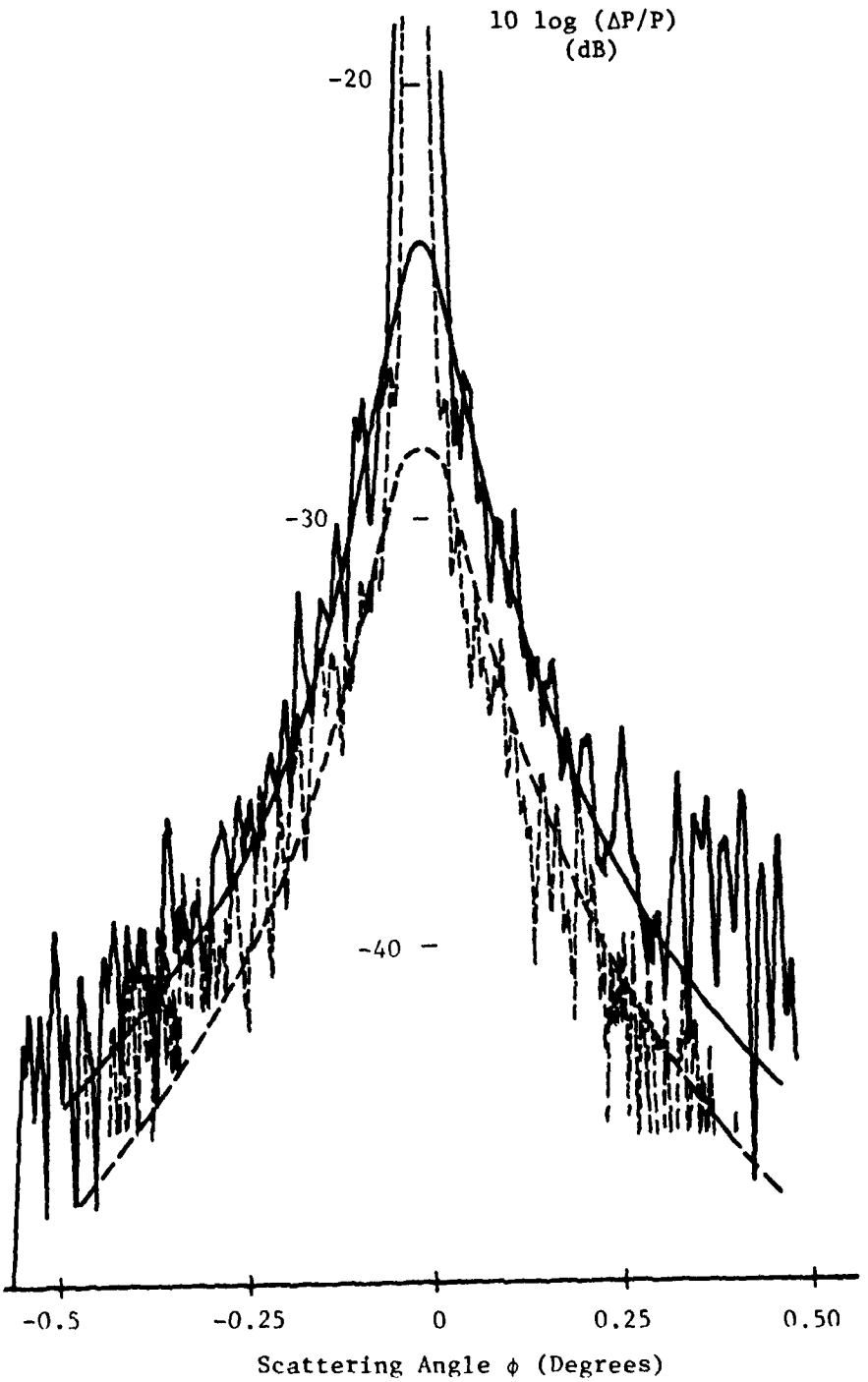

Fig. 22. In-plane scattering energy distribution for sample 135 (TM_o mode, $k \perp c$), taken with separated coupling prisms (solid curves) and adjacent coupling prisms (dashed curves). Bell-shaped curves are theoretical. Scattering angles are referenced to waveguide material.

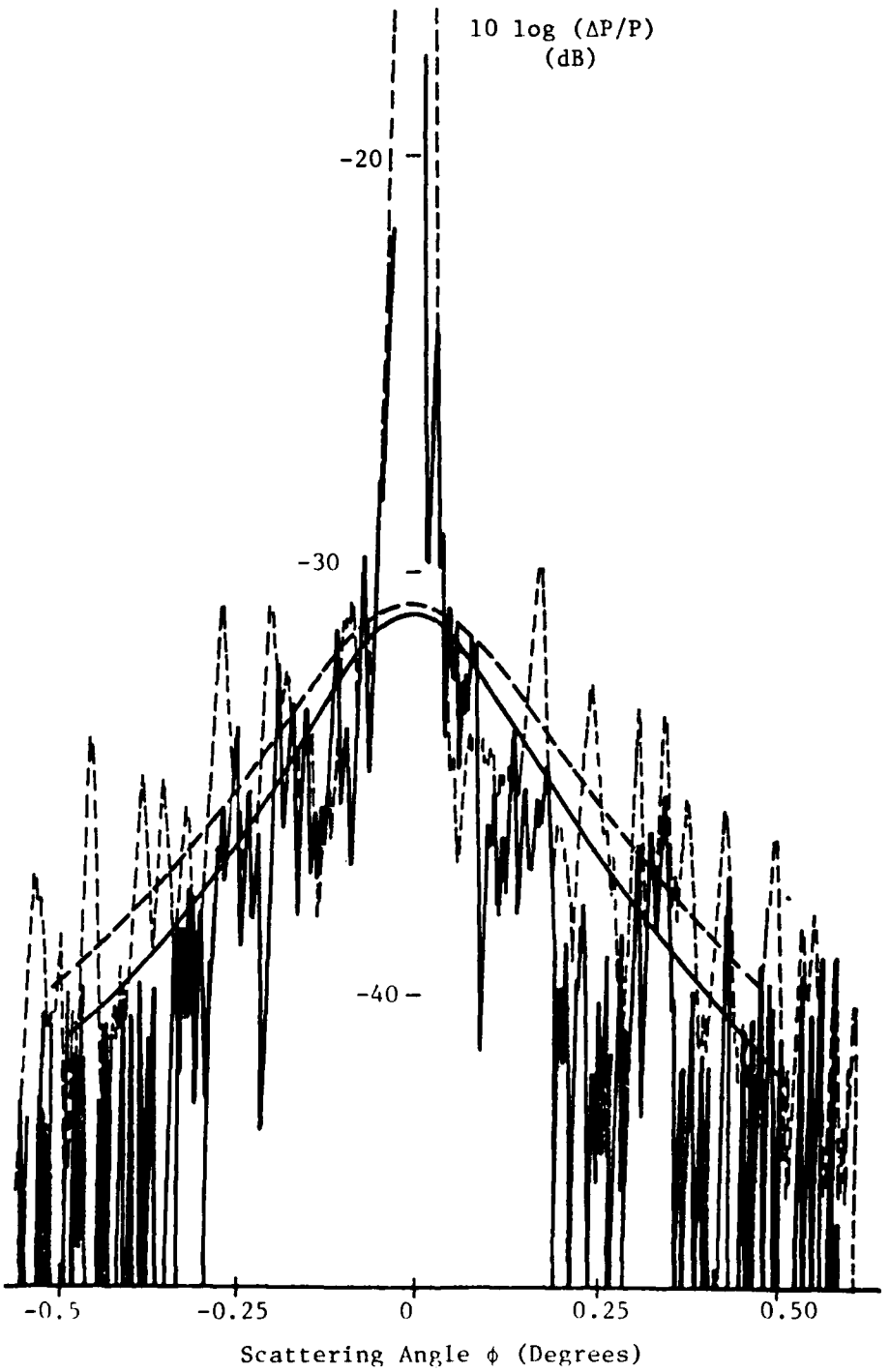

Fig. 23. In-plane scattering energy distribution for sample 135 (TE_0 mode, $k \perp c$), taken with separated coupling prisms (solid curves) and adjacent coupling prisms (dashed curves). Bell-shaped curves are theoretical. Scattering angles are referenced to waveguide material.

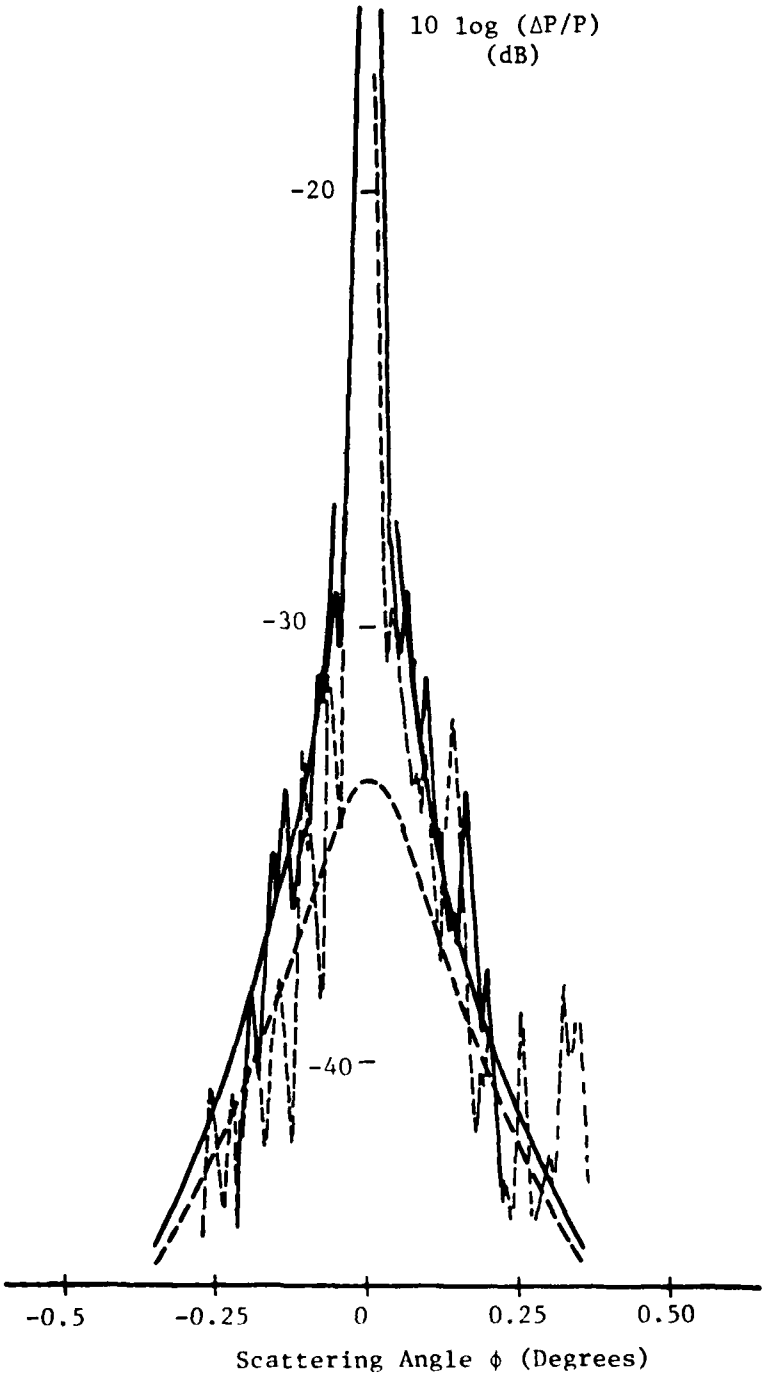

Fig. 24. In-plane scattering energy distribution for sample 155 (TM_o mode, k||c), taken with separated coupling prisms (solid curves) and adjacent coupling prisms (dashed curves). Bell-shaped curves are theoretical. Scattering angles are referenced to waveguide material.

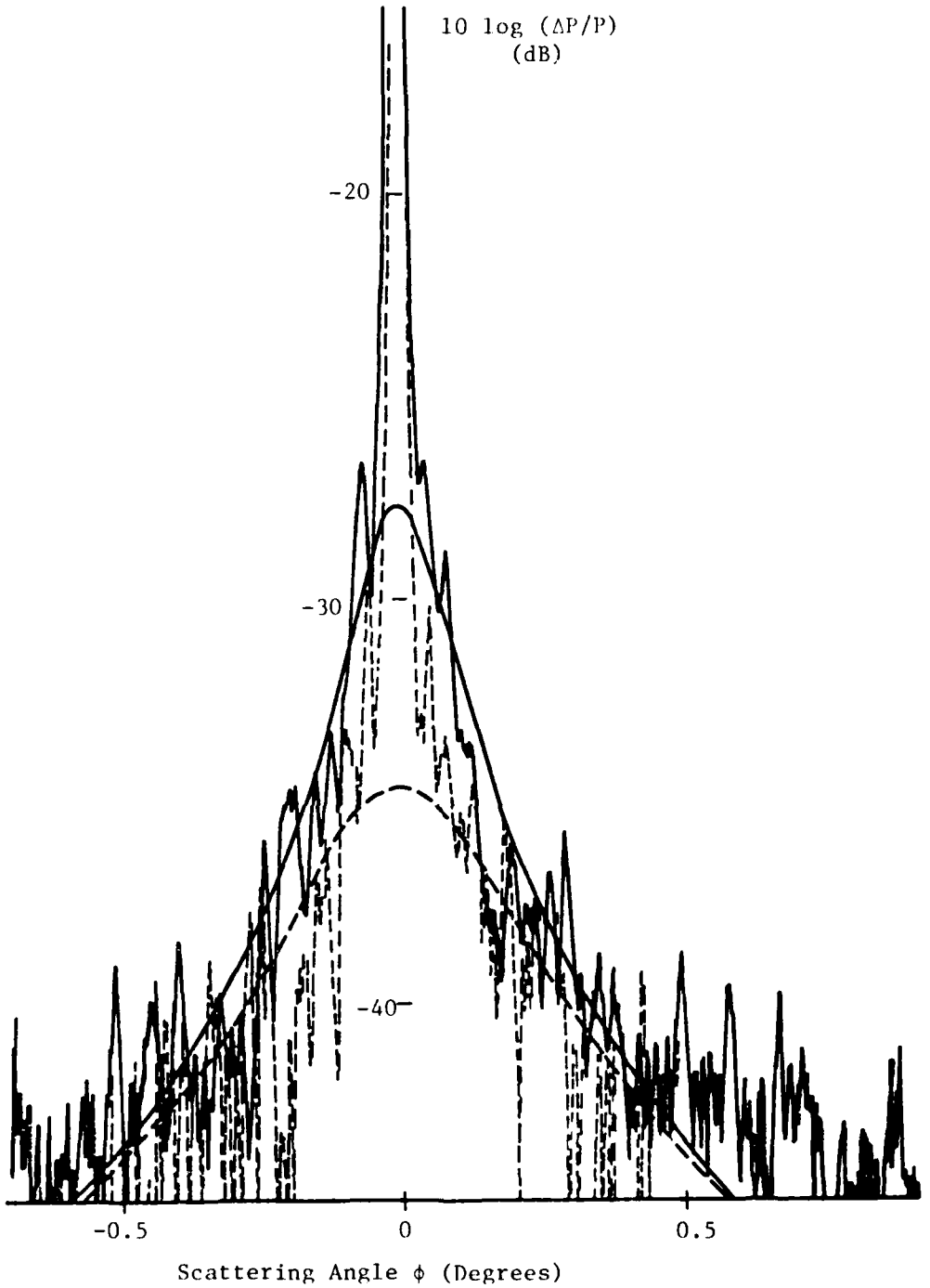

Fig. 25. In-plane scattering energy distribution for sample 155 (TM_0 mode, $k \perp c$), taken with separated coupling prisms (solid curves) and adjacent coupling prisms (dashed curves). Bell-shaped curves are theoretical. Scattering angles are referenced to waveguide material.

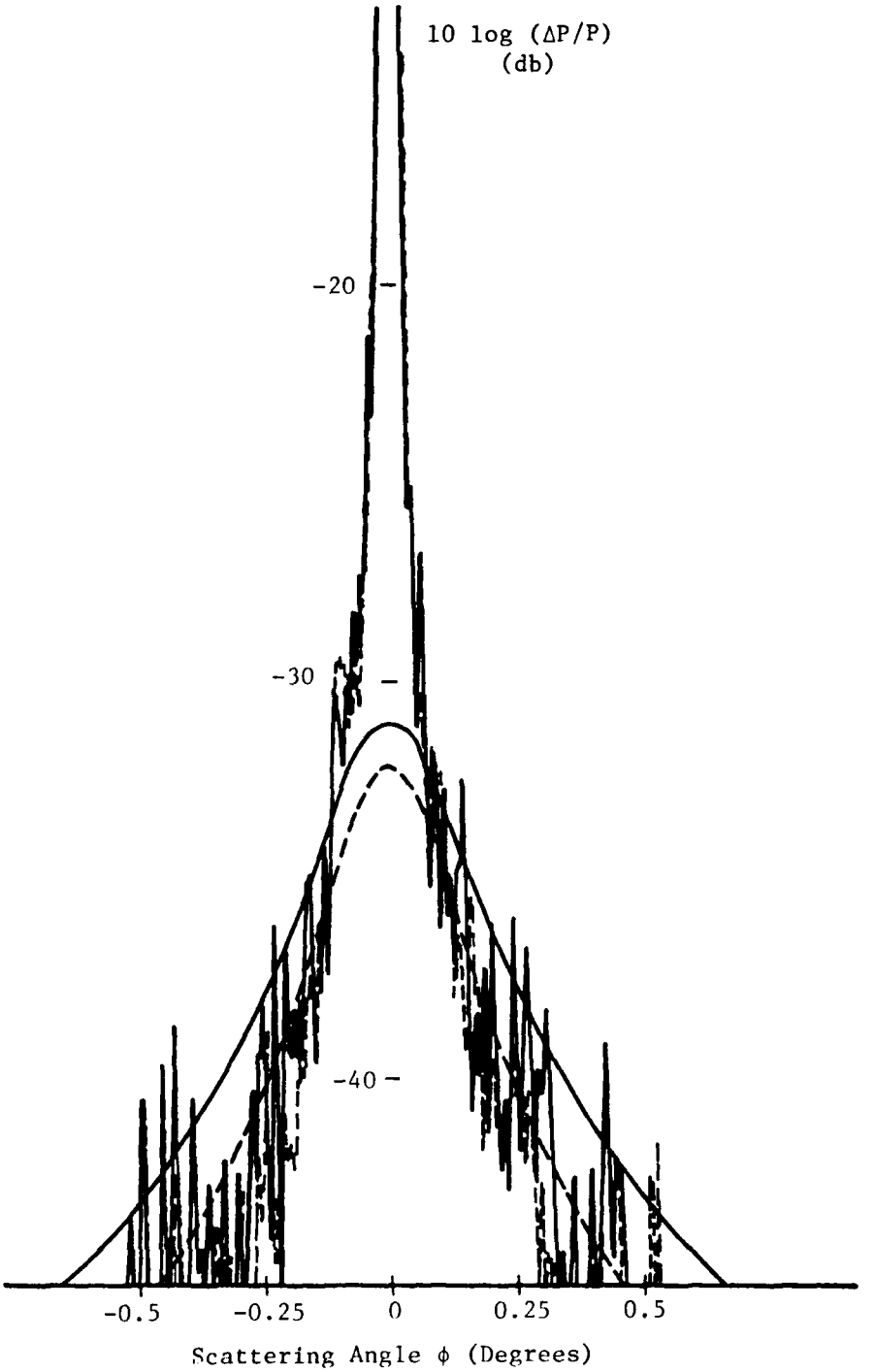

Fig. 26. In-plane scattering energy distribution for sample 166 (TM_o, $k \perp c$), taken with separated coupling prisms (solid curves) and adjacent coupling prisms (dashed curves). Bell-shaped curves are theoretical. Scattering angles are referenced to waveguide material.

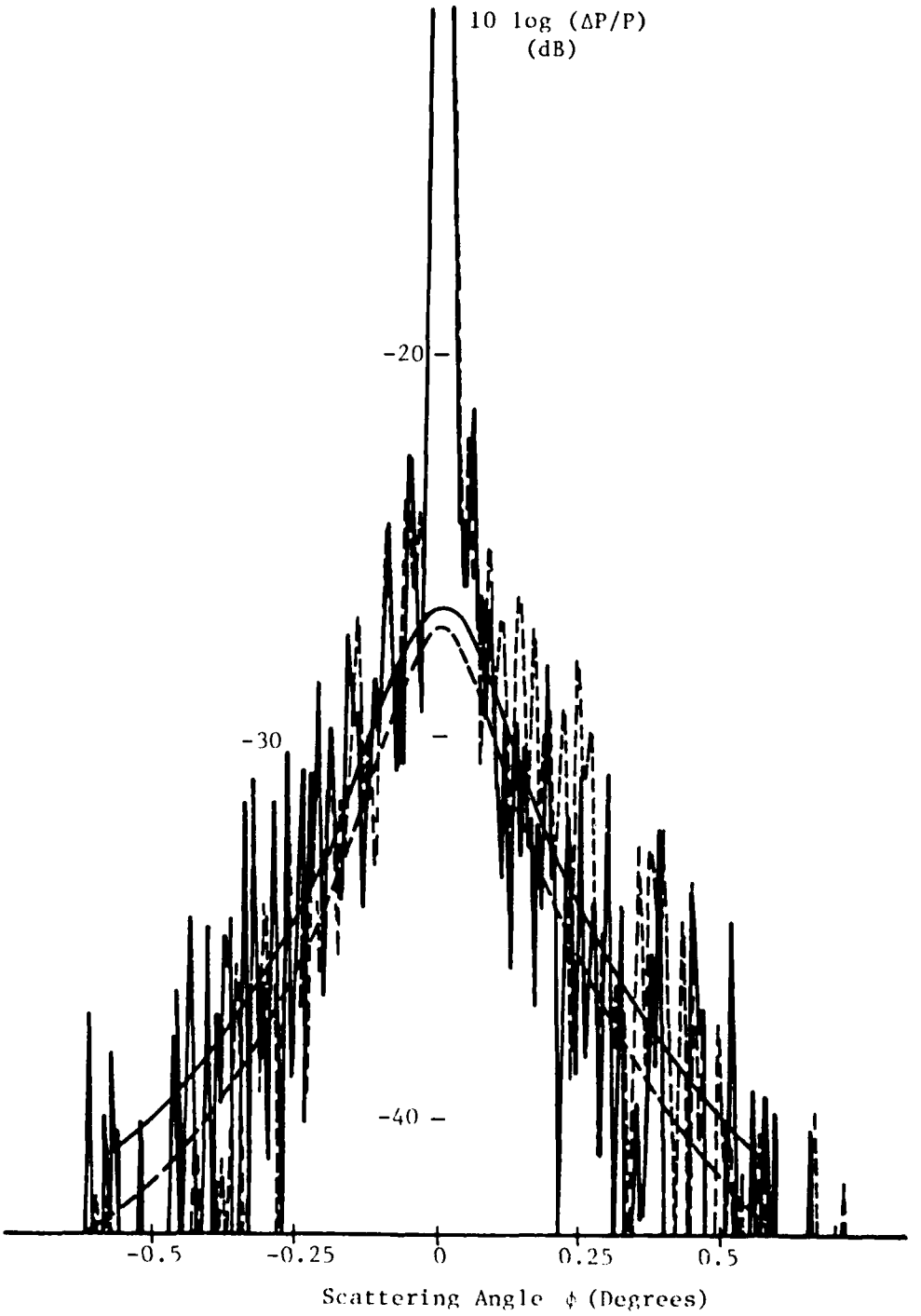

Fig. 27. In-plane scattering energy distribution for sample 168 (TE_o, k⊥c), taken with separated coupling prisms (solid curves) and adjacent coupling prisms (dashed curves). Bell-shaped curves are theoretical. Scattering angles are referenced to waveguide material.

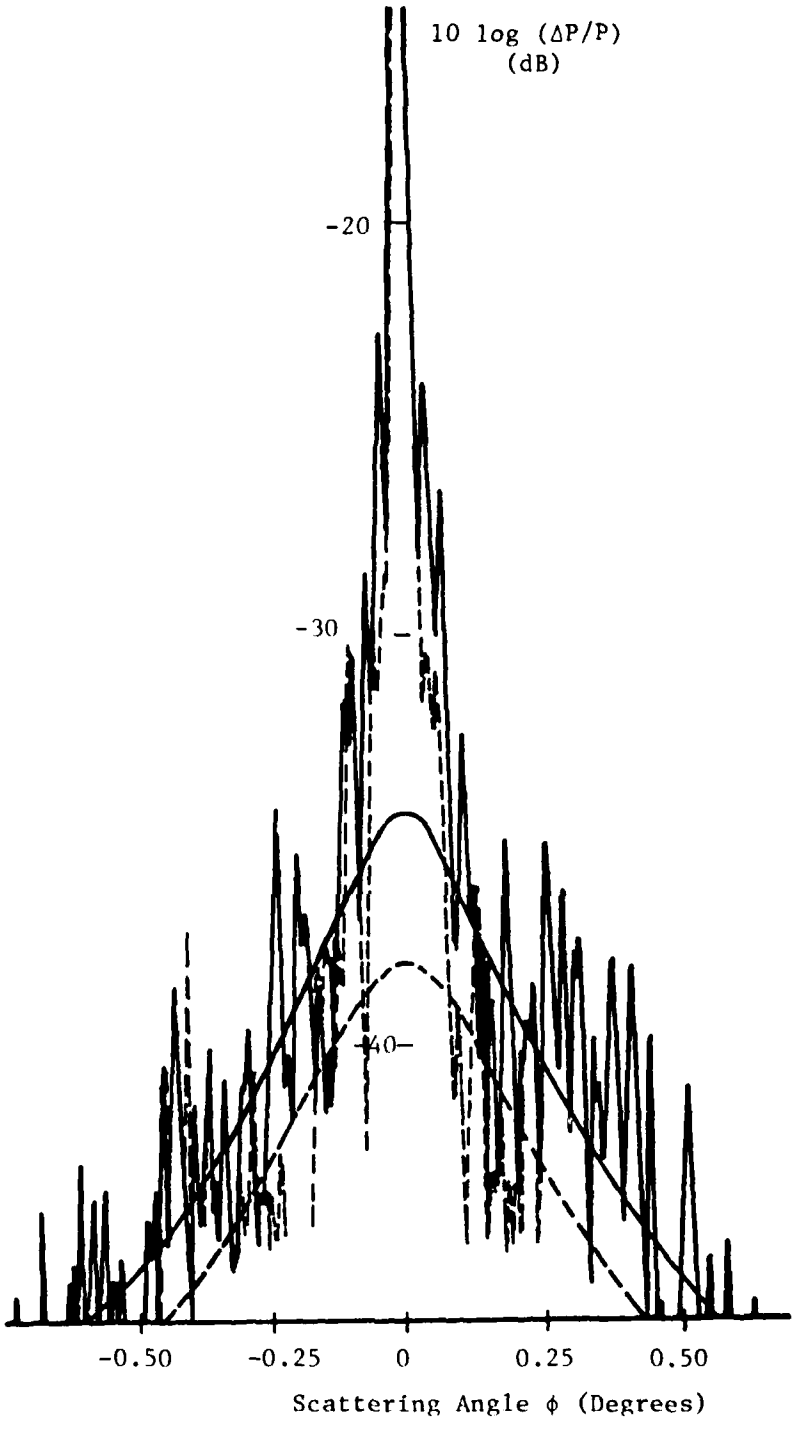

Fig. 28. In-plane scattering energy distribution for sample 169 (TM_0, $k \perp c$), taken with separated coupling prisms (solid curves) and adjacent coupling prisms (dashed curves). Bell-shaped curves are theoretical. Scattering angles are referenced to waveguide material.

TABLE III. SCATTERING LEVELS CALCULATED FROM IN-PLANE SCATTERED-ENERGY DISTRIBUTIONS OBTAINED USING SEPARATED AND ADJACENT COUPLING PRISMS

Sample Identification	HP-6	135	135	155	155	166	168	169
Mode	TE_o	TM_o	TE_o	TM_o	TM_o	TM_o	TE_o	TM
Propagation Direction	$k \perp c$	$k \perp c$	$k \perp c$	$k \parallel$	$k \perp c$	$k \perp c$	$k \perp c$	$k \perp c$
On-axis Scattering (0°),dB								
From Prism	-22.10	-28.29	-30.81	-33.50	-34.73	-32.13	-27.08	-37.90
From Prism + Waveguide	-23.80	-23.42	-31.02	-11.75	-27.63	-30.97	-26.49	-34.31
From Waveguide (calculated)	--	-25.13	--	--	-28.57	-37.27	-35.45	-36.81
Experimental Fluctuation in Scattered Energy (dB)	$\pm$3	$\pm$1	$\pm$2.5	$\pm$1.7	$\pm$1.2	$\pm$2	$\pm$3.4	$\pm$4
Off-axis Scattering (1° in air), dB								
From Prism	-41.21	-45.22	-39.25	-46.25	-42.73	-44.60	-40.25	-46.58
From Prism + Waveguide	-39.79	-42.61	-40.74	-46.04	-42.30	-41.77	-38.69	-44.42
From Waveguide (calculated)	-45.34	-46.06	--	-59.3	-52.56	-44.97	-43.89	-48.49

(row 6) was comparable to the changes in scattering produced using separated and adjacent coupling prisms, it is difficult to know what significance to attach to these results. Let us, therefore, consider the entries of Table III from a different point of view.

Taken as a whole, the data show the dominance of scattering from the prism-coupling region over that from the free waveguide. Since prism scattering results from an enhancement of scattering from waveguide imperfections in the input-coupling region, those waveguides with the lowest inherent scattering will also have the lowest prism-enhanced scattering. We can thus determine the best samples in Table III by looking for those with the lowest scattering as measured with adjacent coupling prisms. A critical assumption is that the proportionality constant relating inherent waveguide scattering to prism scattering is the same for all waveguides. Exceptions to this will have to be discussed individually.

An examination of row 3 in Table III, for on-axis scattering and adjacent coupling prisms, shows HP-6 to be the worst waveguide tested, having a scattering level of -22 dB. Recall that this was the only sample not polished by the supplier, Crystal Technology. Waveguides 155 and 166 are now found to be comparable in performance and superior to 135. In row 5, 166 was superior to both 155 and 135, which were comparable. We are thus inclined to rank the three samples in order of increasing quality as follows: 135 (poorest), 155 (intermediate), and 166 (best). This is significant because the waveguides were fabricated with slightly different procedures: 135 was diffused from a thicker Ti film than were 155 and 166 (270 Å instead of 175 Å), while 155 was formed from a film evaporated in a tighter vacuum system than was the film used for 166. Our results suggest that the use of a thin, oxygen-rich Ti film will improve waveguide quality, presumably by impeding the formation of Li-Ti-O surface compounds and by minimizing any surface roughness that may be induced by the diffusion process.

Outdiffused waveguide sample 168 presents a paradox in that it shows quite low scattering obtained as the difference between data for separated and adjacent coupling prisms, yet the absolute scattering level measured with adjacent coupling prisms in higher than for any sample in Table III except HP-6, Outdiffused waveguides are expected to have less scattering than indiffused waveguides because they are immune to scattering from Li-Ti-O surface compound

formation and from diffusion-induced surface roughness. This can be reconciled with the high level of scattering observed for adjacent coupling prisms only if we assume a large degree of prism-enhanced scattering. This is in agreement with the predictions of Appendix C. Equation C-17 indicates that prism-enhancement varies in proportion to $(D/\Delta n)^2$, where D is the waveguide depth and Δn is the surface index change. This ratio can be two orders of magnitude larger in an outdiffused waveguide than in an indiffused waveguide. We are thus confident in asserting that sample 168 is one of the better-quality waveguides tested.

The last sample to consider in Table III is sample 169. This waveguide shows the best scattering performance of any waveguide in the table, by either of the two criteria that we have employed. This is surprising, because the fabrication conditions were deliberately chosen to produce an inferior waveguide. A 600 Å-thick Ti film was diffused to produce Li-Ti-O surface compound formation and diffusion induced surface roughness. It was planned to monitor waveguide quality improvement by performing post diffusion polishing of the sample, as was done in Ref. 1. In that work, 720 Å-thick Ti films diffused for three hours showed considerable surface granularity which we associated with surface compound formation. In a waveguide formed similarly to 169, only very slight granularity was observed. Our interpretation is that the higher diffusion temperature (1000°C instead of 950°C) and longer diffusion time (8 h instead of 3 h) cause the surface compounds to break up, forming a more homogeneous waveguide layer. However, caution must be exercised in interpreting the results of Table III for this sample, since the extent of prism-enhanced scattering is not known and can not be easily predicted. Both Δn and D are larger for this waveguide, and the ratio $(D/\Delta n)^2$ describing prism enhancement may be greater than, less than or comparable to that for other indiffused samples in the table.

Connection with Previous Results

In summary, it appears that the best waveguides are obtained by fabrication procedures that minimize disruption of the sample surface, either by surface compound formation or diffusion induced roughness. We find from experiment that this can be done by the use of thin Ti films having a high oxygen content and/or by the use of long diffusion times and high temperatures. Both techniques should lead to smaller values of Δn and larger values of D, which the

theory of Sec. IV shows to be conducive to low scattering cross sections. Thus our experimental results are qualitatively supportive of the theory. Unfortunately, they do not go far enough toward determining the best waveguide scattering that may be obtained. That is the case because we concentrated in our experiments on sources of scattering that were related to waveguide handling procedures such as polishing and cleaning, rather than to waveguide diffusion conditions, such as diffusion time, temperature and Ti-film thickness. This choice was made because the results of the Phase I program[1] suggested that it was appropriate. We now believe that many of these results were improperly influenced by prism-enhanced scattering.

The last samples examined in the current program, 166, 168, and 169, show an appropriate shift in emphasis to the study of diffusion conditions and their effects on scattering. Unfortunately, significant time was lost in attempting to develop end-fire coupling techniques and an in-depth study was not possible. The most serious loss was a set of experiments to evaluate the effects of post-diffusion polishing of various waveguide samples. These experiments would have provided information regarding the relative importance of diffusion-induced surface roughness and surface compound formation, and could have resulted in a more definitive recipe for low scattering waveguides. As the current program ends, we know the desirability of fabricating waveguides with small Δn and large D, but we do not know the optimum way to achieve these conditions, whether by heavy post-diffusion polishing of waveguides formed using thick Ti films or by light post-diffusion polishing of waveguides formed using thin Ti films and longer hotter diffusion treatments.

Our initial attempts to answer these questions involved the development of a reflection scattering technique to measure surface roughness. This technique was mentioned previously in connection with sample 154, where it was used to verify that the surface roughness of that sample was enough to cause the observed level of scattering. We planned to make repeated use of this technique following post-diffusion polishes of waveguides in the 160 series to more precisely correlate waveguide scattering with surface roughness. Some initial results with these waveguides are described in Appendix E.

In order to complete our presentation of in-plane scattering data we include as Fig. 29 the scattered energy distribution for sample 154 taken using end-fire input coupling of TE_o polarized light.

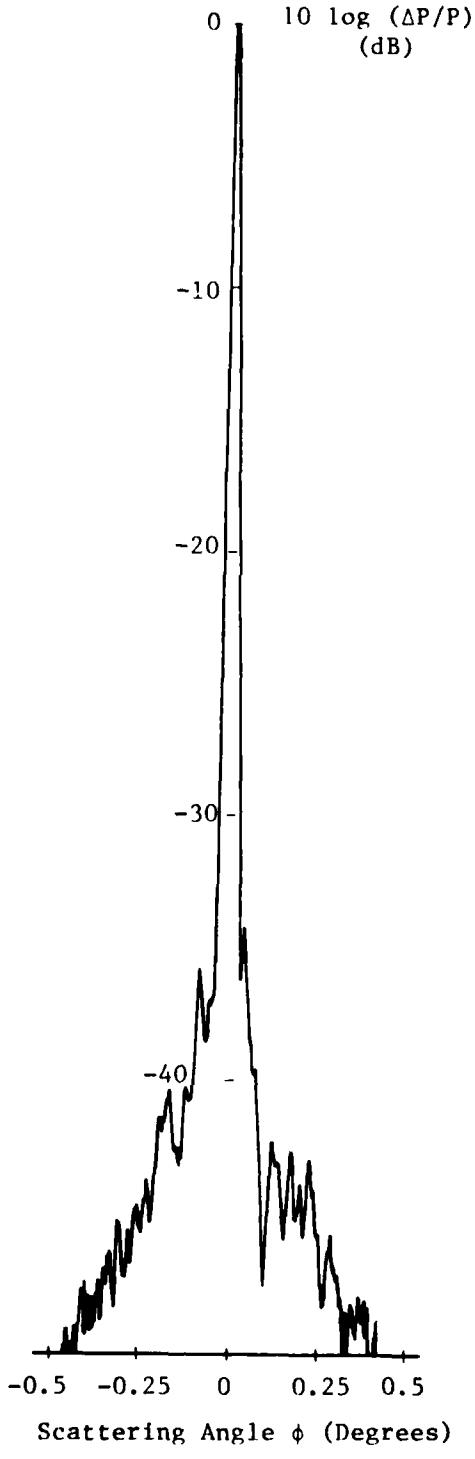

Fig. 29. In-plane scattered energy distribution for sample 154 (TE_o mode, $k \perp c$) obtained using end-fire input coupling.

VI. SUMMARY AND CONCLUSIONS

This report has described an intensive investigation of sources of scattering in $LiNbO_3$, Ti-diffused optical waveguides. The investigation, primarily experimental in nature, has been complicated by experimental difficulties of the type which escape immediate detection, and which, when discovered, frustrate correction. I speak primarily of the problems associated with prism-enhanced scattering and the unsuccessful attempt to eliminate them by the polishing of edges for end-fire coupling. These problems have limited the scope of the program to the extent that waveguides other than Ti-diffused $LiNbO_3$ were not investigated. We have, however, managed to interpret the data obtained for $LiNbO_3$ through the use of extensive (and initially unanticipated) calculations, so that important conclusions are drawn with regard to the suitability of the material for integrated-optical signal-processing applications such as the spectrum analyzer. While we have not experimentally studied other candidate waveguides for these applications, we note that our calculations are relevant to all waveguides having a small surface-to-substrate index change Δn. In addition, our treatment of the scattering associated with prism coupling and our findings regarding the polishing of edges for end-fire coupling should prove useful to those whose concern is with silicon-substrate waveguides as well as with $LiNbO_3$.

A listing of the achievements of the program follows:

- Identification of potential sources of scattering in Ti-diffused $LiNbO_3$ waveguides.
- Comprehensive listing of experimental methods useful for the study of waveguide scattering sources, including experimental results for those we employed.
- Calculation of spectrum-analyzer dynamic range in terms of scattering cross sections, scattering-center densities, and spectrum-analyzer geometry.
- Derivation of formulas for in-plane scattering cross sections for Mie, Rayleigh-Gans-Debye, and Rayleigh scattering centers

- Analysis of scattering associated with prism coupling.
- Investigation of edge-polishing techniques for end-fire coupling.
- Development of procedures for data acquisition and analysis in the presence of prism-enhanced scattering.
- Development of a qualitative but highly sensitive experiment for detection of in plane scattering at 90°.
- Measurement of surface roughness associated with Ti diffusion using a reflection-scattering experiment.
- Testing and evaluation of in-plane scattering in $LiNbO_3$ waveguides formed using a wide variety of fabrication procedures.

The research summarized by these achievements has led us to conclude that $LiNbO_3$ is an eminently useful substrate for the spectrum-analyzer application.[2]

We find that the initial substrate, as polished by the supplier, has one of the smoothest surfaces known to NBS. The process of Ti diffusion roughens the surface slightly and produces the formation of non-$LiNbO_3$ compounds within the top fraction of a micron of the waveguide surface[7]. Most likely these are compounds of lithium, titanium, and oxygen, such as Li_2TiO_3 or $Li_2Ti_3O_7$.[7] We find that the index inhomogeneity produced by these compounds or by the surface roughness associated with them are each sufficient to explain the scattering levels observed in our best experimental waveguides. These waveguides, however, were fabricated in such a way as to produce a relatively large value of the surface index change Δn and a small value of the diffusion depth D. We now know that these conditions are decidedly non-optimum from the point of view of reducing waveguide scattering, a fact that was not obvious experimentally because they turn out to be optimum conditions for minimizing the significant contribution from prism-enhanced scattering. On the basis of theory developed during the program we predict that employing waveguide-diffusion treatments to produce $\Delta n \approx 0.005$ and $D \approx 3.3$ μm, to give a specific but not all-inclusive example, will reduce the scattering contributed by surface roughness to negligible levels.

Residual scattering would then be associated with surface-compound formation. This contribution, while remaining greater than that from surface roughness, is also reduced by fabricating waveguides having small Δn and large D. This reduction occurs simply because the modal distribution of guided light produces a smaller field at the surface under conditions of small Δn and large D. However, there is some evidence that the longer, hotter diffusion treatment leading to these conditions will also increase the material homogeneity of the surface.[17] This produces a further reduction in scattering quite apart from that associated with the modal-field distribution. On this basis we conclude that waveguides suitable for the spectrum analyzer should result from simple adjustments of the diffusion conditions. However, we emphasize that the waveguides, when evaluated using prism coupling, may not appear to be of high quality because of the increase in prism-enhanced scattering when Δn is reduced and D is made larger.

Finally, we note that our expectation that low waveguide scattering results from longer, hotter diffusion treatments does not guarantee the success of a spectrum analyzer fabricated using such a treatment. Reference 32 shows that geodesic lenses formed in waveguides having a small $\Delta n/D$ ratio may have through-puts intolerably low for applications. If this happens to be true, it may be necessary to employ waveguides having Δn and D values that are non-optimum from the point of view of in-plane scattering characteristics. Scattering from these waveguides may still be reduced to tolerable levels by post-diffusion polishing of the surface. This was investigated in the first phase of this two year scattering program.[1] Figure 12 of Ref. 1, reproduced as Fig. C2 of Appendix C, shows the best scattering performance observed during either phase of the scattering-reduction program. It was obtained by post-diffusion polishing of a sample that initially showed evidence of significant surface-compound formation.

In summary, we believe that Ti diffused waveguides formed in $LiNbO_3$ using suitable diffusion conditions and post-diffusion polishing as required will suffice for the production of integrated optical spectrum analyzers having dynamic range values in excess of 40 dB, and perhaps as large as 60 dB.

APPENDIX A

NATIONAL BUREAU OF STANDARDS
EVALUATION OF SURFACE ROUGHNESS OF $LiNbO_3$

Attached is a report of test results obtained by personnel of the National Bureau of Standards. The object of the test was to obtain roughness and autocorrelation-length information for $LiNbO_3$ substrate 164. This sample was sent to NBS in as- received condition. As for other samples used in the program, the supplier was Crystal Technology. The sample dimensions were 25 mm x 25 mm x 3 mm and the polish of both broad faces was specified to be $\leq$ 1/4 in flatness. The sample was selected-acoustic grade in quality.

In summary of the attached report, the workers described the sample surface as one of the smoothest they had ever examined. The dates referred to in the report are for the year 1980.

U.S. DEPARTMENT OF COMMERCE
NATIONAL BUREAU OF STANDARDS
WASHINGTON, D.C. 20234

REPORT OF TEST

731/222492

To: Battelle Memorial Institute
Columbus Laboratories
505 King Avenue
Columbus, Ohio 43201
Attn: David Vahey

This report covers NBS measurements of the surface texture parameters of a polished $LiNbO_3$ specimen. The specimen was measured on two occasions: Jan. 25 and Apr. 7 of this year. Between these dates the data analysis program was changed so that the precision of the R_q calculation was improved on April 7. The results for the rms roughness R_q and autocorrelation length a are tabulated below.

Table I

	R_q (nm)	a (μm)
Jan. 25	$\lesssim 0.3$	36
Apr. 7	$\lesssim 0.35$	23

The above values have estimated uncertainties of approximately 30% due primarily to uncertainty in the calibrating step height, uncertainty in the measurement of horizontal displacement, digitization, and the variation in the surface properties themselves from place to place. The 30% uncertainty represents a 95% confidence interval.

Measurement Procedure

Surface topography is measured at the NBS by means of a minicomputer/stylus instrument system. Using an interferometrically measured step, the system was calibrated on each value of magnification employed during a measurement. Profiles of the calibrating step and the roughness area under test were stored in the minicomputer memory using 12 bit analog to digital conversion. Each profile contained 4000 digitized points.

The stylus tip was chisel-shaped with approximate dimensions 0.1 μm x 1 μm. The response of the system was limited to a band of surface wavelengths determined by the stylus width and various electronic filters described below. R_a values were calculated from three successive traverses of each position. The average of these was calculated and is shown in the data sheets. Then the digitized profile data from the third traverse at each position were

stored in the computer. The other parameters and the statistical functions were subsequently calculated from the stored profiles.

The experimental parameters are shown in Table II.

Table II

Date	Trace Length (μm)	Approximate Point Spacing (μm)	Positions	Bandwidth (μm)
Jan. 25	750	0.1875	1-6	4 - 200 (low pass - high pass filters)
Apr. 7	80	0.02	1-6	1 - 19 (stylus width - high pass filters)
Apr. 7	1500	0.375	7-12	4 - 200 (low pass - high pass filters)

Please note that there were two modes of operation on Apr. 7. The results quoted in Table I were taken for the long-trace mode only. The results for the short trace mode are consistent with these.

The value for R_q was calculated according to the formula

$$R_q = \left(\frac{1}{4000} \sum_{i=1}^{4000} y_i^2 \right)^{1/2} ,$$

where y_i is the height of the filtered profile with respect to the mean line at position 1.

The autocorrelation length was calculated from the average autocorrelation function for each day. It is defined as the lag distance at which the function drops to 10% of its value at zero lag. Since the noise of the instrument was appreciable at the high magnification (1 million X) required to make the measurement, the spike at zero lag was ignored and the ACF was replotted on semilog paper as several-point averages. The values for α were taken from these plots.

Additional Data

A number of other surface parameters and functions were calculated from the surface profiles and the results are included with this report. These include the parameters of average slope, average wavelength, peak-count wavelength, peak-to-mean line height, skewness, and kurtosis, and the power

spectral density function (PSD). Results were calculated for each profile and averages of these were calculated for each surface.

The PSD represents the breakdown of the profile into its component spatial frequencies f. For most surfaces the PSD monotonically decreases with increasing spatial frequency. The cutoffs shown at low frequency are due to the low-pass electronic filters. The sharp spikes are probably not real spatial components of the surface but rather components of periodic noise picked up during the measurement.

Measurements made by: Theodore Vorburger

Supervisor E. Clayton Teague

For the Director,

D. R. Flynn, Program Manager
Mechanical Production Metrology
Center for Mechanical Engineering
and Process Technology

APPENDIX B

90° SCATTERING EXPERIMENTAL ANALYSIS: DETERMINATION OF THE THRESHOLD OF VISION

In Sec. IV we described an experiment to test for scattered light at 90°. Owing to the low level of scattering encountered in $LiNbO_3$ waveguide sample 135 at that scattering angle, we found it necessary to use the human eye as the detector. Since the eye has a nonlinear response to light we limited consideration to deciding whether or not any light could be detected, rather than how much light could be detected. To convert our qualitative observation to quantitative information, it is necessary to specify the threshold of human vision.

Reference B1 indicates that for a point source of red light, the threshold of vision is about 0.15 $\mu lm/m^2$ for foveal vision and about 0.004 $\mu lm/m^2$ for extra-foveal vision. Foveal vision is described as that employed under ordinary lighting conditions, when we "look right at" an object. For the dark-adapted eye, there is a gain in sensitivity of about 40X obtained by looking at a slight angle away from the object. Assuming that this condition applied at least during part of our experiment, the threshold of vision is (0.004 $\mu lm/m^2$) x (1W/682 lm) x the aperture of the eye. Taking the latter quantity to be 5 mm^2, we find $P_{th} = 3 \times 10^{-17}$ W. Even if foveal vision is employed throughout the experiment, which seems unlikely, the threshold is still comparable to the 10^{-15} W value employed in the analysis of Sec. IV.

If the scattering source is viewed as an extended source positioned, as far as the eye can tell, at the output coupling spot, it is probably more appropriate to calculate the threshold of vision using the minimum perceptible luminance, indicated to be 5×10^{-6} cd/m^2 in Ref. B1. The power associated with this luminance is obtained as its product with the solid angle subtended by the eye in the observation and the area of the illuminating region. If the aperture of the eye is 5 mm^2 and the viewing distance is 300 mm, the solid angle subtended is 5 $mm^2/3 \times 10^4$ $mm^2 = 1.7 \times 10^{-4}$. The area of the illuminating region is the area of the output coupling spot, about 10 mm x 0.5 mm = 5 mm^2. Since 1 cd = 1 lm/steradian = (1/682) W/steradian, we find the power associated with the

threshold of vision to be

$$P_{th} = (5 \times 10^{-6}\ \text{cd/m}^2)(1.7 \times 10^{-4}\ \text{sterad})(5 \times 10^{-6}\ \text{m}^2)(1/682)(\text{W/steradian})$$

$$= 6 \times 10^{-18}\ \text{W} \qquad \text{(B1)}$$

This is slightly lower than the value calculated for a point source.

A potential problem is that our experiment could not be done in a completely darkened room, owing to the glow of the laser discharge and scattering from beam forming optics and light in the waveguide substrate. Nevertheless the value $P_{th} = 10^{-15}$ W used in Sec. IV is two orders of magnitude larger than that which we have calculated here, and this could compensate somewhat for the error introduced by utilizing visual sensitivity data presumed to apply in a totally darkened environment. We note that 1 nW of HeNe laser light incident on a white card is visible to the eye under reduced but not totally darkened lighting conditions. Assuming that 100% of this power is reflected, an upper limit of 10^{-14} W is incident on the eye at a distance of 30 cm. This is only one order of magnitude larger than the value we have employed for the threshold of vision.

Reference

B1. J.W.T. Walsh, Photometry, Constable and Company Ltd., London, 1953, Chapter III.

APPENDIX C

SCATTERING ASSOCIATED WITH PRISM COUPLING

In this appendix we present a theoretical analysis of what is referred to in the text as "prism-enhanced scattering." Our major conclusions, cited often in the text, are the following: (1) An ideal prism can effectively magnify the scattering contribution from scattering centers in the waveguide beneath the input-coupling prism, relative to the scattering contribution from the free waveguide. (2) The enhancement is greater when the angular divergence of the input beam acts to produce a low coupling efficiency, and should be reduced to tolerable levels by using a well-collimated input beam.

Figure C1 shows a diagram of the prism waveguide geometry in the vicinity of the input-coupling region. In order to be specific, we consider scattering centers associated with Li-Ti-O compound formation just beneath the waveguide surface. We will take that view of scattering in which the source of the scattered field is the polarization vector $\underline{\delta P} = \underline{P}_{actual} - \underline{P}_{ideal}$, where $\underline{P}_{actual}$ is the polarization in the presence of scattering centers and $\underline{P}_{ideal}$ is the polarization that would result if there were no scattering centers. From the definition

$$\underline{P} = (\epsilon - \epsilon_o)\underline{E} \quad , \tag{C1}$$

we determine

$$\delta\underline{P} = \delta\epsilon\underline{E} \tag{C2}$$

where $\underline{E}$ is the total field at the surface and $\delta\epsilon$ is the change in permittivity associated with the scattering mechanism. Since $\epsilon = n^2\epsilon_o$ in the optical regime, $\delta\epsilon = 2n\delta n\epsilon_o$ may be substituted in Eq. 2.

The scattered field $\underline{E}_s$ from a given scattering center will be proportional to the dipole moment, which is the integral of the polarization δP over the volume of the center. For the case of islands of Li-Ti-O compounds formed near the waveguide surface, we use a typical area a^2, measured in the

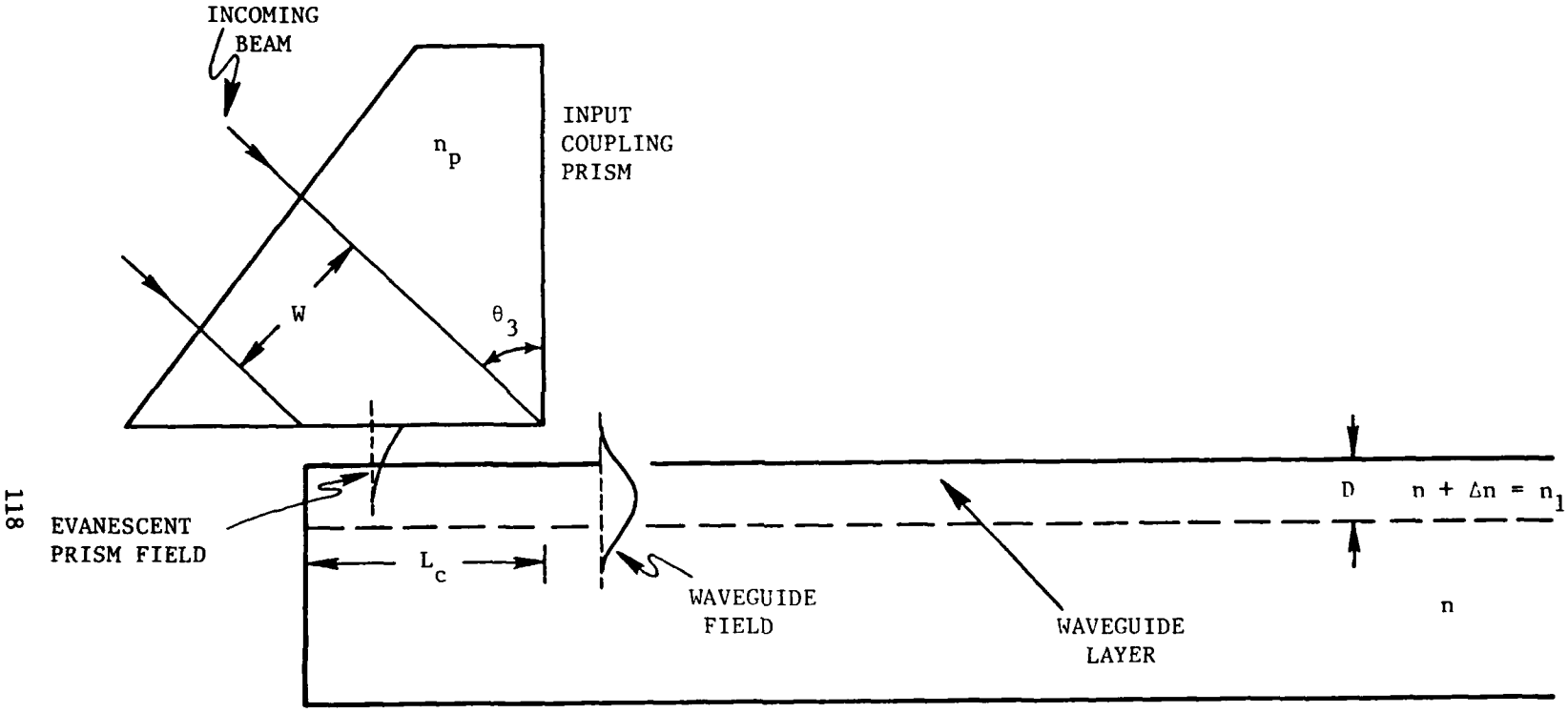

Fig. C1. Geometry for analysis of scattering associated with input prism coupling.

plane of the waveguide, and a depth z_o Thus

$$E_s \propto \delta n E a^2 z_o \quad , \tag{C3}$$

where E_s is the (scalar) field from one scattering center. The intensity from N scattering centers is proportional to NE_s^2. For this discussion we are interested only in the fact that N is proportional to the beam path length L. For the scattered intensity, we write

$$I = K\delta n^2 E^2 a^4 z_o^2 L \quad , \tag{C4}$$

where K is a constant of proportionality.

Our interest is in comparing the scattered intensity from the prism-coupling region to that from the free waveguide. We assume that all parameters in Eq. C4 except for E and L are unaffected by the presence of the prism. Thus we write

$$I_g = K' E_g^2 L_g, \qquad K' = K\delta n^2 a^4 z_o^2, \tag{C5}$$

for the scattered intensity from the free waveguide, where E_g is the waveguide field at the surface, and L_g is the path length between input and output coupling prisms. Similarly, the scattered intensity from the input-prism coupling region is

$$I_c = K' E_c^2 L_c \quad , \tag{C6}$$

where E_c is the total field at the waveguide surface and L_c is the coupling length.

The field E_c contains contributions from the modal waveguide field E_g and from the evanescent field associated with light that is totally reflected at the base of the input-coupling prism. If this field is called E_p, then the largest value of E_c at the waveguide surface is

$$E_c = E_p + E_g \quad . \tag{C7}$$

If $E_p >> E_g$, the light intensity scattered in the coupling region relative to that scattered in the free waveguide is

$$I_c/I_g = E_p^2 L_c / E_g^2 L_g \quad . \tag{C8}$$

This ratio can be unity or greater even if $L_c << L_g$, since we assume $E_p >> E_g$. To see if this inequality can hold in practice, a calculation based on the prism-coupling theory of Tien and Ulrich[C1] is in order.

Equations 11 and 12 of the latter reference provide an expression for the field E_p in terms of the amplitude of a plane wave incident on the base of the coupling prism. If A_3 is taken to be the amplitude of the plane wave, consistent with the notation of Tien and Ulrich,[C1] we have

$$E_p = A_3 \, \tau_{321} \quad , \tag{C9}$$

where τ_{321} is the amplitude transmission across the gap of the three layer system consisting of prism, air gap, and waveguide layer. Equation 12 of Ulrich[C2] contains a general expression for τ_{321}:

$$\begin{aligned} \tau_{321} &= 4h(n_p^2 - n^2)^{1/2}(n_p^2 - 1)^{-1/2} \, e^{-i\phi}(1 + h^2 e^{-2i\phi})^{-1} \\ h &= \exp[-k_o S(n^2 - 1)^{1/2}] \\ \phi &= \tan^{-1}[(n^2 - 1)^{1/2}(n_p^2 - n^2)^{-1/2}] \quad , \end{aligned} \tag{C10}$$

where n_p is the prism index, n is the $LiNbO_3$ index, S is the gap width, and $h << 1$ describes the weak-coupling limit.

To obtain the corresponding expression for the field from the waveguide mode at the surface, we use the differential equation derived by Tien and Ulrich to describe the interaction between the waveguide field

and the prism field. This is Eq. (42) of Reference C1. In terms of real variables, rather than normalized variables, and in terms of our notation, the differential equation is

$$\begin{aligned} dA_1/dx &= \alpha A_3 - \gamma A_1 \\ \alpha &= (\tau_{321}/2nD)(n_1^2-n_g^2)^{1/2} \\ \gamma &= (1/nD)(n_1^2-n_g^2)(n_p^2-n^2)^{1/2}(n_p^2-1)^{-1}f^2(h) \\ f^2(h) &= 4h^2[(1+h^2)^2-4h^2(n^2-1)(n_p^2-1)^{-1}] \quad . \end{aligned} \tag{C11}$$

In this equation $n_1 = n + \Delta n$ is the waveguide surface index, $n_g = n + \Delta nb$ is the mode index, and x is the coupling distance. The result can be expressed in terms of the notation of Tien and Ulrich by using

$$(n_1^2-n_g^2)^{1/2} = n_1\cos\theta_1 \simeq n_1/\tan\theta_1 \quad , \tag{C12}$$

valid for waveguides like $LiNbO_3$ having $\Delta n << n$. In this equation $\theta_1 \simeq \pi/2$ is the angle of incidence on the waveguide surface of the bounce modes described by Tien and Ulrich.

In Eq. (C11) we have also used $\tau_{321}(n_1^2-n_g^2)^{1/2}/(n_p^2-n^2)^{1/2}$ in place of the transmission T of Tien and Ulrich. Additionally, the coefficient γ in Eq. (C11) is the expression that results when the quantity $1-r_1$ of Reference C1 is expressed in terms of the strength parameter h and refractive index parameters. This is done using Eq. (24) of Reference C1. Finally in Eq. (C11), D is used to describe waveguide depth instead of the W used by Tien and Ulrich.

Note that in the differential Eq. (C11) A_1 is the amplitude of one of the two equivalent bounce waves into which the waveguide mode may be resolved. The peak field of the mode is $2A_1$. The field at the surface is found in terms of the peak field by solving the waveguide boundary conditions. For a strongly assymetric waveguide like $LiNbO_3$, the analysis of Marcuse[C3] indicates that

$$E_g(x) = 2A_1(x)(n_1^2-n_g^2)^{1/2}(n_g^2-1)^{-1/2} \quad . \tag{C13}$$

Taking $n_1 = n + \Delta n$ and $n_g = n + \Delta nb$, with $\Delta n << n$, this result is expressed approximately as

$$E_g(x) = 2A_1(x)[2n\Delta n(1-b)]^{1/2}(n^2-1)^{-1/2} \quad . \tag{C14}$$

It is instructive to substitute this result and the result of Eqs. (C9) and (C10) into Eq. (C11) to arrive at

$$dE_g(x)/dx = [2\Delta n(1-b)/D][(n^2-1)^{-1/2}E_p - 4h^2(n_p^2-n^2)^{1/2}(n_p^2-1)^{-1} E_g(x)] . \tag{C15}$$

This differential equation relates the waveguide field at the surface to the evanescent prism field at the surface. For the case of weak coupling, the second term in Eq.(C15) may be neglected, and the waveguide surface field is found to be

$$E_g(x) = [2\Delta n(1-b)/D](n^2-1)^{-1/2}E_p x \quad . \tag{C16}$$

If $x = \ell$ is the effective length over which input coupling occurs, we find

$$E_g(\ell) = [1.021\Delta n(1-b)\ell/D]E_p \quad , \tag{C17}$$

where we have used $n = 2.2$ to obtain the numerical coefficient 1.021. If $\Delta n = 0.005$, $b = 0.5$, $D = 3.0\mu m$, and $\ell = L_c = 1mm$, the beam width and coupling spot size we find $E_g(\ell) = 0.851\ E_p$. The waveguide surface field is then comparable to the evanescent prism field. In accord with the discussion associated with Eqs.(C6)-(C8), the scattering from the input-coupling region is enhanced by the contribution of the prism field, but it remains small in comparison to scattering from the free waveguide, owing to disparity in the path lengths.

This conclusion is based on the assumption that $\ell = 1mm$. A very different conclusion can result if we suppose that effective coupling occurs

over a smaller distance. This could occur, for example, if the incident beam has a slight divergence, so that the correct coupling angle is achieved only across part of the beam. This would be the part nearest the termination of the coupling spot, in order to avoid coupling out part of the waveguide beam.

To get an indication of what value ℓ might have, we begin by deriving a relation for coupling efficiency. The defining expression is (C1)

$$\eta = \frac{(c/4\pi)\ n\ D\ A_1(\ell)A_1^*(\ell)}{(c/8\pi)\ n_p\ W\ A_3A_3^*} \tag{C18}$$

where the modal field $A_1(\ell)$ may be determined from the field at the surface $E_g(\ell)$ or by integrating the differential Eq.(C11). For low coupling efficiencies such as are encountered in practice, we use $A_1(\ell) = \alpha A_3 \ell$, where α is given in Eq.(C11). We also note the relation between beam width W and coupling spot size L_c, $W = L_c \cos\theta_3$, where $\theta_3 = \sin^{-1}(n_g/n_p)$ is the angle of incidence on the base of the coupling prism. Substituting these results in Eq. 18, we obtain

$$\eta = |\tau_{321}|^2(n_1^2-n_g^2)(n_p^2-n^2)^{-1/2}\ell^2/2nL_cD \quad . \tag{C19}$$

From the defining Eq. 10, we find $|\tau_{321}|^2 = 4f^2(h)(n_p^2-n^2)/(n_p^2-1)$, where $f^2(h)$ is given in Eq.(C11). $f^2(h)$ varies from $4h^2$ for small values of h to approximately 2 for h=1.

We are interested in the possibility of attaining reasonable coupling efficiencies with small values of ℓ. This is best accomplished if $|\tau_{321}|^2$ has its largest value, $|\tau_{321}|^2 \simeq 8(n_p^2 - n^2)/(n_p^2-1) = 3.755$. Eq. 19 then becomes,

$$\eta = 2.037\Delta n(1-b)\ell^2/L_cD \quad , \tag{C20}$$

where we have used $n_1^2-n_g^2 \simeq 2n\Delta n(1-b)$. For $\Delta n = 0.005$, $b = 0.5$, $\ell = 200\mu m$, $L_c = 1mm$, and $D = 3.0\mu m$, we obtain $\eta = 6.8\%$ for the input coupling efficiency.

We typically observe waveguide through-put in the range 5-10%. This is marginally consistent with the above value for η if output coupling efficiency is in the range 50-100%. This high efficiency is possible because there is no restriction on output coupling length imposed by beam size or divergence, as is the case with input coupling.

Using ℓ = 200μm in Eq.(C17), we determine $E_g(\ell) = 0.170\ E_p$. That is, the peak waveguide field is approximately one-sixth the magnitude of the prism field at the waveguide surface. The prism field is not effected much by slight beam divergence, and may be regarded as constant over the coupling length L_c. The maximum possible scattered intensity from this field is then proportional to $E_p^2 L_c$, which is to be compared to scattering from the free waveguide, proportional to $E_g^2 L_g$. The ratio of prism-coupling scattering to waveguide scattering is

$$R = I_c/I_g = E_p^2 L_c / E_g^2 L_g \quad . \tag{C21}$$

A numerical value R = 2.3 is found for the example $E_g = 0.170\ E_p$, L_c = 1.0 mm, and L_g = 15.0 mm.

A more accurate analysis would employ an effective coupling length $L_c' < L_c$ in Eq.(C21) to account for the fact that some of the light scattered into waveguide modes by the prism field is out-coupled before it reaches the free waveguide. The quantity $e^{-2\gamma(L_c-x)}$ is the probability that a photon scattered at x will reach $x = L_c$ without being lost to the waveguide, where γ is the amplitude attenuation coefficient given in Eq.(C11). The power scattered by the prism field E_p which reaches the free waveguide is

$$E_p^2 L_c' = E_p^2 \int_o^{L_c} dx e^{-2\gamma(L_c-x)} \tag{C22}$$

from which we obtain

$$L_c' = (1/2\gamma)(1-e^{-2\gamma L_c}) \quad . \tag{C23}$$

For the numerical parameters used in the calculation so far, we find $L_c' = 481\mu m$. The light scattered from the prism coupling region then reduced to 111% of the total light scattered from the free waveguide.

While it must be acknowledged that the derived result R = 1.11 was obtained through the choice of favorable parameters, the calculation does add support to the experimental observation that prism-associated scattering is a significant part of the total in plane scattering measured. It is instructive to consider that the total effective scattering path length is given by

$$L = L_g + L_e \tag{C24}$$

where $L_e = RL_g$ is the effective additional scattering path length associated with prism enhancement. From Eqs.(C17),(C21),(C23), and (C11) we obtain

$$L_e = 0.96\ [D/\ell\Delta n(1-b)]^2(1/2\gamma)(1-e^{-2\gamma L_c}),$$
$$\gamma = 0.51[\Delta n(1-b)/D]f^2(h) \quad . \tag{C25}$$

In obtaining this result, we have used L_c' from Eq.(C22) in place of L_c in Eq.(C21).

If we perform scattering measurements with the coupling prisms separated first by L_g and then by L_g', the ratio of scattered intensity in the two measurements is given by

$$I_s/I_s' = (L_g + L_e)/(L_g' + L_e) \tag{C26}$$

where it is assumed that the effective length of the coupling region, L_e, is the same in the two experiments. We have used $L_g' = L_g/10$ in experiments. This leads to

$$I_s/I_s' = (1 + L_e/L_g)/(0.1 + L_e/L_g) \quad . \tag{C27}$$

If $L_e = L_g$ the ratio is approximately 2. In other words, a factor of 10 change in free waveguide path length is accompanied by only a factor of 2 change in scattering. This is characteristic of our observations. We have even obtained results in which $I_s' \gtrsim I_s$, as can occur if L_e increases when the path length is reduced owing to variations in coupling efficiency.

The main assumption required to obtain values of L_e/L_g as large as unity is that of a small effective coupling length ℓ. Supporting evidence for a small value of ℓ is the fact that coupling to a waveguide mode occurs over a range of tuning angles that happens to be about 1 mrad in our experiments. This range includes the natural tuning range for the mode and a contribution from external factors such as beam divergence. We will use $\Delta\theta_{nat}$ to describe the natural angular turning range and $\Delta\theta_{div}$ to describe the tuning range associated with beam divergence. If $\Delta\theta_{div}$ is large compared to $\Delta\theta_{nat}$, we expect efficient coupling to occur over a distance

$$\ell = L_c \, \Delta\theta_{nat}/\Delta\theta_{div} \quad . \tag{C28}$$

A value for $\Delta\theta_{nat}$ may be calculated from formulas presented in the paper by Ulrich.[C2] If $n_p \sin\theta_3 = n_g$ defines the angle of incidence θ_3 for coupling to the mode having the effective index n_g, a slight variation in θ_3, say $\delta\theta$, causes a change in n_g by an amount

$$\delta n_g = n_p \cos\theta_3 \, \delta\theta = (n_p^2 - n^2)^{1/2} \, \delta\theta \quad . \tag{C29}$$

Ulrich shows that the energy density of light in the waveguide region falls off in Lorentzian fashion with increasing δn_g, or equivalently, with increasing $\delta\theta$. The full-width-at-half-maximum energy density is

$$\Delta n_g = (n_p^2 - n^2)^{1/2} \, \Delta\theta_{nat} = 2K_m \tag{C30}$$

in Ulrich's notation, where K_m is given by Eq. (37) of his paper.[C2] Transferring our notation to his result we have, in the limit $h \ll 1$,

$$\Delta\theta_{nat} = 16h^2[2n\,\Delta n(1-b)]^{1/2}/\chi(n_p^2-1)$$

$$\chi = -(\partial\psi/\partial b)/\Delta n$$

$$\psi = 2k_o D[2n\Delta n(1-b)]^{1/2} - 2\phi_{10} - 2\phi_{12} \qquad \text{(C31)}$$

$$\phi_{10} = \tan^{-1}[b/(1-b)]^{1/2}$$

$$\phi_{12} = \tan^{-1}[(n^2-1)/(2n\Delta n)(1-b)]^{1/2} \quad .$$

In evaluating $\partial\psi/\partial b$, we may neglect the contribution $\partial\phi_{12}/\partial b$ since $\phi_{12} = \pi/2$ for all values of b that are of interest. We find

$$\partial\psi/\partial b = -[b(1-b)]^{1/2}[k_o D(2n\Delta nb)^{1/2}+1] \quad . \qquad \text{(C32)}$$

By inserting this result into Eq. (C27), we obtain

$$\Delta\theta_{nat} = [16h^2/(n_p^2 - 1)][\Delta n(1-b)/k_o D][Q/(Q+1)]$$

$$Q = k_o D(2n\Delta nb)^{1/2} \quad . \qquad \text{(C33)}$$

For the parameter values used in this section, including $h \simeq 1$, $\Delta n = 0.005$, $b = 0.5$, $D = 3.0\mu m$ and $k_o = 2\pi/0.633\mu m$, $\Delta\theta_{nat}$ is in the vicinity of 0.1 mrad. This is about one-tenth the total tuning range that we observe for our waveguides, suggesting

$$\Delta\theta_{nat}/\Delta\theta_{div} = 0.1 \quad . \qquad \text{(C34)}$$

In this case, only one-tenth of the extent of the incident wavefront is capable of coupling efficiently to the waveguide, or $\ell = L_c/10$. This is comparable to the values found in our earlier calculations to give large prism enhancement of scattering.

One possible alternative to the concept of prism-enhanced waveguide scattering holds that the scattering results from inperfections in the coupling prisms. We have several observations that suggest that this is not the case. First, the angular distribution of inplane scattering does not change much when the prism separation is reduced. This suggests that the size of the scattering centers is the same in the waveguide region as in the prism region. Barring coincidence, this suggests that the scatterers are localized in the waveguide. Second, we have observed in our best waveguide a very low level of scattering, even though no special precautions were taken with the prism couplers. This waveguide was discussed in detail in Ref. 1., and its scattering performance is reproduced in Figure C2. We interpret the result as indicating that the reduction of waveguide scattering centers, as was done by polsihing in this case, is accompanied by the reduction of prism-enhanced scattering as well. This is consistent with our model, but not consistent with the idea that the prisms have fixed scattering centers associated with them.

Finally, we observe that prism-coupling scattering is greater in the case of input coupling than output coupling. This would not be the case for scattering centers fixed to the prism, but it is the case for prism enhanced waveguide scattering. The mechanism that our model employs for prism-enhanced scattering requires the evanescent field of the input beam to act as the source of scattering. This source is not available in output coupling. Hence, less enhancement is predicted in the case of output coupling.

We observed that this prediction was satisfied by an experiment in which end-fire coupling was used along with a single-prism coupler. Total scattering was less when the prism was used for output coupling and input coupling was accomplished by end fire.

We conclude that the model of prism-enhanced waveguide scattering exhibits many of the features that we have encountered in experiments. Let us consider, then, how this effect may be reduced in future observations. The main contribution leading to a large prism enhancement is the existance of a small effective length ℓ = 100μm over which input coupling can occur. If ℓ be increased ten fold to the value associated with the coupling spot size or beam width, prism enhancement of the scattering is calculated to be negligible.

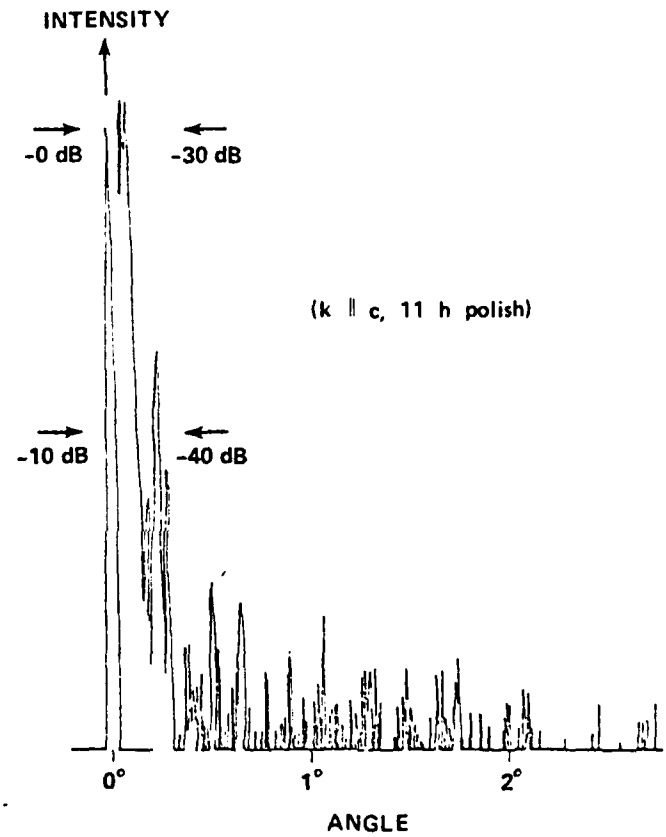

Fig. C2. In-plane scattered-energy distribution for the TE_0 mode propagating parallel to the optic axis, after 11 h total polishing time.

We determined above that ℓ = 100μm was compatible with a beam divergence of about 1 mrad. This is the natural divergence angle of many low power He-Ne lasers, consistent with the typical beam width W = 1mm. Increasing ℓ should simply be a matter of carefully controlling beam collination and insuring that the Gaussian waist coincide with the input coupling region.

References

C1. P. K. Tien and R. Ulrich, "Theory of Prism-Film Coupler and Thin Film Light Guides", J. Opt. Soc. Am., 60 (10), 1325-1337 (1970).

C2. R. Ulrich, "Theory of Prism-Film Coupler by Plane-Wave Analysis", J. Opt. Soc. Am., 60 (10), 1337-1350 (1970).

APPENDIX D

DETERMINATION OF WAVEGUIDE PARAMETERS FROM DIFFUSION CONDITIONS

It may be noted that the determination of scattering cross sections using the various formulas of the text inevitably requires knowledge of the waveguide index parameters Δn and D. These are generally determined using the relations

$$\Delta n = AT/D$$

$$D = 2[\mathcal{D}(T)t_D]^{1/2} \tag{D1}$$

where A is an empirically determined coefficient, T is the Ti-film thickness, T is the diffusion temperature, $\mathcal{D}(T)$ is the diffusion coefficient at that temperature, and t_D is the diffusion time.

The purpose of this appendix is to point out the caution that must be taken in employing this type of analysis. The largest source of error is in the film thickness T. This thickness is intended to correspond to that of an oxygen-free Ti film prior to diffusion. However, Ti is an effective getter of oxygen and our e-beam-evaporated films invariably show more transparency than they would be expected to for a pure Ti film, owing to the presence of residual oxygen in the vacuum system. Measured values of T are therefore too large by a factor that depends on the oxygen content of the film. Our own experience is that this content depends strongly on the vacuum system employed. Therefore, in applying the empirical relationship $\Delta n = AT/D$, the waveguide in question should be fabricated from the same vacuum system used in experiments to determine the constant A.

In our recent work, $LiNbO_3$ waveguides have been diffused from e-beam evaporated films formed in two different vacuum systems. In each case, the e-beam gun was the same. The sample of Figure 20, emphasized in this report because of its examination using end-fire coupling, was formed using the more efficient vacuum system. It was diffused from a Ti film of thickness 250 Å as determined by a crystal thickness monitor and 315 Å as determined using an angstrometer.

Optical transmission was estimated to be in the range 10-25%. Most of the other waveguides of the program were diffused using slightly more transmissive films, say 33% transmissive. These films were evaporated in a less efficient vacuum system. For a given thickness these films would have had less Ti and therefore would produce waveguides with a smaller Δn. We also note that the waveguides having a greater oxygen content entered the substrate more rapidly. This would indicate a larger diffusion depth D. Since most scattering mechanism decrease in strength with smaller Δn and larger D, it appears appropriate to diffuse films that have been evaporated in relatively imperfect vacua. It also appears reasonable to carry out the diffusion in a oxygen-rich atmosphere, as we do, rather than in argon.

It is ironic that the waveguide of Figure 20, which shows the best scattering performance of any waveguide fabricated during the current program, was fabricated under non-optimum conditions leading to a large Δn and small D. We believe that the good performance resulted from the elimination of prism-enhanced scattering and that much better performance may be expected from waveguides fabricated under the more optimum conditions outlined in Sec. V.

APPENDIX E

MEASUREMENT OF SURFACE ROUGHNESS FROM SCATTERING OF REFLECTED LIGHT

This appendix describes a series of measurements that we made in order to determine the surface-roughness parameters of our diffused $LiNbO_3$ waveguides. These measurements were made with the idea of correlating surface roughness with measured in-plane scattering levels, using the theoretical results of Sec. IV. The measurements proved to be exceedingly complicated and of limited precision, so this plan was not fully implemented. However, those measurements that were made are worth discussing.

EXPERIMENTAL CONFIGURATION

The experimental configuration that was employed is shown in Fig. E1. A gently focused laser beam was incident on the sample at approximately 45°. It is critical that the beam be highly filtered spatially so that the only scattered light observed in the far field is that associated with the sample surface. This filtering is most readily accomplished if the beam is focused on or near the sample. However, the size of the beam incident on the sample should be large in comparison to the roughness autocorrelation length in order to justify a statistical analysis of the results.

Note from Fig. E1 that scattered light is monitored in the actual far field. A lens is not used to generate the far-field condition because of the scattering which would be introduced by surface roughness and imperfections in the lens. Another problem is that of second-surface reflections from the sample. These were either eliminated by blocking with a razor edge, or they were allowed to contribute to the scattered signal. Blocking is difficult because light diffracted from the razor is often comparable to or larger than the scattered signal. On the other hand, allowing the second surface to contribute to the scattering introduces an unknown quantity into the measurement because the second surface will not contain a diffused waveguide, generally, and may also have a greater incidence of scratches and imperfections introduced during sample handling.

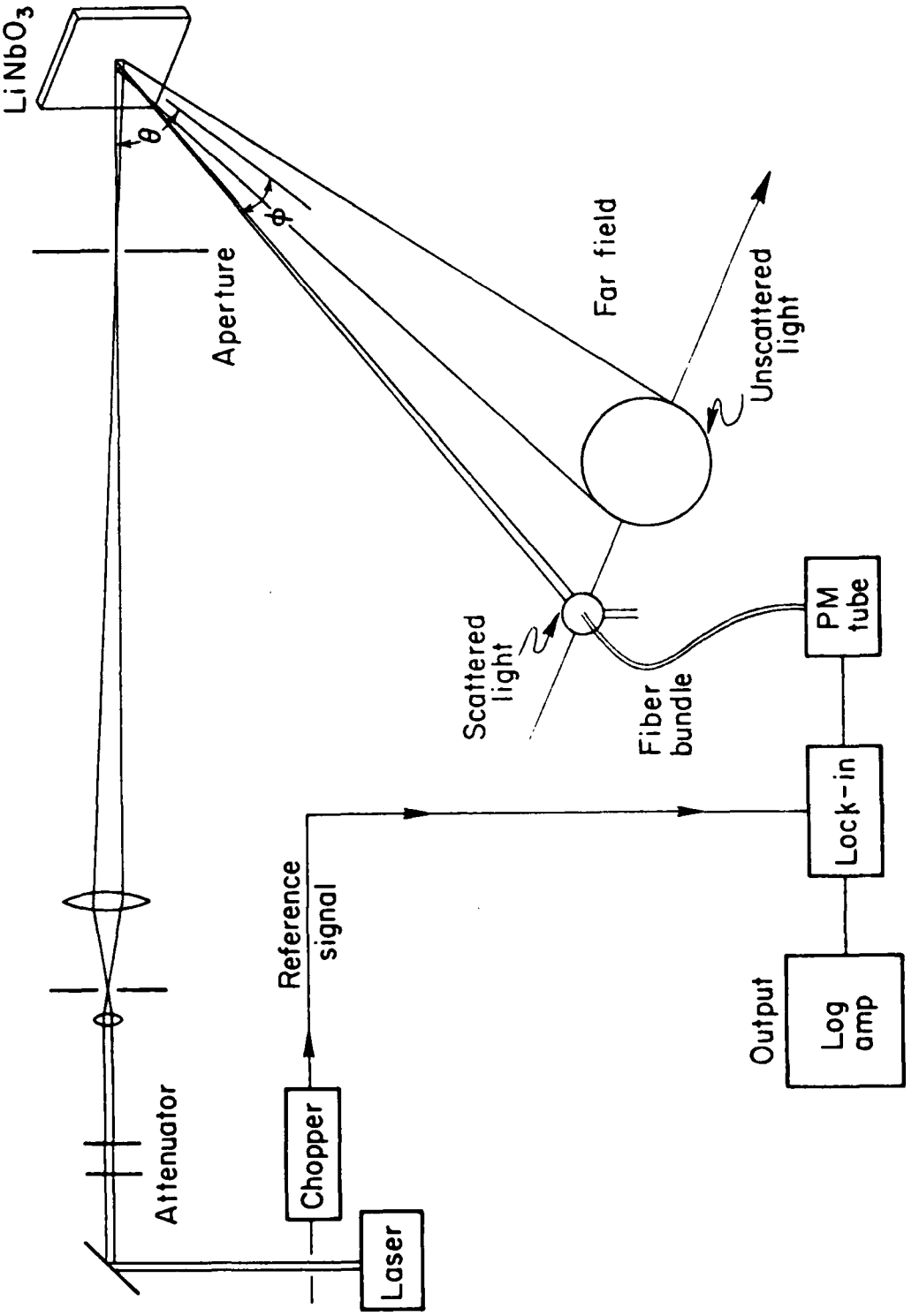

Fig. E1. Reflection experiment for measurement of surface roughness.

Add to this the fact that the surfaces of $LiNbO_3$ are intrinsically very smooth (see Appendix A) and one can begin to appreciate the difficulty of the measurement. We will be describing the measurement of scattering levels in the range -60 to -70 dB.

THEORETICAL ANALYSIS

Our analysis of surface scattering parallels that of Sec. IV for Rayleight-Gans-Debye scattering from waveguide index inhomogeneities. We consider in Fig. E2 a single roughness element in an otherwise smooth surface. The roughness height is σ and the lateral size (autocorrelation length) is a. Light reflected from the surface has its wavefront locally perturbed as a result of the phase perturbation. The strength of the perturbation is $\Delta\phi = k_o\sigma\cos\theta$, and it occupies a region of size $a\cos\theta$, in the near field.

In the far field, the amplitude distribution is that of the unperturbed beam plus the contribution from the roughness element, as described by the laws of diffraction. For $\sigma << \lambda_o$ the perturbed wavefront in the near zone has the peak amplitude

$$A_{no} = iA_o k_o \sigma\cos\theta \tag{E1}$$

If the roughness element is circular in the plane of the surface with radius a, the wavefront perturbation will be elliptical, with major axis a perpendicular to the plane of incidence and minor axis $a\cos\theta$ in the plane of incidence.

For convenience we will assume a Gaussian profile

$$A(x,y) = A_{no}e^{-(4/a^2)(x^2/\cos^2\theta + y^2)} \tag{E2}$$

where x and y are coordinates attached to the reflected beam: the z axis is the direction of propagation, the x axis is in the plane of incidence, and the y axis is normal to the plane of incidence.

In the Fraunhofer zone, the amplitude distribution is the Fourier-transform of Eq. (E2), or

$$A_f(X,Y) = -(ik_o/2\pi z)e^{ik_o z}\iint dxdyA_n(x,y)e^{i(k_o/z)(xX + yY)} \tag{E3}$$

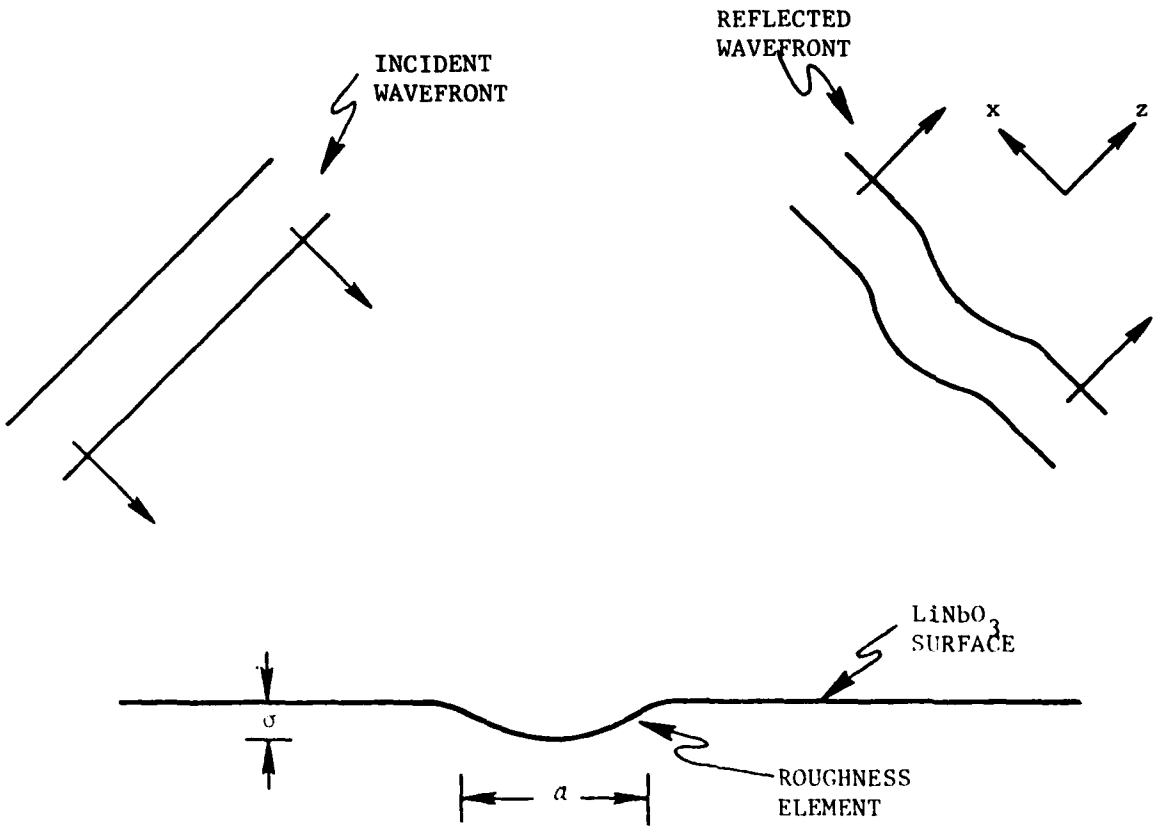

Fig. E2. Geometry for analysis of scattering caused by reflection from a rough surface.

where X,Y are the coordinates in the observation plane that correspond to x,y in the near zone, and z is the distance of the observation plane from the plane of the sample. The result of carrying out the integration is

$$A_f(X,Y) = -A_o\, e^{ik_o z}(k_o^2\sigma a^2\cos^2\theta/8z)\exp[-X^2k_o^2a^2\cos^2\theta/16z^2$$

$$-Y^2k_o^2a^2/16z^2] \qquad \text{(E4)}$$

The power from this scattered field intercepted by a detector of area S at a distance z from the sample is

$$\delta P = (c/8\pi)|A_f|^2 S \quad . \qquad \text{(E5)}$$

As for an in-plane scattering measurement, this power is referenced to the peak power in the unscattered beam. This power is determined by a Fourier-transform similar to Eq. (E3) for the incident field

$$A(r) = A_o\, e^{-4r^2/W^2} \qquad \text{(E6)}$$

where W is the width of the incident beam on the surface, measured between opposite $1/e^2$ intensity points. By inserting Eq. (E6) in place of $A_n(x,y)$ in Eq. (E3) we obtain

$$A_u(R) = iA_o(k_o/2\pi z)e^{ikR}\,\pi(W^2/4)e^{-(R^2/z^2)k_o^2W^2/16} \qquad \text{(E7)}$$

as the unscattered amplitude in the far zone. Note that r and R are the radial coordinates corresponding to x,y and X,Y, respectively.

The peak power collected by the detector of area S is

$$P = (c/8\pi)|A_u(0)|^2 S. \qquad \text{(E8)}$$

The relative scattered power is obtained by dividing Eq. (E8) into Eq. (E5) and substituting the results of Eqs. (E7) and (E4). The result is

$$(\delta P/P) = (k_o^2\sigma^2 a^4 \cos^4\theta/W^4)\ \exp(-\phi_x^2\ k_o^2 a^2\cos^2\theta/16 \qquad \text{(E9)}$$

$$-\phi_y^2 k_o^2 a^2/16) \quad ,$$

where $\phi_x = X/z$ and $\phi_y = Y/z$ are introduced to indicate the angle of scattering.

Thus far we have considered only scattering from a single roughness element positioned at the most intense position of the beam. Other elements see less incident power and their scattering strength is reduced proportionately. Let x',y' be cartesian coordinates of the plane of the surface, with the origin at beam center and the x' axis in the plane of incidence. Owing to the oblique approach of the beam, the intensity at x',y' is

$$I(x',y') = I(0)\ \exp[-8x^2\cos^2\theta/W - 8y'^2/W] \quad . \qquad \text{(E10)}$$

Within an increment of area dx'dy' the total number of roughness elements is $dx'dy'/a^2$, and their contribution to scattered power is δP times the exponential term in Eq. (10). The total scattered power is

$$\Delta P = \delta P a^{-2} \iint_{-\infty}^{\infty} dx'dy'\ e^{-8x'^2\cos^2\theta/W^2\ -8y'^2/W^2} \qquad \text{(E11)}$$

$$= \delta P(\pi W^2/8a^2\cos\theta) \quad .$$

The total relative scattered power is obtained from Eq. (E9) by multiplying by $(\Delta P/\delta P)$. The result is

$$\Delta P/P = (\pi/8)(k_o^2\sigma^2 a^2\cos^3\theta/W^2)\ \exp(-\phi_x^2 k_o^2 a^2\cos^2\theta/16 \qquad \text{(E12)}$$

$$-\phi_y^2 k_o^2 a^2/16) \quad .$$

Experimentally, we scan along the X axis, that is, in the plane of incidence. Thus $\phi_y = 0$ in Eq. E12, and we replace ϕ_x by ϕ for simplicity. The equation to use in analyzing the data is

$$\Delta P(\phi)/P = (\pi/8)(k_o^2\sigma^2 a^2\cos^3\theta/W^2)\ e^{-\phi^2 k_o^2 a^2\cos^2\theta/16} \quad . \qquad \text{(E13)}$$

Note that W is the waist of the incident beam, since we assumed in the analysis that the incident wavefronts were planar in the vicinity of the sample. However, the experiment may be performed with a diverging or converging beam. The scattered power will remain constant since the number of scattering centers goes up to compensate for the lower intensity at the sample surface. One must take care to use the beam waist for W in Eq. E14 rather than the beam diameter at the sample.

RESULTS AND ANALYSIS

Figure E3 shows the first experimental results, obtained for sample 154. In plotting the normalized scattered intensity versus scattering-angle squared we expect to find a linear variation except near the orgin where the unscattered intensity is large. These data are not plotted in Fig. E3, so a good straight line is obtained down to the noise level of the system. The slope and intercept of this line provide information regarding the autocorrelation length a and the surface roughness σ. The relevant formulas obtained using Eq. E13 are

$$\text{slope} = (10 \log e)(k_o a \cos\theta/4)^2 \tag{E15}$$

$$\text{intercept} = 10 \log [(\pi/8)(k_o^2 a^2 \sigma^2 \cos^3\theta/W^2)]$$

The first expression is used to find a value for a. This value is then inserted into the second expression to enable the determination of a value for σ. Even if the data shows a good straight-line behavior, as does Fig. E3, we caution the reader not to place significance on the values so obtained beyond a factor of about 2. Our derivation has not followed a mathematically rigorous path (E2). and even if it had we would ultimately have to make assumptions regarding the surface roughness statistics valid for our sample. Thus we take some liberty when we refer to a as the autocorrelation length and σ as the rms surface roughness. Nevertheless the data of Fig. E3 indicates that a = 52 μm and σ = 29 Å. To obtain these values, we used $k_o = (2\pi/0.633)\mu m^{-1}$, $\theta = 47°$, and W = 142 μm.

It was this experiment that led us to believe that surface roughness was an important source of the observed scattering level in sample 154, as shown

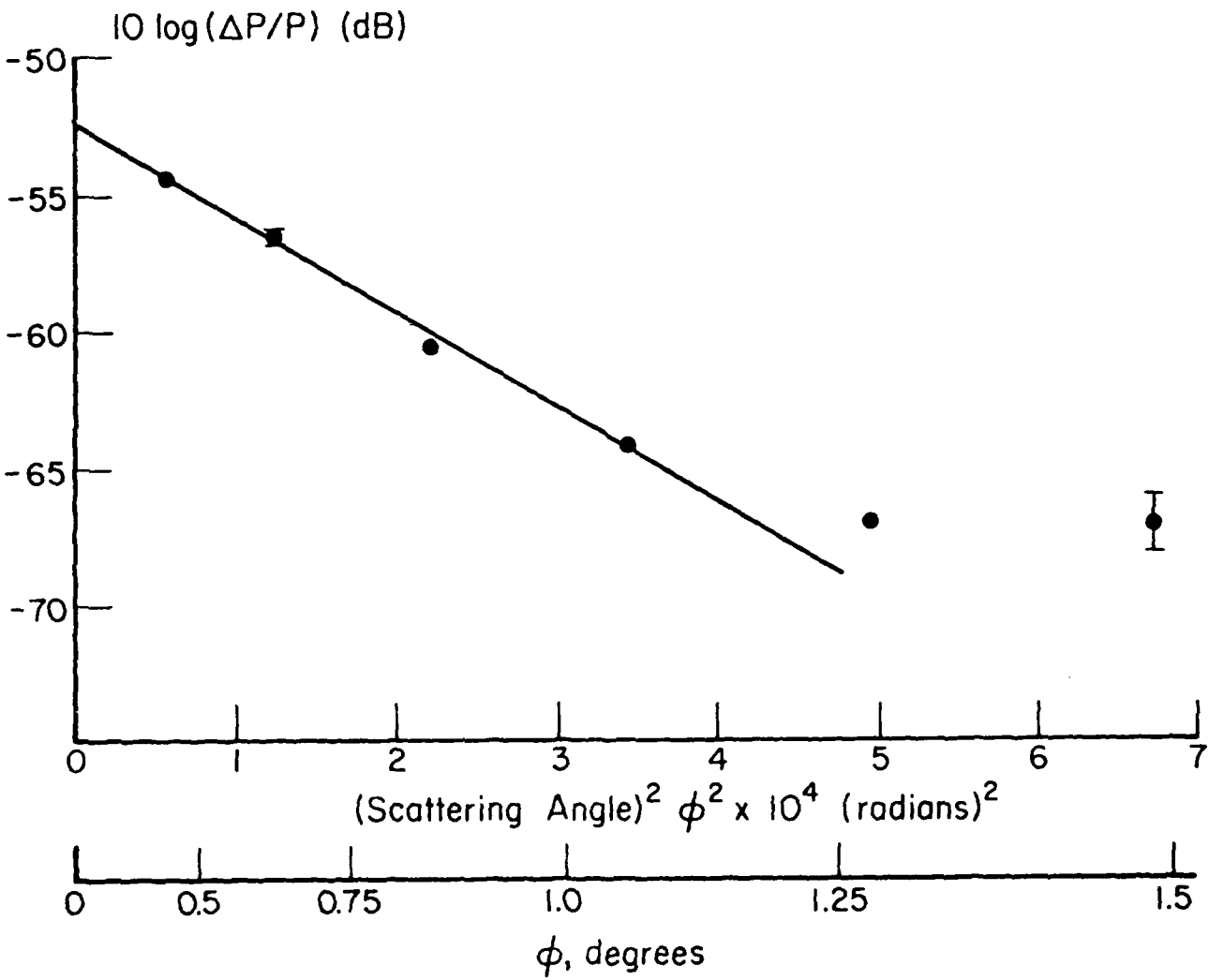

Fig. E3. *Normalized* scattered intensity vs scattering angle.

in Fig. 20. Although we later found that surface-compound formation could also explain our in-plane scattering results, we embarked on a program to measure surface roughness for various waveguide samples and to correlate the results with in-plane scattering levels for the same waveguides. This led to refinements in the Experiment of Fig. E1 and made us aware of the experimental difficulties of the measurement which we had not appreciated when the data of Fig. E3 were taken.

First of all, we had assumed that all scattering observed was that from roughness in the $LiNbO_3$ surface. In fact, it is impossible to filter out all background scattering from optics used in the measurement, so an initial determination of this background scattering must be undertaken. This was done by removing the sample from the optical path and measuring the scattered energy in the incident beam. Then a similar measurement was made with the crystal in place.

These measurements were made for $LiNbO_3$ substrate 165. The NBS Talysurf examination of the similar substrate 164 had shown the surface to have a smoothness less than or comparable to 3 Å. One does not therefore expect to see much additional scatter produced by the $LiNbO_3$ surface. The experimental results of Fig. E4 show this to be true. Data taken with and without the crystal in place are identical to within experimental uncertainty. The error bars in Fig. E4 pertain to the data taken without the crystal in place, shown as solid data. Several runs were made and the variations in scattered intensity at a given angle were used to determine the error bars. The position of the dots are determined by averaging the results for two runs.

Best-fitting straight lines for the data are also plotted in Fig. E4. The dashed line pertains to scattering observed with the sample in place. The solid line refers to scattering from the incident beam. The proximity of the two lines in comparison to the size of the error bars shows that the $LiNbO_3$ roughness cannot be measured by this technique. In fact, if $\sigma \approx 3$ Å as determined by NBS for a similar sample, we expect the intercept for surface roughness scattering to fall between -70 and -75 dB, almost three orders of magnitude below the measured background scattering level.

Figure E5 shows the results of a comparable experiment performed after a Ti-diffused waveguide was fabricated in sample 165. The fabrication conditions were similar to those for sample 169; that is, a 600 Å Ti film was diffused for 8 h at 1000°C. The surface roughness produced by the diffusion was sufficient to

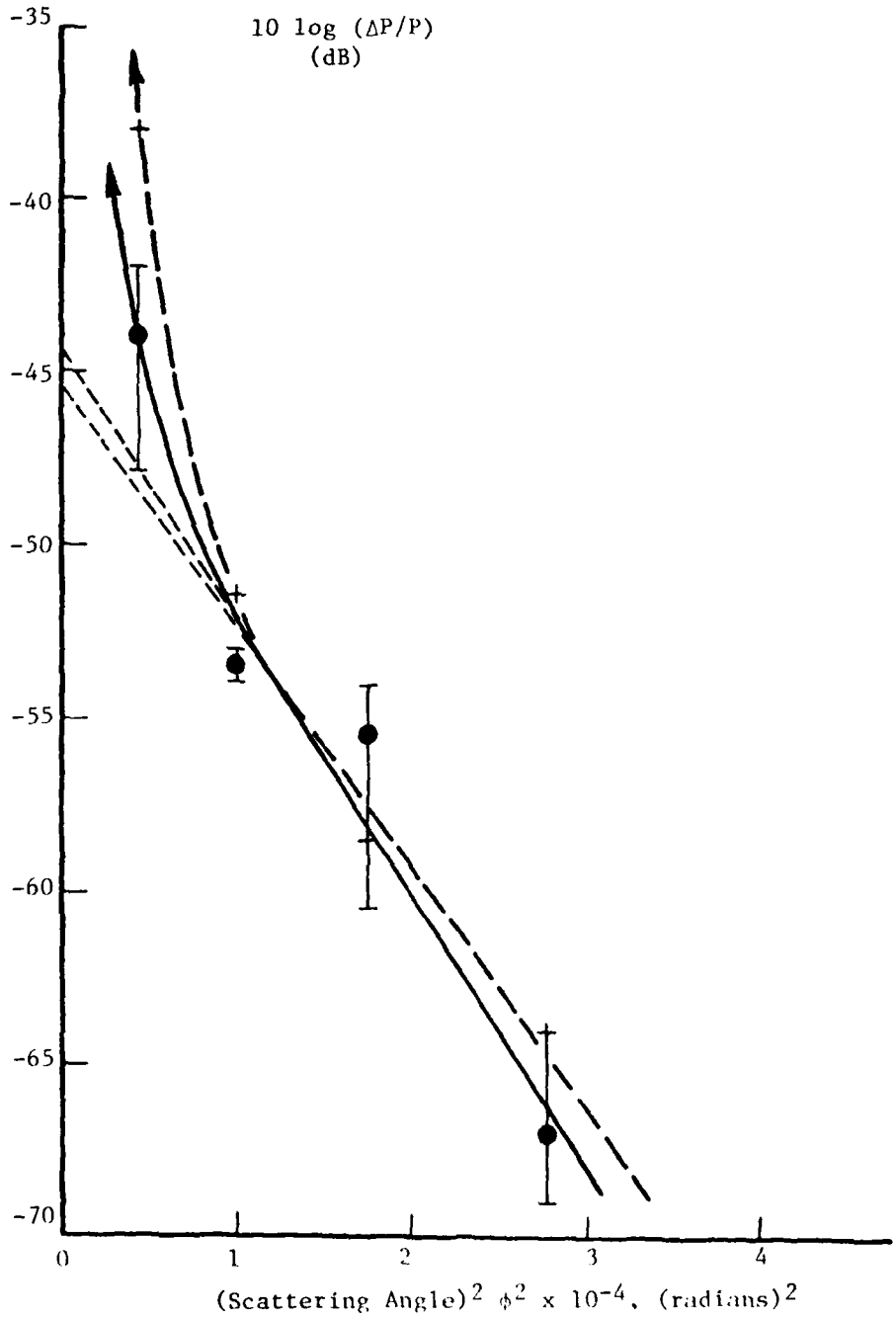

Fig. E4. Normalized scattered intensity vs scattering-angle squared prior to waveguide formation. Dots correspond to background scattering from optics, crosses correspond to scattering from optics plus the $LiNbO_3$ surface prior to waveguide formation. Straight lines show best linear fit, excluding data above -50 dB.

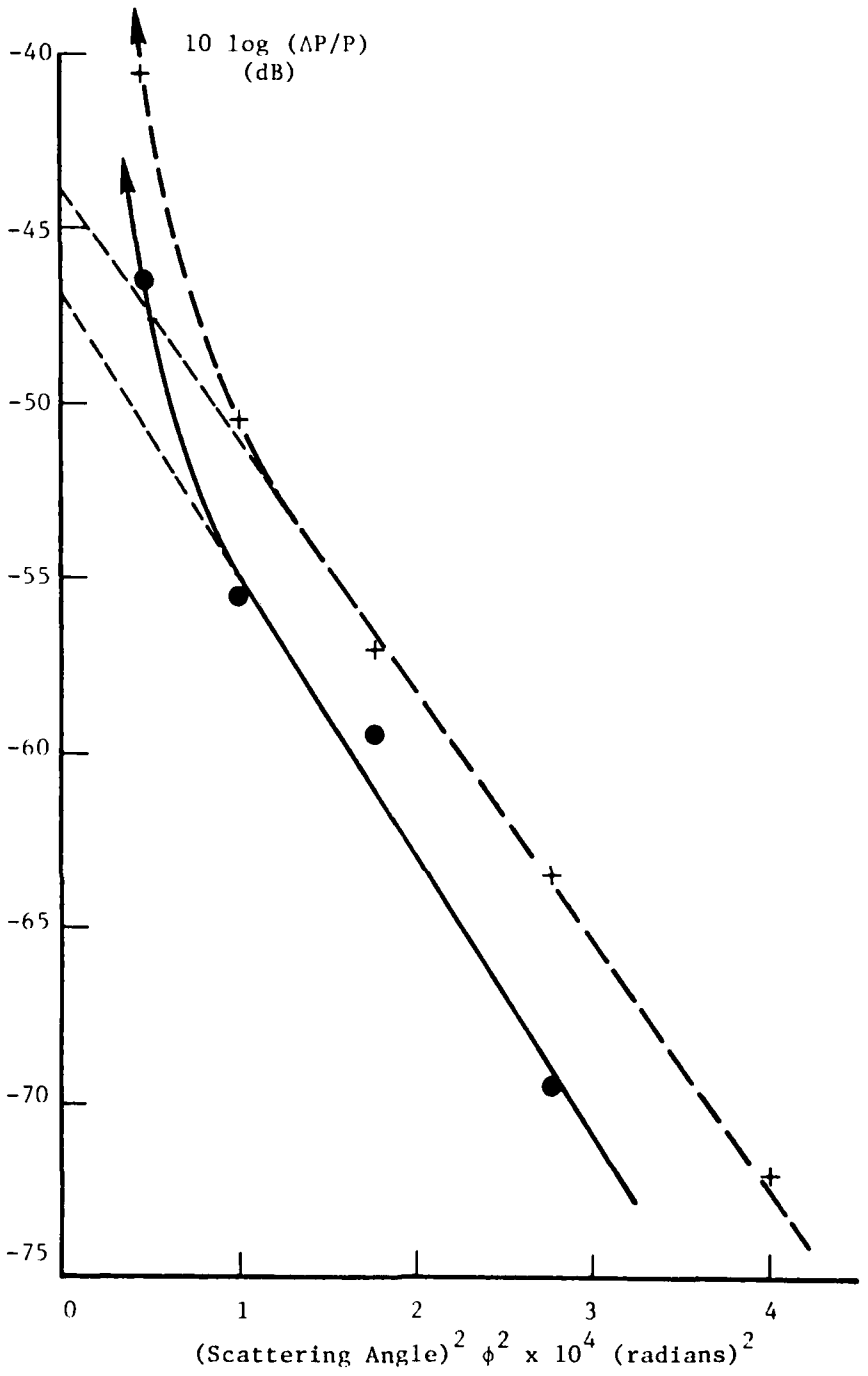

Fig. E5. Scattering level vs scattering-angle squared following waveguide formation. Dots correspond to background scattering from optics. Crosses correspond to scattering from optics plus the $LiNbO_3$ surface following waveguide formation. Straight lines show best linear fit, excluding data above -50 dB.

cause a measurable scattered signal above the background level. The scattering associated with the waveguide alone was determined by subtracting the value of $\Delta P/P$ associated with the background from the value associated with the background plus waveguide. When this was done as a function of scattering angle, using the straight lines in Fig. E5 to determine $\Delta P/P$ values, a curve was constructed which is virtually a straight line having intercept -45.67 dB and slope 6.45×10^4 dB/radian^2. This straight line is plotted in Fig. E6 along with the straight line obtained from Fig. E3 for sample 154. Despite significant differences in slope and intercept, the two lines are found to be consistent with fairly similar values for a and σ. We find

$$a(154) = 52\ \mu m$$
$$a(165) = 72\ \mu m$$
$$\sigma(154) = 29\ \text{Å}$$
$$\sigma(165) = 29\ \text{Å}$$

This is surprising in view of the very different fabrication conditions for the two waveguides. However it is consistent with our observation that waveguide 169, fabricated similarly to 165, had in-plane scattering characteristics comparable to 154. It may be that diffusion induced roughness is smoothed away for sufficiently long diffusion times.

References

E1. D. C. Champeney, Fourier Transforms and Their Physical Applications, Academic Press, London, 1973, p. 22.

E2. P. Beckmann and A. Spizzichino, The Scattering of Electromagnetic Waves from Rough Surfaces, Pergamon Press, Oxford, 1968.

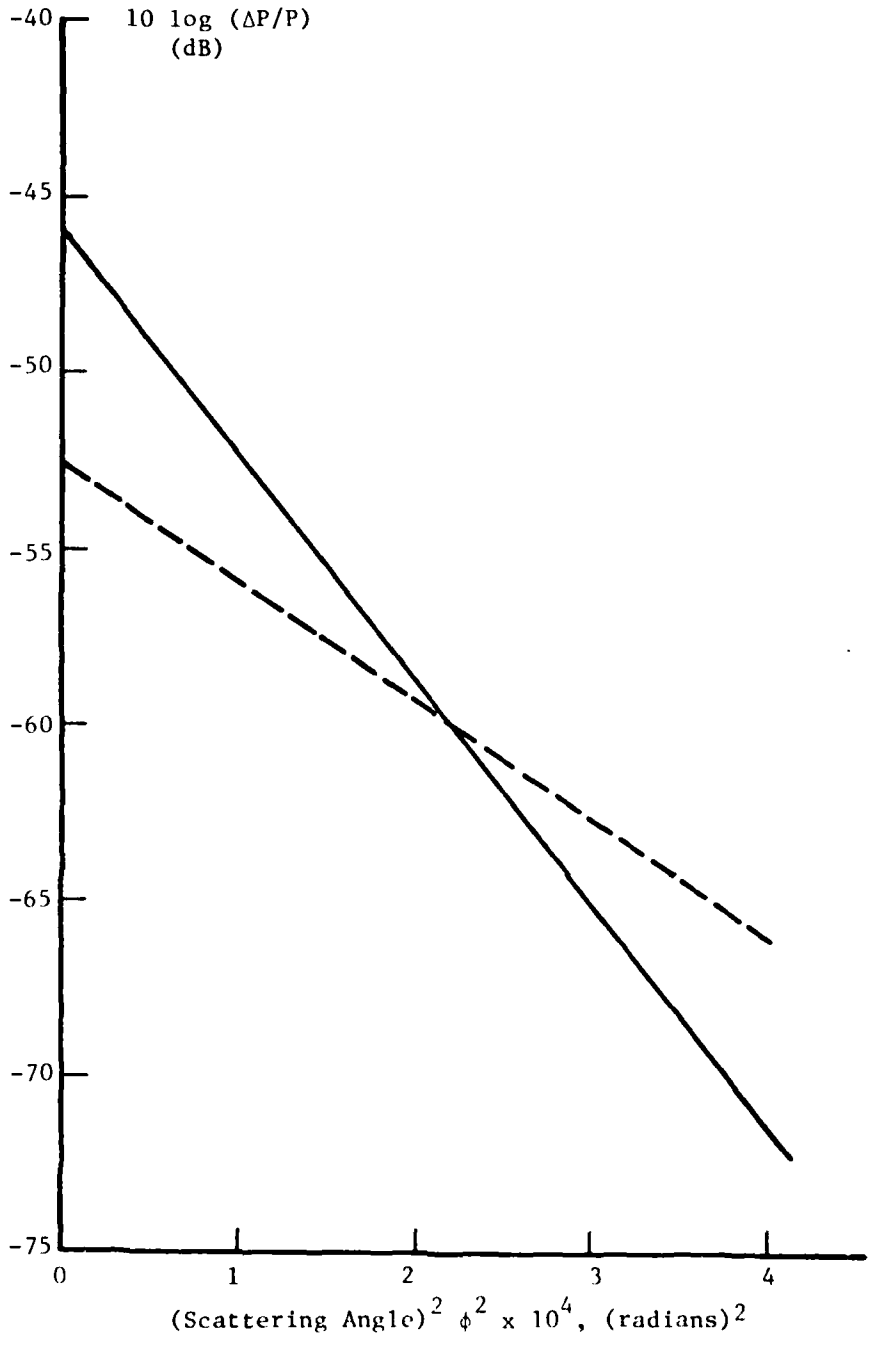

Fig. E6. Normalized scattered intensity versus scattering-angle squared for sample 154 (dashed line) and sample 165 (solid line).

REFERENCES

1. D. W. Vahey, "Optical Waveguide Scattering Reduction", Air Force Technical Report AFAL-TR-79-1113, Final report for the period 15 April 1978 to 15 April 1979, prepared by Battelle Columbus Laboratories.

2. M. C. Hamilton, D. A. Wille, and W. J. Miceli, "An Integrated Optical RF Spectrum Analyzer", Optical Engineering, 16 (5), 475-478 (1977).

3. D. Marcuse, Light Transmission Optics, Van Nostrand Reinhold, New York, 1972, Chapters 8 and 9.

4. J. T. Boyd, and D. B. Anderson, "Effect of Waveguide Optical Scattering on the Integrated Optical Spectrum Analyzer Dynamic Range", IEEE J. Quantum Electron, Vol. QE-14 (6), 437-443 (1978).

5. D. J. Walter and J. Houghton, "Attenuation in Thin Film Optical Waveguides Due to Roughness Induced Mode Coupling", Thin Solid Films, 52, 461-476 (1978).

6. K. Nassau, H. J. Levinstein, and G. M. Loiacono, "Ferroelectric Lithium Niobate. 1. Growth, Domain Structures, Dislocations, and Etching", J. Phys. Chem. Solids, 27, 983-988 (1966).

7. W. K. Burns, P. H. Klein, E. J. West, and L. E. Plew, "Ti Diffusion in Ti:$LiNbO_3$ Planar and Channel Optical Waveguides", J. Appl. Phys., 50 (10), 6175-6182 (1979).

8. K. Nassau, H. J. Levinstein, and G. M. Loiacono, "Ferroelectric Lithium Niobate. 2. Preparation of Single Domain Crystals", J. Phys. Chem. Solids, 27, 989-996 (1966).

9. N. Ohnishi, "An Etching Study on a Heat-Induced Layer at the Positive Domain Surface of $LiNbO_3$", Japan J. Appl. Phys., 16 (6), 1069-1070 (1977).

10. J. D. Venables, "Damage-Induced Microdomains in $LiTaO_3$", Appl. Phys. Lett., 25 (5), 254-256 (1974).

11. V. Ramaswamy and R. D. Standley, "Growth Strains and Losses in Nb-Diffused $LiTaO_3$ Optical Film Waveguides", Appl. Phys. Lett., 26 (1), 10=12 (1975).

12. G. D. Boyd, R. V. Schmidt, and F. G. Storz, "Characteristics of Metal-Diffused $LiNbO_3$ for Acoustic Devices", J. Appl. Phys., 48 (7), 2880-2881 (1977).

13. K. Sugii, M. Fukuma, and H. Iwasaki, "A Study of Titanium Diffusion into $LiNbO_3$ Waveguides by Electron-Probe Analysis and X-Ray Diffraction Methods", J. Mats. Sci., 13, 523-533 (1978).

14. L. O. Svaasand, M. Eriksrud, G. Nakken, and A. P. Grande, "Solid Solution Range of $LiNbO_3$", J. Crystal Growth, 22, 230-232 (1974).

15. C. M. Horwitz, R. C. McPhedran, and J. A. Beuner, "Interference and Diffraction in Globular Metal Films", J. Opt. Soc. Sm., 68 (8), 1023-1038 (1978).

16. W. Lang, "Nomarski Differential-Interference-Contrast Microscopy". ZEISS Information, Carl Zeiss, Inc., New York.

17. R. J. Esdaile, A. D. McLachlan, and R. M. DeLaRue, "New Aspects of Titanium Diffusion in Lithium Niobate", Talk WB3-1, Technical Digest, Conference on Integrated and Guided Wave Optics, Incline Village Nevada, January, 1980.

18. H. E. Bennett, "Characterization of Optical Thin Films and Surfaces", J. Opt. Soc. Am., 69 (10), 1426 (1979).

19. S. Tolansky, Multiple Beam Interferometry, Clarendon Press, Oxford, 1948.

20. M. Minakata, S. Saito, and M. Shibata, "Two-Dimensional Distribution of Refractive Index Changes in Ti-Diffused $LiNbO_3$ Strip Waveguides", J. Appl. Phys., 50 (5), 3063-3067 (1979).

21. M. Fukuma, J. Noda, and H. Iwasaki, "Optical Properties of Titanium-Diffused $LiNbO_3$ Strip Waveguides", J. Appl. Phys., 49 (7), 3693-3698 (1979).

22. D. J. Channin, J. M. Hammer, and M. T. Duffy, "Scattering in ZnO-Sapphire Optical Waveguides", Appl. Opt., 14 (4), 923-930 (1975).

23. J. W. Goodman, Introduction to Fourier Optics, McGraw-Hill, San Francisco, 1968, Chapter 4.

24. G. B. Hocker and W. K. Burns, "Modes in Diffused Optical Waveguides of Arbitrary Index Profile", IEEE J. Quantum Electron., Vol. QE-11, No. 6, 270-276 (1975).

25. D. Marcuse, Theory of Dielectric Optical Waveguides, Academic Press, New York, 1974, Chapter 1.

26. K. H. Haegele and R. Ulrich, "Pyroelectric Loss Measurements in $LiNbO_3$:Ti Guides", Opt. Lett., 4 (2), 60-62 (1979).

27. F. A. Jenkins and H. E. White, Fundamentals of Optics, Third Ed., McGraw-Hill, New York, 1957, p. 51.

28. E. Malarkey, private communication.

29. A. M. Glass, "The Photorefractive Effect", Opt. Eng., 17 (5), 470-479 (1978).

30. R. V. Schmidt and I. P. Kaminow, "Metal-Diffused Optical Waveguides in $LiNbO_3$", Appl. Phys. Lett., 25 (18), 458-460 (1974).

31. V. E. Wood, N. F. Hartman, and C. M. Verber, "Characteristics of Effused Slab Waveguides in $LiNbO_3$", J. Appl. Phys., 45 (3), 1449-1451 (1974).

32. D. W. Vahey, R. P. Kenan, and W. K. Burns, "Effects of Anisotropic and Curvature Losses on the Operation of Geodesic Lenses in Ti:$LiNbO_3$ Waveguides", Appl. Opt., 19 (2), 270-275 (1980).

*U.S.Government Printing Office: 1981 – 757-002/509

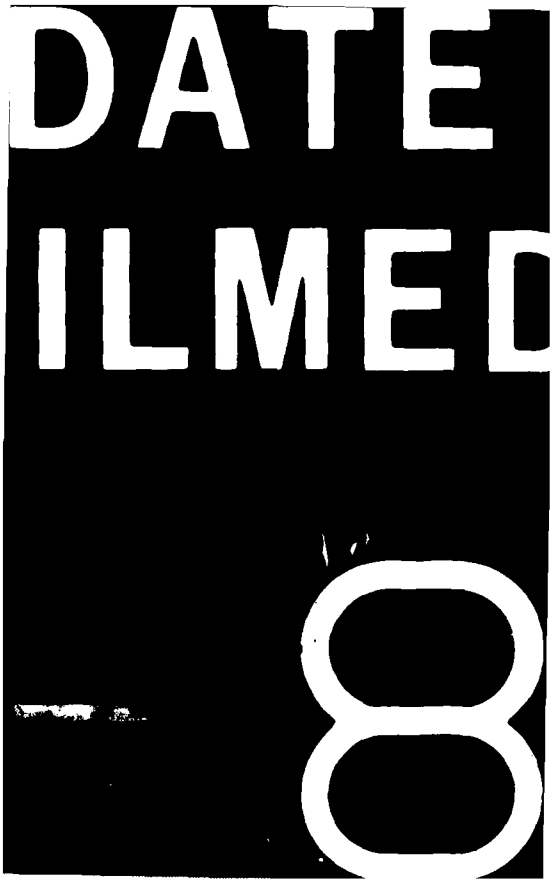
DATE
ILMED
8